Renewable energy storage in geological porous media

—

Coupled process simulation for storage dimensioning in renewable energy grids and estimation of induced hydraulic impact

Dissertation
in fulfilment of the requirements for the degree "Dr. rer. nat." of the Faculty
of Mathematics and Natural Sciences at Kiel University

submitted by
Firdovsi Gasanzade

Kiel, June 2023

First referee: Prof. Dr. Sebastian Bauer
Second referee: Prof. Dr.-Ing. Olaf Kolditz

Date of the oral examination: 15.09.2023
Approval for printing: 15.09.2023

gez. Prof. Dr. Frank Kempken, Dekan

I hereby declare that, apart from the guidance provided by the supervisor, the content and design of the thesis are entirely my own work. Furthermore, the thesis has not been submitted, either in whole or in part, for a doctoral degree to any other examining body, and it has neither been published nor submitted for publication. The thesis has been prepared in accordance with the Rules of Good Scientific Practice of the German Research Foundation. No academic degree based on this thesis has been withdrawn.

Firdovsi Gasanzade

14.06.2023

Abstract

Energy transition from conventional to renewable energy sources requires significant large energy storage capacities to dampen the fluctuating availability of renewable sources and to ensure stability in energy supply. Energy storage in the geological subsurface has emerged as a promising solution due to its capacity and support for required cycle time. This thesis assesses three types of subsurface storage - hydrogen, methane and compressed air – with an emphasis on quantifying their storage potential at a site-specific level, integrating suitable geological storage into renewable energy systems and quantifying secondary induced gas leakage during storage operations.

The study area is located within the North German Basin, where potential storage sites are screened employing a newly constructed three-dimensional structural model. Site-specific estimates of stored energy and exergy capacities are obtained through a volume-based approach, indicating that capacity for a single site may reach the tens of TWh range. Additionally, high well deliverability rates are found predominantly in two out of three considered storage formations. Despite geological parameter uncertainty, the storage potential for all three technologies is significantly larger than the predicted demand and viable storage rates are achievable in all storage formations.

To evaluate the integration of subsurface storage into renewable energy systems, a compressed air energy storage (PM-CAES) type is simulated using coupled models. The use of coupled power plant and subsurface models allowed for the consistent determination of load profiles and storage plant performance characteristics in energy systems. Numerical simulations are performed using open-source thermal engineering code and the multiphase-multicomponent reservoir simulator. The PM-CAES systems can supply 115 MW of electric power and between 12.1 GWh and 49.9 GWh of electric energy for up to 429 h, thereby offering grid-scale power storage capacity. The storage design is robust against variations in future energy system scenarios and different power plant configurations, with efficiencies between 0.54 and 0.67 and energy densities between 0.12 kWh and 0.28 kWh per kilogram of stored air. The storage design can be improved by using horizontal instead of vertical wells, which also reduces induced pressure effects in the storage reservoir.

A novel semi-analytical solution for the coupled power plant - geostorage model is developed to approximate geological storage processes, facilitating efficient assessment of their role in energy systems. The model accurately simulates storage operations, considering fluid properties, well configurations and facility constraints. Validation with realistic energy system scenarios shows that the model provides a consistent approximation, capturing storage pressure, rates and capacity within 98% of the full-scale model. The designed PM-CAES plant achieves continuous energy discharge of 3 GWh - 6.69 GWh at a power rate of 50 MW, with storage efficiency of 0.53. The new model offers a reliable and efficient alternative to full-scale numerical models, reducing runtime by a factor of about 20. This approach enables fast site assessment and scenario simulations, making it valuable for optimising the design and evaluation of operational conditions for renewable energy storage applications.

The potential for stored gas leakage from adjacent or intersecting fault systems is a crucial consideration for energy storage applications. In the final section of this thesis, an evaluation of the gas leakage effects during methane storage operations is conducted. Numerical scenario simulations indicate that gas leakage rates are strongly dependent on the fault's geometry, petrophysical parameters and capillary pressures affecting gas leakage rates during storage operation. Storage operation itself plays a significant role in gas leakage rates, with significant leakage occurring primarily during injection periods, with peak rates potentially reaching thousands of cubic meters per day. Increasing capillary entry pressure results in a sealing effect. During withdrawal periods, the pressure gradient between a storage formation and a fault zone is reduced or even reversed, resulting in significantly reduced leakage rates or even temporary stoppage of the leakage.

Zusammenfassung

Die Energiewende von konventionellen zu erneuerbaren Energiequellen erfordert erhebliche große Energiespeicherkapazitäten, um die schwankende Verfügbarkeit erneuerbarer Energiequellen zu reduzieren und die Energieversorgung zu sichern. Die Energiespeicherung im geologischen Untergrund hat sich als vielversprechende Lösung erwiesen, da sie eine hohe Kapazität aufweist und die erforderliche Zykluszeit unterstützt. In dieser Arbeit werden drei Arten von unterirdischen Speichern - Wasserstoff, Methan und Druckluft - untersucht, wobei der Schwerpunkt auf der Quantifizierung ihres Speicherpotenzials auf standortspezifischer Ebene, der Integration geeigneter geologischer Speicher in erneuerbare Energiesysteme und der Quantifizierung sekundär induzierter Gasleckagen während des Speicherbetriebs liegt.

Das Studiengebiet befindet sich im Norddeutschen Becken, wo potenzielle Speicherstandorte mit Hilfe eines neu erstellten dreidimensionalen Strukturmodells untersucht werden. Anhand eines volumenbasierten Vorgehens werden standortspezifische Schätzungen der gespeicherten Energie- und Exergiekapazitäten vorgenommen, die darauf hindeuten, dass die Kapazität eines einzelnen Standorts den Bereich von zweistelligen TWh erreichen kann. Darüber hinaus werden in zwei von drei betrachteten Speicherformationen hohe Bohrlochraten gefunden. Trotz der Unsicherheiten bei den geologischen Parametern ist das Speicherpotenzial für alle drei Technologien deutlich größer als der prognostizierte Bedarf und in allen Speicherformationen sind realisierbare Speicherraten möglich.

Um die Integration von unterirdischen Speichern in erneuerbare Energiesysteme zu bewerten, wird ein Druckluftspeicher (PM-CAES) mit gekoppelten Modellen simuliert. Die Kopplung von Kraftwerks- und Untergrundmodellen ermöglichte die einheitliche Bestimmung von Lastprofilen und Speichereigenschaften in den Energiesystemen. Die numerischen Simulationen werden mit einem Open-Source-Code für die Thermodynamik und dem mehrphasigen Mehrkomponenten-Simulator für Speicher durchgeführt. Die PM-CAES-Systeme können 115 MW an elektrischer Leistung und zwischen 12,1 GWh und 49,9 GWh an elektrischer Energie für bis zu 429 Stunden liefern und bieten damit Stromspeicherkapazität im Netzmaßstab. Das Speicherdesign ist robust gegenüber Schwankungen in zukünftigen

Energiesystemszenarien und verschiedenen Kraftwerkskonfigurationen, mit Wirkungsgraden zwischen 0,54 und 0,67 und Energiedichten zwischen 0,12 kWh und 0,28 kWh pro Kilogramm gespeicherter Luft. Das Speicherdesign kann durch die Verwendung von horizontalen anstelle von vertikalen Bohrungen verbessert werden, was auch die induzierten Druckauswirkungen im Speicher reduziert.

Es wurde ein neues semi-analytisches Modell für die Kopplung von Kraftwerk und Geospeicher entwickelt, um geologische Speicherprozesse zu approximieren und damit eine effiziente Bewertung ihrer Rolle in Energiesystemen zu ermöglichen. Das Modell simuliert den Speicherbetrieb unter Berücksichtigung von Flüssigkeitseigenschaften, Bohrlochkonfigurationen und Anlagenbeschränkungen genau. Die Validierung mit realistischen Energiesystem-Szenarien zeigt, dass das Modell eine konsistente Annäherung liefert und Speicherdruck, -raten und -kapazität innerhalb von 98% des numerischen Modells erfasst. Die entworfene PM-CAES Anlage erreicht eine kontinuierliche Energieentladung von 3 GWh - 6,69 GWh bei einer Leistung von 50 MW und einer Speichereffizienz von 0,53. Das neue Modell bietet eine zuverlässige und effiziente Alternative zu detaillierten numerischen Modellen und verkürzt die Rechenzeit um einen Faktor von etwa 20. Dieser Ansatz ermöglicht eine schnelle Standortbewertung und Szenariosimulationen, was ihn für die Optimierung des Designs und die Evaluierung der Betriebsbedingungen für Anwendungen zur Speicherung erneuerbarer Energien wertvoll macht.

Das mögliche Leckagepotential von Speichergas aus benachbarten oder sich kreuzenden Störungssystemen ist ein entscheidender Faktor für die Energiespeicherung. Im letzten Teil dieser Arbeit wird eine Bewertung der Auswirkungen von Gasleckagen während des Betriebs von Methanspeichern durchgeführt. Numerische Simulationen von Szenarien zeigen, dass die Gasleckageraten stark von der Geometrie der Störung, den petrophysikalischen Parametern und den Kapillardrücken abhängen, die die Gasleckageraten während des Speicherbetriebs beeinflussen. Der Speicherbetrieb selbst spielt eine wichtige Rolle bei den Gasleckageraten, wobei signifikante Leckagen vor allem während der Injektionszeiträume auftreten, wobei die Spitzenraten potenziell Tausende von Kubikmetern pro Tag erreichen können. Ein zunehmender kapillarer Eintrittsdruck führt zu einer abdichtenden Wirkung. Während der Entnahmeperioden wird das Druckgefälle zwischen einer Speicherformati-

on und einer Störungszone verringert oder sogar umgekehrt, was zu deutlich geringeren Leckageraten oder sogar zu einer vorübergehenden Schließung der Leckage führt.

Acknowledgements

During my doctoral journey, I have been fortunate to have the company of genuinely friendly and supportive individuals, I would like to express my sincere gratitude to all those who have helped me and supported me during my research.

I would like to begin by expressing my gratitude to my supervisor, Sebastian Bauer, for providing me with a conducive research environment and the opportunity to work on the topic of energy storage as part of the energy transition. His continuous guidance and valuable insights have significantly contributed to my study. I am particularly grateful for his mentoring style of evaluating specific aspects of my research in the broader picture, which has helped me in my scientific career and future endeavours.

My thanks also go to Wolf Tilmann Pfeiffer who has shared his experience and knowledge on regional geology during my first steps into PhD journey. I also extend my appreciation to Francesco Witte for his invaluable scientific input into my research on power plant engineering and model developments. Furthermore, I would also like to express my gratitude to all my colleagues at Kiel University, especially Linwei Hu, Jens-Olaf Delfs, Bo Wang for the productive conversations and invaluable assistance they provided during my breaks from studying virtual models.

Finally, I thank my parents and sister for their unwavering support during my academic pursuits, despite residing in another country. I am genuinely grateful for my wife Narmin, whose care and understanding have been instrumental in helping me achieve this milestone.

Firdovsi Gasanzade

Kiel, 2023

Contents

List of Figures

List of Tables

1 Introduction

The energy transition is a global phenomenon that aims to shift the energy sector from traditional fossil fuel sources towards cleaner, more sustainable options. This transition is driven by various factors, including concerns over climate change, energy security and the economic benefits of renewables [Clarke et al., 2022]. Fossil fuels have been of great significance in the world's economies over past decades, but today their use raises drastic concerns, primarily due to the releasing greenhouse gases that contribute to climate change. The nature of fossil fuels has a direct impact on their supply, thus being a subject to market fluctuations and geopolitical tensions. Renewable energy sources, such as wind, solar, hydro, geothermal or biomass provide a promising alternative to traditional fossil fuels and have gained significant attention in recent years. However, the integration of renewables into the energy sector is associated with certain uncertainties and challenges with regards to supply and demand over space and time [Adamek et al., 2012, Pape et al., 2014]. As such, wind and solar energy are weather dependent and can fluctuate significantly, making it challenging to ensure a stable and reliable energy supply. Therefore, addressing these challenges requires significant investments in research and development, as well as infrastructure to accelerate the deployment of renewable energy technologies.

Germany's energy system is undergoing a significant transformation towards renewables, with a focus on reducing greenhouse gas emissions and achieving climate goals. Germany has set ambitious targets for energy transition (german: Energiewende), aims to significantly increase the share of renewable energy in its energy sectors, with a target of generating 80% of electricity and 50% of heating from renewables by 2030, improve energy efficiency and phasing out nuclear power. In 2022, the net electricity generation in Germany from renewables was 244 TWh (terawatt-hours), which accounted for around 46% of the country's total net electricity generation (Fig. 1.1). The main renewable contributors are wind and solar power, while nuclear power accounts for less than 10% of Germany's electricity generation. At end of 2022, Germany had an installed renewable energy capacity of around 147 GW, which includes wind, solar, hydropower and biomass. Solar and wind energy have contributed the most with capacity of approximately 65.5 GW and 66.4 GW, followed by biomass and hydropower – around 9 GW and 5 GW, respectively. Implementation of solar and wind power by 2030 has a significant impact on the residual load, often resulting in temporary scenarios characterised by both power shortages and an excess of renewable generation capacity, thus can trigger storage demand [Weitemeyer et al., 2015]. The subsequent section outlines the factors that contribute to this demand.

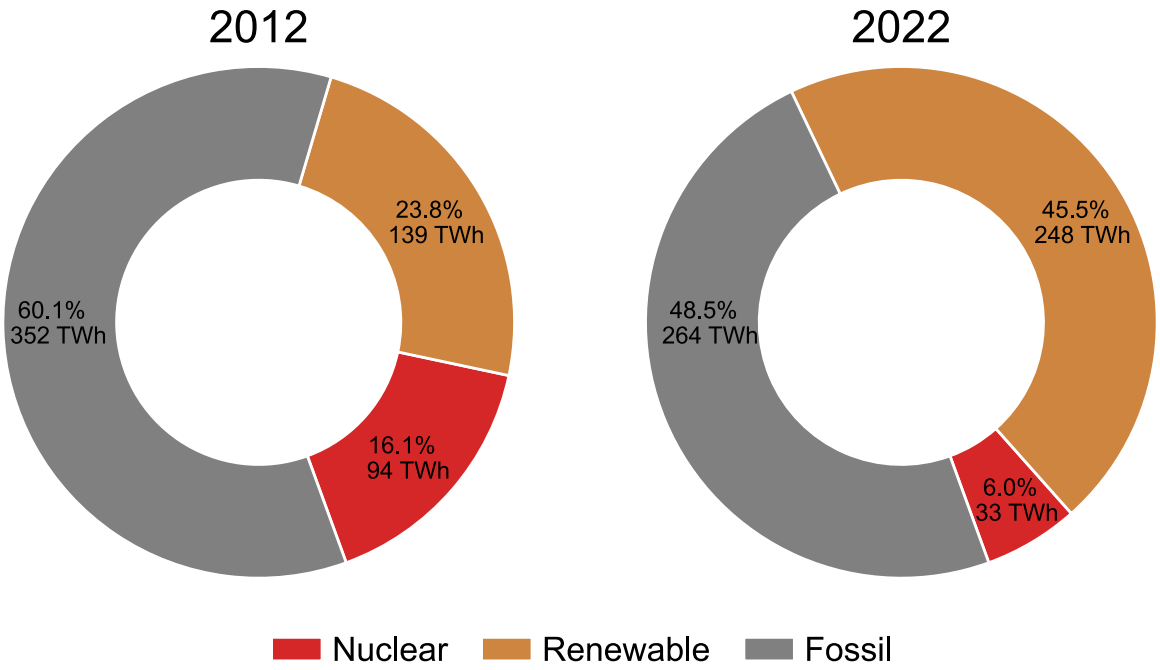

Figure 1.1: Total net electricity generation in Germany in 2012 and 2022, data ascertained by Fraunhofer ISE.

1.1 Analysis of storage demand

The renewable dominated power system can ensure flexibility and reliability through various measures such as storage, grid interconnection, excess of installed capacity, demand-side management, renewable curtailment and system diversity [Blanco and Faaij, 2018]. These measures address different aspects of the renewable energy system, such as spatial and temporal components, dynamic parameters of power plants and the need for reserve capacity to cope with fluctuations in generation and demand. Doubling shares of renewable energy sources has an influence on residual load, which is managed by balancing power [Denholm and Hand, 2011]. Storage option enables both upward and downward flexibility, storing energy when there is available surplus power or lower demand and discharging storage to meet demand at all times despite fluctuations in the generation from variable renewable sources. Upon discharge period storage can be applied in different roles with various flexibility measurements and Power-to-X technologies [Blanco and Faaij, 2018, Denholm et al., 2010].

With high shares of variable renewables, the demand for storage increases linearly in terms of power capacity and exponentially in terms of energy capacity. According to literature both storage duration and required capacity demand are widely investigated. However, the clarity in this field is lacking due to the grounding in modelling and, more specifically, in mathematical optimisation, which is the main method used for the majority of the model-based scenarios of energy system development pathways [Cebulla et al., 2018]. Multiple

studies have applied optimisation in the context of future energy systems to identify and assess strategies for reducing emissions.

SRU [2011] developed a 100% renewable power scenario for Germany, where large-scale power exchange with neither Scandinavia nor Northern Africa is possible, temporary surplus power generation may rise to 209 GW and total yearly surplus energy may exceed 53 TWh. Adamek et al. [2012] conducted an analysis on the cost-minimisation of renewable reduction and the demand for additional storage capacity across different renewable energy shares: 40%, 80% and 100%. The study showed that the respective scenarios experienced negative residual load durations of 44 h, 2329 h and 4271 h. Peak surplus power is 10 GW (40%), 50 GW (80%) and 81 GW (100%), respectively. In the 40% scenario, minimal additional storage was deemed necessary. However, in the 80% renewables scenario, 14 GW/70 GWh of short-term storage and 18 GW/7.5 TWh of seasonal storage were determined to be required. In a study conducted by Hartmann [2013], the role of storage technologies in the German renewable energy system was examined. The findings highlighted that achieving an 80% renewable share would require the installation of 66 GW of power capacity and 5.4 TWh of storage capacity.

According to Krzikalla et al. [2013], Germany is expected to have a surplus generation of approximately 35 TWh by 2030. These projections assume a thermal must-run of 5 GW in 2030, as well as flexible biomass generation. The study suggests that if there is sufficient flexibility on both the demand and supply sides, additional storage capacity will only be necessary after 2030. Schaber et al. [2013] estimated a demand of 18 TWh at 66% renewables, while Palzer and Henning [2014] reported a demand of 17.5 TWh at 100% RES. In 2050, Lunz et al. [2016] predicted that Germany would require long-term storage units with a discharge power of 23 GW, a charge power of 97 GW and a capacity of 13 TWh to meet its residual load. Schill [2014] states when there is a high share of renewables and the system is already flexible, the importance of electricity storage increases. The flexible 2050 scenario suggests that a minimum of 10 GW of storage investments would be necessary. Schiebahn et al. [2015] found that achieving seasonal balancing requires 27 TWh of storage and a 60-day reserve requires 90 TWh. The study assumed a power generation structure in Germany with high reliance on onshore and offshore wind, with 169 GW and 70 GW installed capacities respectively. According to Weitemeyer et al. [2015], depending on storage size and efficiency, the projected storage demand on the pathway towards 100% renewable energy could range from 0.2 TWh to 9.1 TWh, with a total demand of up to 80 TWh for some assumptions.

Although the available literature data lies within a wider range span, it is clear that the

requirements for storage increase, as moving towards a 100% renewable energy system. The high capacities of intermittent power generation are expected to be matched by high storage demand. Additionally, doubling the storage capacity has been shown to reduce energy loss in systems with high penetration of renewables (e.g., 80%, Solomon et al. [2014]). In order to avoid the reduction, storage capacities would have to increase, adding only 5 GW of storage to an energy system with an average demand of 60 GW reduced from 100 TWh to 40 TWh, thus more storage capacity leads to reductions in curtailment [Adamek et al., 2012, Sterner and Stadler, 2014]. The determination of the required storage demand remains a subject of ongoing investigation in the existing literature. However, understanding the storage demand is crucial for effectively balancing the intermittent nature of renewable power generation. The ability to store any excess energy, whether in the form of heat or power, enables mitigation of supply imbalances by subsequently discharging energy from storage during periods of deficit.

1.2 Analysis of available geological storage options

It is a common practice to classify storage technologies according to the conversion process involved, with two possible energy inputs, i.e., electricity and thermal energy and a wider range of energy outputs, such as electricity, thermal energy, gaseous and liquid fuels. Power-to-Power processes are classified as electrical energy storage, while Power-to-Thermal processes are part of thermal energy storage (TES). Power-to-Gas and Power-to-Liquids are respectively classified as chemical energy storages. Electricity energy storage can be classified into three types: mechanical, electrochemical and electrical. These classifications store energy in the form of kinetic or potential energy using mechanical processes, as chemical energy using reversible electrochemical reactions. Traditionally in all future energy system development pathways, geological storage options [Lunz et al., 2016, Sterner and Stadler, 2014]: pumped-hydro, compressed air energy storage (CAES), hydrogen and methane energy storage are considered, as the main storage technologies are present as large-scale storage options.

Geological subsurface can be used for three of four storage technologies mentioned above for energy storage applications. Porous formations are more widely distributed [Bachu et al., 2007, Bradshaw and Dance, 2005] and therefore may offer greater storage capacities. The same is true for pumped hydropower storage with over 165 GW of capacity in operation worldwide and a potential of 17.3 PWh [Hunt et al., 2020], relies on suitable topological conditions, whose application is limited to mountainous regions.

The prerequisite for geological energy storage in porous formations is the presence of a trap that retains the stored energy in the form of gas. These traps can take the form of stratigraphic or structural features, wherein the gas is confined to the upper portion or crest of a structure by a tight cap rock, effectively preventing migration of the stored gas. It is essential to have a sufficient pore volume to accommodate the desired stored volumes and target rates. Furthermore, the storage formation should exhibit adequate intrinsic permeability to support the planned flow rates for the storage application. The screening and characterisation of suitable geological traps present significant challenges, initiating an understanding of subsurface geology, petrophysical conditions and the quantification of site performance for different applications. These challenges are associated with geological uncertainties in porous formations and their spatial distributions. For instance, all sedimentary depositions can be influenced by regional geological activity, such as tectonic events or changes in sedimentary depositional environments. Addressing and quantifying such uncertainties is crucial to mitigate risks and ensure the successful implementation of storage application in geological porous formations.

Hydrogen and synthetic methane, along with compressed air energy storage in geological media, offer promising solutions to the challenges of energy storage and decarbonisation in the energy transition. Hydrogen, as a versatile energy carrier with high gravimetric energy density, holds immense potential for facilitating the integration of renewables and decarbonising various sectors [Schiebahn et al., 2015, Sterner and Stadler, 2014], including transportation and industry. Its high energy density enables efficient storage and transportation through geological porous media, utilising subsurface formations such as depleted oil and gas fields, aquifers and salt caverns. In parallel, the generation of synthetic methane through methanation provides a means of converting surplus renewable energy into a storable and transportable form. By utilising geological media for synthetic methane storage with a high volumetric energy density, it becomes possible to mitigate CO_2 emissions and integrate renewable energy sources with existing natural gas infrastructure. Leveraging geological formations as storage reservoirs for synthetic methane not only capitalises on the existing infrastructure, including pipelines and distribution networks, but also minimises the environmental impact associated with CO_2 emissions.

Furthermore, CAES is a highly promising and effective approach for large-scale energy storage, offering a valuable solution to address the intermittency of renewables. This storage process ensures a reliable and dispatchable energy supply, maintaining the balance of intermittent renewable energy generation [Adamek et al., 2012, Lund and Salgi, 2009]. The two main types of CAES plants are defined as diabatic and adiabatic. Diabatic CAES employs the use of natural gas or other fuel sources to heat the compressed air before releasing

it to generate electricity, resulting in greater efficiency but also carbon emissions. On the other hand, adiabatic CAES utilises advanced thermal storage techniques to reheat the compressed air without the need for additional fuel, making it a more environmentally friendly alternative. Notable examples of existing CAES sites include the Huntorf CAES plant in Germany, renowned for its diabatic technology and the McIntosh CAES plant in Alabama, USA [Succar and Williams, 2008]. These sites demonstrate practical application of CAES technology in real-world energy storage scenarios.

The combination of hydrogen and synthetic methane storage, along with CAES in geological porous media, presents a holistic approach to address the challenges of energy storage and enable the efficient integration of renewable energy sources into the grid. As the energy transition targets to double or triple the renewable energy capacity by 2030, the geological subsurface storage capacity becomes essential. However, the available storage potential and spatial distribution of storage sites is yet to be determined. Co-location of storage facilities with renewable energy sources can be considered beneficial to increase overall system efficiency [Pape et al., 2014]. Yet, there is a lack of assessment framework specifically for different storage technologies and their capacity assessment in porous media. The storage operation cannot be feasible without an integrated assessment framework that takes into account all components' specifications. Moreover, there are a few assessment frameworks available that consider the full storage operation process to gain detailed insight in 100% renewable energy systems.

1.3 Analysis of storage operation

As stated, storage classification takes into account the energy conversion process and the effectiveness of energy storage in geological media is determined by the duration of time for which it can store and provide energy. The duration of energy storage in geological media can be classified into three main categories: short-, medium and long-term storage types [Sterner and Stadler, 2014]. Short-term storage types can discharge power for up to a few hours at a time. Medium-term storage types can provide energy for several days or weeks. Long-term storage types can provide energy for seasonal periods. One short to medium-term storage option is CAES, which converts electrical or other forms of energy into mechanical energy and stores it in the subsurface. CAES has the capability to increase power plant output quickly in response to sudden increases in demand, making it a suitable option for balancing the intermittent output of renewables [Budt et al., 2016]. On the other hand, chemical energy storage is a long-duration storage option that involves an electrolysis pro-

cess for hydrogen or methanation for synthetic methane [Schiebahn et al., 2015]. Chemical energy storage has high energy density (i.e. 33.3 kWh/kg for hydrogen and 13.9 kWh/kg for synthetic methane), enabling it to store large amounts of energy in a small space and can be stored in geological porous media for several weeks or even seasonal periods.

Although storage processes may vary, they generally involve three critical steps: charging (loading), storing and discharging (unloading). These procedures are carried out using various components such as energy converters (for charging and discharging) with different efficiencies, storage media and peripherals: When all of these components work together as a single system, it forms a complete energy storage system. Accurately predicting and evaluating the storage process remains one of the main challenges to be addressed for ensuring the safe and efficient operation of energy storage systems. It is especially not trivial for the estimation of locally achievable charging/discharging rates as well as overall capacities and efficiencies. This can be connected with the geological uncertainty of formation spatial distribution, its petrophysical settings, as well as employed technical facilities.

The industry that has been operating energy storage for many years is the natural gas industry, where storage operations involve injecting natural gas into geological media, such as depleted gas fields, aquifer structures or salt caverns and withdrawing during times of high demand. This method plays an important role in ensuring adequate gas supply for seasonal energy demand. In Germany, there are 45 storage facilities with a total working gas volume of around 23 bcm (billion cubic meters), mainly operating in salt caverns, depleted fields and only 5 in aquifer structures [LBEG, 2021]. While Germany's gas storage infrastructure consists of two-thirds salt caverns and under one-third of porous media facilities, the situation is the opposite according to global experiences. This is because porous media formations are more commonly found in sedimentary basins worldwide [Bradshaw and Dance, 2005]. Depleted fields are often readily available for use as storage applications, as they already have the necessary infrastructure in place and location, making them a more attractive option for storage operators. Whereas storage in aquifer structures requires trap screening, site characterisation studies as well as facility design.

In order to store renewable energy, all three components of the storage system (charging, discharging and storage) must be processed and analysed. Surplus power is converted into a storable form, through energy conversion processes. As a storage media geological subsurface can be a suitable place for large-scale energy storage applications. The stored energy can then be used later as fuel or to produce other valuable items. However, accurately predicting and evaluating the storage process is one of the main challenges. To assess the feasibility of renewable energy storage, it is crucial to understand the fundamental processes

involved in charging (injection), discharging (withdrawal) and storing in geological formations. Since geological traps are commonly used as storage media, it is essential to identify and analyse them as an analogy with the natural gas industry. As one potential storage site can be used for different storage applications, there should be a selection criteria for development in the context of a site suitable for storage type in terms of capacity, rates and uncertainty. Moreover, having more than one type of storage application, e.g., hydrogen and compressed air energy, raises the question of how to schedule their use.

To assess the feasibility of renewable energy storage, it is imperative to comprehend the underlying fundamental processes associated with charging (injection), discharging (withdrawal) and storage in geological formations. As geological formations are commonly employed as storage mediums, it becomes crucial to identify and analyse them, drawing upon insights from the natural gas industry. Given that a single storage site can cater to multiple storage applications, the development of selection criteria is essential to identify sites suitable for specific storage types in terms of capacity, rates and uncertainty. Furthermore, the inclusion of multiple storage applications, such as hydrogen and compressed air energy, necessitates careful scheduling to optimise their utilisation.

1.4 Current and past research

Nowadays, there is growing global attention in the literature towards the utilisation of the geological subsurface for storage purposes, particularly as the penetration of renewable energy sources increases. This section presents an overview of the past and current research conducted in the field of energy storage in porous media. The aim of this section is to outline the research status and provide an understanding of the advancements made in this area. While this section offers a summary, each subsequent chapter will delve into a more detailed literature review of relevant studies associated with specific aspects of storage.

Back to the history, in case of storage of methane ideas were developed from the beginning last century and the first storage facility to balance seasonal and daily variations in demand for gas goes back to the early 1947 [Katz et al., 1959]. The concept of hydrogen storage was initially introduced by Sørensen in 1975 [Sørensen, 1975]. According to him, by the year 2050, with the proliferation of large-scale wind electricity generation, the need for suitable storage systems would arise. The idea of storing electrical energy through compressed air dates back to the mid-20th century [Budt et al., 2016]. In the 1960s, with emerging baseload generation, such as nuclear power and larger lignite coal-fired power plants, there was an

economic incentive to store low-cost off-peak power from baseload generation sources and utilise it during peak-load hours [Tuschy et al., 2002]. In 1978, the Huntorf power plant was built in north-western Germany and became the first commercial CAES facility worldwide [Succar and Williams, 2008, Tuschy et al., 2002]. The power plant was designed to transfer off-peak energy produced by the nuclear power plant to the high demand periods and also to stabilise the power grid when some baseload power stations failed during operating.

The literature on storage in salt caverns is well-researched, but when it comes to utilising porous formations for CAES, studies have been limited. The scarcity of data for storage site selection and the inherent complexity and uncertainties associated with porous media are the main reasons for this limitation. For instance, a study conducted in Pittsfield, Illinois examined the feasibility of CAES in a porous formation [Bui et al., 1990], subsequently, plans were made to construct the first commercial plant in Iowa. However, the planned CAES facility was halted due to unfavourable local geological conditions and energy market considerations [Holst et al., 2012]. This highlights the importance of understanding the subsurface and conducting comprehensive site characteristics. In the recent years, various studies have emerged focusing on subsurface potential assessment for suitable sites screening for different storage technologies in the context of renewable energy storage.

Mouli-Castillo et al. [2019] conducted an evaluation of potential subsurface storage capacity for CAES in the United Kingdom offshore region. The authors then estimate the pore volume of geological traps in sedimentary basins where legacy data from hydrocarbon exploration are available and geographically close to renewable energy sources. A modelling approach is used to predict the potential of CAES on a nationwide scale and the storage potential of offshore saline aquifers in the UK is estimated to be 77 TWh - 96 TWh. The estimated potential for the UK is equivalent to approximately 160% of the UK's electricity consumption for two winter months, with a round-trip energy efficiency of 54%-59%. To achieve the climate goals by the end of the century, it will be necessary to have more than 310 GW of grid-connected electricity storage globally by 2050.

According to Sopher et al. [2019], wind energy is experiencing growth in Sweden and the island of Gotland aims to achieve 100% renewable energy by 2025. The author highlights CAES as a viable option for energy storage on Gotland, utilising the Middle Cambrian Faludden sandstone as a storage reservoir. Extensive data analysis, including an unpublished database of over 2300 km of seismic data and 300 wells, was conducted to assess and identify the optimal location for energy storage. Furthermore, the authors briefly indicate that the southern part of the island is the most suitable area. Structural maps were used to identify favourable storage structures, with calculations estimating the energy storage ca-

pacity of one of the most promising structures in the Faludden reservoir to be between 84 MWh and 1308 MWh. Additionally, the cumulative high case storage capacities of all seven structures amount to approximately 4.31 GWh.

Carneiro et al. [2019] conducted the first potential assessment in Portugal to identify geological formations suitable for large-scale storage of renewables. The study emphasises the significance of energy storage in response to the increasing reliance on renewables within the country. The screening specifically targeted porous media, salt formations and igneous host rocks as potential reservoirs for various energy storage technologies. Feasibility assessments were then carried out to evaluate the suitability of each technology in different potential reservoirs. The study findings revealed a notable overlap between the locations of wind facilities and the selected reservoirs in salt formations and porous media formations located in the western part of Portugal. Conversely, solar sources, primarily concentrated in the southern region, were not found to be compatible with geological storage opportunities. Based on the overall results, the authors recommend focusing local-scale studies primarily on the western part of Portugal, particularly in the Lusitanian Basin, to investigate the potential utilisation of salt formations and porous media aquifers for storing surplus energy generated by nearby wind farms or the transmission grid.

In a study by Tarkowski [2017], seven potential locations for hydrogen storage in Poland were identified within the Carpathian Foredeep, all at depths below 2 km. These locations were selected based on an analysis of 85 depleted fields in the Polish Lowlands. In 2018, Lewandowska-Śmierzchalska et al. [2018] introduced a methodology that incorporates a decision support system to classify and rank appropriate geological structures for hydrogen storage. The methodology encompasses salt formations and porous formations (aquifers and depleted oil and gas fields). During their study, the authors discovered that the salt formation in the Gora region received the highest preference score from the decision maker, taking into account all decision-making criteria. In case of porous formations, the Chabowo and Przemysl fields obtained the highest preference scores.

TNO and EBN [2018] conducted a technical assessment report to evaluate subsurface storage options in the Netherlands for the country's energy transition. The assessment focused on technologies that could support the substantial expansion of renewable energy, ensure energy security and be implemented in the subsurface at depths exceeding 500 meters within the next 10-30 years. According to Juez-Larré et al. [2019], results show that substantial potential for subsurface storage, including depleted gas fields for hydrogen and synthetic methane storage (456 TWh and 1939 TWh, respectively) and salt caverns for natural hydrogen, methane and compressed air storage (43 TWh, 184 TWh and 0.58 TWh,

respectively). The assessment references the diabatic power plant in Huntorf site, Germany, for a simplified analysis of the potential for CAES including the lower operational pressure range.

However, no comprehensive screening has been conducted to identify suitable porous formation storage sites in Germany, particularly within the North German Basin, for renewable energy storage technologies such as CAES, hydrogen and methane. Additionally, there is lack of standardised estimation approaches for assessing different storage options in porous media and determining their respective capacities. The existing studies have not provided a unified framework to evaluate and compare the available capacities of various storage technologies in porous formations. Furthermore, previous studies have primarily focused on either chemical or mechanical energy storage without providing a comparative capacity analysis. In the context of energy storage applications, understanding the discharging/charging rate is a vital parameter in assessing the suitability of a site for a specific storage application. The storage flow rate serves as a crucial starting point for preliminary site planning, as the ability to discharge and charge the storage system at the desired rate is essential for meeting energy demands and ensuring a reliable and consistent energy supply.

Isothermal transient gas flow in porous media, based on Darcy's law developed by Muskat [1946] using partial differential equations, is a commonly employed approach to derive injection/withdrawal rates. Solutions for these equations are typically obtained through the utilisation of numerical methods, which can be time-consuming for storage site selection and performance assessment. Kushnir et al. [2010] developed an analytical solution to examine the gas flow dynamics in aquifer reservoirs of CAES plants, specifically focusing on the cyclic distribution of gas pressure within the reservoirs. The authors proposed an approximate solution that is applicable for analysing pressure variations in anisotropic reservoirs, considering the presence of partially penetrating wells. However, in many regional or basin-scale cases, geological data is limited and comprehensive consideration of petrophysical settings is not always feasible. To calculate achievable storage flow rates, the natural gas industry uses the inflow performance relationship [Katz et al., 1959]. Sopher et al. [2019] applied this approach to derive volumetric flow rates for CAES screened sites, ranging from 35 kg/s to 262 kg/s, but excluding the allowable storage pressure limits at the wellbore.

Several studies have been conducted on applying numerical simulation to explore geological storage in porous media, considering both petrophysical characteristics and technical designs of storage wells. Oldenburg and Pan [2013] simulated a hypothetical CAES porous formation storage site with an anticline structure and demonstrated the feasibility of CAES operation using a single wellbore at the crest of the structure. The results suggest that CAES

in porous media is capable of storing energy effectively, although the energy storage density within the reservoir may vary spatially due to pressure gradients. Wang and Bauer [2017] conducted a feasibility study to explore the possibility of utilising CAES in sandstone formations. They examined the potential of replacing two salt cavern units with a synthetic anticline storage structure, using the Huntorf site as a reference storage plant. Simulation results indicated that a 20 m-thick storage formation with a permeability of 1000 mD and utilising six wells, could support the required continuous power output. However, none of these studies assessed the feasibility of porous media CAES considering site-specific power plant setup. In a recent study, Pfeiffer et al. [2021] found that the behaviour of CAES in porous media varied depending on the surface power plant topology, emphasising the need for site-specific plant design for potential storage sites. Results from these modelling studies show that, in principle, large-scale CAES within porous reservoirs is feasible. However, most of them are based on synthetic storage models and surface power plant settings are traditionally based on reference salt cavern power plant topology.

Pfeiffer and Bauer [2015] developed a hydrogen storage scenario in porous media by conducting numerical simulations. The storage approach included injecting nitrogen as a cushion gas during the build-up phase within an aquifer structure. To meet the regional electricity demand in Northern Germany, a weekly hydrogen of 129 million sm^3 was employed. The study suggested that optimised injection schemes, including shut-in periods during the initial filling process, could enhance the storage performance. Feldmann et al. [2016] conducted a study to investigate the hydrodynamic and mixing processes involved in hydrogen gas storage in porous media. They performed a numerical case study in a depleted gas reservoir, simulating a simplified seasonal pattern consisting of 5 years of build-up phase charging followed by 5 years of seasonal cyclic operation. The study focused on the withdrawal of an annual gas volume of 107.7 million sm^3, analysing various physical phenomena associated with the storage process. Sainz-Garcia et al. [2017] showed that the geological trap in the San Pedro saline aquifer is suitable for seasonal hydrogen storage. The developed model showed that no hydrogen crossed the structure spill point and no viscous fingering occurred despite the high density and viscosity contrast between hydrogen and water. Although their research demonstrates the average performance in the aquifer, storage sites can cover up to 15% of city electricity consumption via the re-electrification process. All the mentioned studies employed highly detailed numerical models that varied storage settings and configurations, but they were all based on simplified assumptions of renewable fluctuations, either on a weekly or seasonal basis, without considering the stochastic fluctuations in both demand and supply expected from variable renewables.

Numerous publications have focused on the integration of energy storage into renewable

power systems with stochastic supply and demand patterns [Crotogino et al., 2010, Gabrielli et al., 2020, Lund and Salgi, 2009] however, none of them have explicitly addressed the intricate geological storage options in porous media and their significance in future energy systems. This gap can be attributed to the disparity in solution approaches between geological storage, which necessitates precise process discretisation and energy system modelling, which relies on distinct mathematical optimisation schemes. Therefore, there is a need to develop a methodological framework that captures the intricacies of geological storage processes while considering the governing physical processes in the subsurface, while also ensuring adequate simplification to align with the specific modelling requirements of renewable energy systems.

The necessity of a comprehensive numerical storage model lies in its ability to accurately represent the various induced processes associated with typical subsurface use options. Bauer et al. [2013] highlighted that any subsurface storage utilisation leads to induced effects, which can be broadly classified based on the governing physico-chemical processes responsible for transmitting these effects, such as thermal, hydraulic, mechanical and chemical effects, along with their interconnected feedback mechanisms. As previously stated, there are no analytical solutions for non-linear three-dimensional fluid flow phenomena occurring within porous media, and the majority of quantitative solutions rely on numerical methods. Storage models are frequently expressed as a set of partial differential equations that incorporate the mass conservation for fluid phases with Darcy's law and appropriate initial and boundary conditions [Muskat, 1946]. In the context of energy storage applications, certain undesirable effects may be site-specific, necessitating the adoption of a virtual scenario simulation approach that employs fully parameterised storage sites to evaluate the quantitative impacts of these effects.

For instance, in the natural gas industry, storage processes can have a significant hydraulic impact, potentially resulting in undesirable outcomes such as gas leakages. Evans and West [2008] conducted an extensive investigation and identified a number of incidents predominantly occurring in natural gas storage sites, characterised by varying levels of severity and underlying causes. Notably, the majority of these incidents were attributed to infrastructure failures and human error, rather than geological factors. Nevertheless, the authors highlighted several incidents associated with sites that build aquifer structures. One noteworthy case was reported in sandstone reservoir within the Thaynes formation at the Leroy site.

Chen et al. [2013] conducted a study on the Leroy storage site, which operates as an aquifer storage setting characterised by an anticlinal structure with fault boundaries. During high-

pressure storage operations at this site, gas leakages occur through different pathway windows, including faults, insufficient cap rock and leaky wells. The study's three-dimensional (3D) reservoir analyses highlighted the direct relationship between gas leakage and reservoir pressure, confirming that controlling operating pressure can effectively mitigate leakage. Pressure relief mechanisms effectively regulate and manage the cumulative volumes of brine and gas leakage. Understanding and quantifying these pressure relief mechanisms enable operators to implement appropriate measures to control reservoir pressure and mitigate hypothetical gas leakage, as seen in renewable energy storage applications like hydrogen or synthetic methane. The authors also suggest investigating fault zone parameters to assess potential leakage scenarios and determine gas leakage rates. For instance, in the case of semi-permeable faults, leaked gas has the potential to accumulate in secondary aquifers, as demonstrated in the Kaluga UGS with an active working gas volume of 410 million m^3 [Soldatkin, 2010]. Evans and West [2008] emphasise the importance of investigating fault systems within storage formations, including their sealing capacity and behaviour under diverse conditions. Thorough modelling, assessment and quantification of uncertainties associated with fault zone parameters are essential. Through diligent research of this nature, a more profound understanding of the intricate dynamics of fault systems can be achieved, thereby enhancing knowledge of their implications for optimal storage operations.

1.5 Aims of this thesis

This thesis aims to evaluate geological storage options for promoting a sustainable energy transition by addressing challenges and bridging the knowledge gap associated with storage in geological formations. It explores storage demand in future energy systems with significant shares of renewables, highlighting the necessity of large-scale solutions like hydrogen/methane or compressed air energy storage in geological formations. Numerous studies focus on assessing geological potential and quantifying storage capacity in sedimentary basins. Site selection and design must consider capacity, charging/discharging rates and limitations. However, there is a knowledge gap in quantifying the feasibility of porous media storage in renewable energy systems, particularly in Northern Germany, with varying renewable sources. Filling this gap is crucial for effective energy system planning. Sensitivity studies are needed to quantify potential impacts and undesired effects, particularly gas or formation fluid leakages during the hydraulic process of storage operations. Building upon the existing research and knowledge, the primary objective of this thesis is to address the following research questions and provide solutions to each of them:

- How can the spatial dimensions of storage sites be determined and what are the potential storage sites for hydrogen, synthetic methane and compressed air energy storage types and how can their capacity be quantified?

- How can potential storage sites be optimally utilised, taking into account the dimensions, limitations and suitability for different energy storage applications?

- How can geological storage options be effectively integrated into renewable energy systems, ensuring flexibility in storage facilities to accommodate time-dependent required rates and capacities?

- What are the essential physical processes that need to be retained during storage operations? How can geological storage be approximated to simplify the modelling process while still maintaining technical installation flexibility for facility design?

- What are the key considerations for evaluating the potential for stored gas leakage from adjacent or intersecting fault systems in energy storage applications? Are there any regulatory mechanisms that can control leakage effects?

1.6 Structure of this thesis

Following this introduction (Chapter 1), the subsurface storage potential and technology comparisons within the North German Basin are investigated in Chapter 2. A dedicated 3D structural model is developed based on various geological dataset, identifying suitable formations for energy storage. The analysis includes parameterisation, storage structure identification and estimation of pore and energy storage volumes. Comparative assessments are conducted for hydrogen, synthetic methane and compressed air storage. Chapter 3 focuses on a detailed investigation of a potential site for PM-CAES application, considering renewable energy integration, different surface plant configurations and storage well settings. In Chapter 4 a semi-analytical solution is presented, which aims efficiently assess geological storage processes in future energy systems, accurately simulating operations and capturing storage performance. The model aims to provide a reliable and time-saving alternative to numerical models, enabling rapid site assessment and optimisation of renewable energy storage applications. In Chapter 5, the simulation and quantification of gas leakage effects on methane storage are explored using a representative 3D model with fault systems. Finally, in Chapter 6, the results from Chapters 2, 3, 4 and 5 are discussed and summarised.

2 Subsurface renewable energy storage potential assessment

Part of the content in the following chapter has appeared in the Renewable and Sustainable Energy Reviews:

Firdovsi Gasanzade, Wolf Tilmann Pfeiffer, Francesco Witte, Ilja Tuschy and Sebastian Bauer (2021) Subsurface renewable energy storage capacity for hydrogen, methane and compressed air–A performance assessment study from the North German Basin. doi:10.1016/j.rser.2021.111422

2.1 Introduction

The transition from a conventional carbon-rich energy system to a renewable carbon-free energy system with significantly reduced CO_2 emissions poses one of the greatest challenges to modern society. Many countries worldwide have committed to reducing greenhouse gas emissions, diversifying electricity and energy generation and thus curbing anthropogenically induced climate change [IPCC, 2014]. In Germany, the so-called 'Energiewende' therefore defines a target of renewable energy sources, such as wind or solar power, accounting for 80% of gross electricity consumption by 2050 and 45% of gross energy consumption by 2040 [BMWi, 2018]. Renewable sources currently generate 42% of gross electricity and 17% of gross energy consumption [UBA, 2020]. However, one major drawback of these renewable energy sources is the strongly fluctuating nature of the energy supply, caused by variations in wind or sunshine conditions on an hourly and up to seasonal time scale, and may significantly impair the stability and reliability of the energy and power supply system [Adamek et al., 2012, Gerhardt et al., 2015, Weitemeyer et al., 2015]. Energy storage offers one means of buffering these fluctuations and enabling the requisite high proportions of renewable energy [Gerhardt et al., 2015, Research and IEA, 2016]. This will require large-scale grid storage capacities along with daily to seasonal storage [Inage, 2009, Luo et al., 2015]. Required storage capacity predictions range from about 70 GWh for short five-hour cycles and 7.5 TWh for 17 day cycles [Adamek et al., 2012] to as much as 50 TWh for the longer term in Germany [Klaus et al., 2010].

The geological subsurface may provide large storage capacities as well as the wide range of cycle times and power rates required [Crotogino et al., 2010, Kabuth et al., 2017, Ma et al., 2018]. Available geological storage technologies include compressed air energy storage, syn-

thetic hydrogen or methane storage and thermal energy storage, which may be located either in salt caverns or in porous geological formations [Bauer et al., 2013]. In northern Germany, the North German Basin (NGB) provides potential storage sites in both porous sandstone formations and salt caverns [Kaufhold et al., 2011, Reinhold et al., 2011], while suitable porous storage sites also exist in the south of the country, albeit to a much lesser degree [Gerling, 2010].

While salt caverns offer suitable storage environments [Caglayan et al., 2020, Evans and West, 2008, Lankof and Tarkowski, 2020, LBEG, 2018, Parkes et al., 2018], geological salt formations may not be present in locations at which storage capacity is required [Donadei and Schneider, 2016]. Porous formations are more widely distributed [Bachu et al., 2007] and therefore potentially offer greater storage capacities.

A total of 715 gas storage sites currently exist worldwide, hosting 396.8 billion Nm^3 of natural gas, and this number is increasing [Kabuth et al., 2017, LBEG, 2018]. Storage sites in porous formations mainly use depleted oil and gas fields and contribute significantly to their total capacity [Holloway et al., 1996, LBEG, 2018]. In Germany, about 17 storage sites operate in porous formations with about 9.3 billion Nm^3 of working gas volume [LBEG, 2018]. These sites use methane produced in natural gas fields as storage gas and are mainly intended to dampen seasonal fluctuations in gas demand. However, in recent years, porous formations have also been considered for energy storage in combination with power-to-X technologies for storing surplus power either as mechanical energy using CAES [Mouli-Castillo et al., 2019, Oldenburg and Pan, 2013, Sopher et al., 2019, Succar and Williams, 2008, Wang and Bauer, 2017] or as chemical energy (i.e., synthetic hydrogen or methane) produced from surplus power [Ma et al., 2018, Pfeiffer et al., 2017, Sainz-Garcia et al., 2017]. These studies have demonstrated that porous geological formations provide promising large-scale storage options on both the shorter and longer time scales by providing the required storage capacities as well as flow rates considering the heterogeneity of the permeability distribution [Pfeiffer and Bauer, 2019], storage gas dissolution [Li et al., 2018] or geochemical effects [Hassannayebi et al., 2019, Wang and Bauer, 2019].

To address the needs of the energy supply system with increasing proportions of renewable energy production, not only are energy storage sites required but these sites must also be suitably placed in relation to the main energy generation and consumption areas [Pape et al., 2014]. A screening and assessment of available subsurface storage sites analogous to the effort undertaken for CO_2 storage is required [Ajayi et al., 2019, Bachu et al., 2007, Bauer et al., 2012]. The overall storage capacity of European countries was assessed for carbon capture and sequestration (CCS) by Holloway et al. [1996], outlining potential host rock

formations. In Germany, nationwide screening for CO_2 onshore porous formation storage identified the NGB as the main suitable storage region by virtue of the abundant availability of porous storage formations and cap rock [Reinhold et al., 2011] . For CCS, storage capacity estimation indicates that a capacity estimate based on a characterisation of the individual traps yields conservative estimates compared to a formation-based approach [Knopf and May, 2017]. Detailed numerical site-specific studies have been used to assess achievable CO_2 storage capacities for individual sites, highlighting the importance of the regional setting [Birkholzer et al., 2015, Kissinger et al., 2014, Mitiku and Bauer, 2013, Watson et al., 2014]. The main cap rock and storage formations have recently been mapped by Jähne-Klingberg et al. [2014] in the offshore German North Sea sector, and thus both onshore and offshore storage formations have now been characterised. An assessment of potential subsurface storage capacity for CAES was performed for the United Kingdom offshore region by Mouli-Castillo et al. [2019] and for Gotland, Sweden by Sopher et al. [2019]. Both identified a significant number of potential storage sites to cover the energy storage demand relating to the transition towards electricity generation by wind power. The Dutch subsurface has also been shown to provide a large potential storage capacity of 1482 billion Nm3 gas in place (GIP) for chemical energy storage, mainly in depleted gas fields [TNO and EBN, 2018]. The first regional scale assessment in Portugal for various storage types demonstrated that CAES and chemical energy storage in combination with power-to-gas are the most suitable for the Portuguese geological context [Carneiro et al., 2019]. However, no systematic screening for porous formation storage sites with respect to renewable energy storage technologies, CAES, synthetic hydrogen and methane as well as an estimation of the respective potential storage capacities for the individual storage gases, has been performed for the NGB.

As energy shortage periods may vary from hours to weeks, compressed air can be utilised for storage applications covering hourly to daily energy shortages, while the use of chemical energy carriers, such as hydrogen or methane, facilitates weekly to seasonal storage applications. It is important to characterise storage sites not only with respect to capacity but also with respect to the achievable energy loading and unloading rates. Therefore, the achievable injection and withdrawal rates are of critical importance, as these are linked to injectivity and thus to reservoir quality and the petrophysical parameters of the porous formation used. This is particularly the case for CAES, as the high cycle number required for renewable energy storage demands high rates and low flow resistance in the storage formation [Mouli-Castillo et al., 2019, Wang and Bauer, 2017].

As energy storage demand increases with the increasing use of renewable energy sources, competition for suitable subsurface storage sites may occur [Bartel and Janssen, 2016]. This may be due to a single storage site's suitability for multiple storage technologies as well as

induced effects from nearby storage sites reducing achievable capacity [Bauer et al., 2013]. Subsurface spatial planning of the geological storage formations is thus required as well as the development of suitable tools and methods for assessment [Kabuth et al., 2017], enabling a comparison of the energy storage potential for each storage technology considered for an individual site. While mechanical energy storage (i.e., CAES) has a high cycle life, low cost and high round trip efficiency [Pape et al., 2014, Sterner and Stadler, 2014], chemical energy storage (i.e., synthetic hydrogen or methane storage from a power-to-gas conversion) has a long system lifespan and low round trip efficiency [Klaus et al., 2010, Ma et al., 2018, Sterner and Stadler, 2014], but is easily integrated within the existing gas infrastructure [Pape et al., 2014] and can be more readily transported. While chemical energy carriers, such as hydrogen and methane have an inherent energy capacity, making it straightforward to calculate the amount of stored energy in a structure, an exergy analysis of the complete systems (i.e., including the above-surface power plant as well as the subsurface storage site) is required to determine the retrievable energy (i.e., the energy reclaimed from the storage for CAES) [Osterle, 1991]. The first exergy analysis of CAES performance was performed by Osterle [1991], while recently for cavern-based CAES technology, He et al. [2017] have determined the exergy of stored gas for different operational modes. To date, however, exergy analysis has not been applied to characterise CAES or hydrogen and methane storage in porous media, and thus, no systematic comparison of the individual geological storage options in terms of their retrievable energy for porous media storage has been performed and reported in the literature.

Carneiro et al. [2019] used publicly available datasets transferred to a GIS system and screened the available geological layers. They were thus able to identify priority sites for subsurface energy storage using CAES and gas storage technologies at the national level. At the regional level, Mouli-Castillo et al. [2019] used a Monte Carlo approach combined with a simplified storage site model approach and datasets derived for CCS storage to show that suitable storage potential for CAES is available in the United Kingdom offshore aquifers to accommodate the power fluctuations expected from offshore wind power plants. Using volumetric information from depleted gas fields, the potential storage capacity for gas storage can also be derived based on the caloric values of the stored gases [TNO and EBN, 2018].

In this study, therefore, a systematic screening and evaluation approach to assess the site-specific energy storage potential for synthetic hydrogen, methane and CAES in porous formations is developed and applied to part of the NGB. To facilitate a consistent comparison of potential storage sites with respect to the retrievable energy, the exergy is determined for these storage options and each potential storage site individually. Additionally, storage deliverability is evaluated as an additional criterion for site suitability. Thus, a consistent

ranking of the individual potential storage sites with respect to retrievable energy capacity and the loading/unloading rates is obtained as well as the total available cumulative storage potential, complemented by an uncertainty analysis of petrophysical parameters. Together with information from energy system modelling and the location of the individual storage sites, this enables an informed decision on the optimal use of an individual site as a basis for subsurface spatial planning of geological energy storage.

2.2 Methodology

2.2.1 Geological setting

To assess the subsurface storage potential, spatial distributions of the main storage and cap rock formations in the study area are required. The study region is part of the NGB, which is one of the largest basins within the Central European Basin System, and its geological structure has been investigated in some areas in recent decade [Arfai et al., 2014, Baldschuhn et al., 2001, Hese, 2012, Jähne-Klingberg et al., 2014, Wolf et al., 2014]. In the present study, all data from these sources were combined into one 3D structural geological model, which incorporates all geological formations from the Zechstein to the Upper Cretaceous, along with the salt structures formed through halokinesis as well as the associated fault systems (see Fig. 2.1). The study area contains almost all main regional tectonic structures, from the Eastholstein block to Entenschnabel's graben systems. The dimensions of the structural model are 550 km x 150 km horizontally, with the deepest point at 10.7 km depth and the spatial resolution being 100 m. For the three main storage formations (i.e., the Quickborn–Volpriehausen (Middle Buntsandstein), the Rhaetian (Upper Keuper) and the Dogger (Middle Jurassic)), as well as their respective cap rock formations, depth horizon maps were created (Fig. 2.2) using the Petrel E&P platform [Schlumberger Ltd., 2018]. The Middle Buntsandstein lithostratigraphic unit has a deposition thickness of over 300 m within the Westholstein block [Baldschuhn et al., 2001, Donadei and Schneider, 2016, Hable et al., 2011] and comprises the Quickborn–Volpriehausen, the Detfurth, the Hardegsen and the Solling formations, which are characterised by basal discontinuities that extend regionally across large areas [Hable et al., 2011]. These are tectonostratigraphic units bounded by unconformities that can be recognised across most of the NGB area. The Quickborn–Volpriehausen sandstones form the base of the Middle Buntsandstein and have a significant thickness of up to 100 m (Westholstein trough), with suitable reservoir properties [Hable et al., 2011] for subsurface storage [Bauer et al., 2013, Benisch and Bauer, 2013, Hese, 2012]. The formation is present in most of the study area, with a depth range of

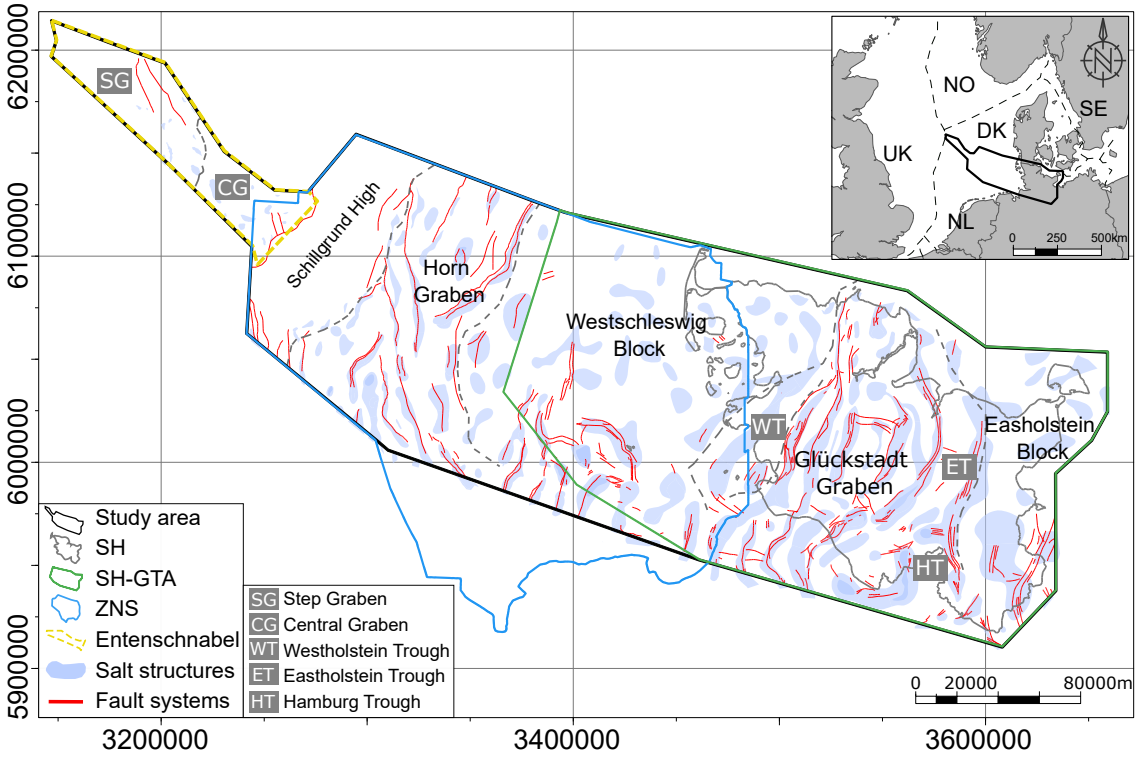

Figure 2.1: Study area with main structural elements from Entenschnabel (dashed yellow line) to Eastholstein block. The WGS84 is applied as a coordinate reference system. The blue solid outline delineates the area of the Central North Sea sector (ZNS); the green solid outline delineates the area of the Geotectonic Atlas of Northwestern Germany [Baldschuhn et al., 2001] and the German North Sea (GTA) within Schleswig-Holstein (SH).

600–10,000 m (see Fig. 2.2c).

Within the Keuper lithostratigraphic unit, only the Rhaetian formation, as part of the Upper Keuper sandstone-claystone sequence, is considered a suitable potential storage formation [Hable et al., 2011, Hese, 2012, Pfeiffer et al., 2017]. Within the study area, the Rhaetian formation is present between the Westschleswig Trough and the Eastholstein Block within a depth range of 300–5,700 m (Fig. 2.2b), exhibiting a lithology varying from sandstones to clay-dominated, with intercalated fine sandstone layers and a thickness of up to 300 m [Baldschuhn et al., 2001, Hable et al., 2011, Hese et al., 2017].

Distribution of the Dogger sandstones from the Middle Jurassic is limited to the salt dome flanks [Hable et al., 2011, Hese, 2012] owing to erosion in large parts of the study area [Baldschuhn et al., 2001, Doornenbal and Stevenson, 2010]. The depth of the Dogger formation varies locally to between 600 m and 3000 m, with the greatest depth to the west of the Glückstadt Graben (Fig. 2.2a). Total thickness varies between 100 m and 300 m [Bald-

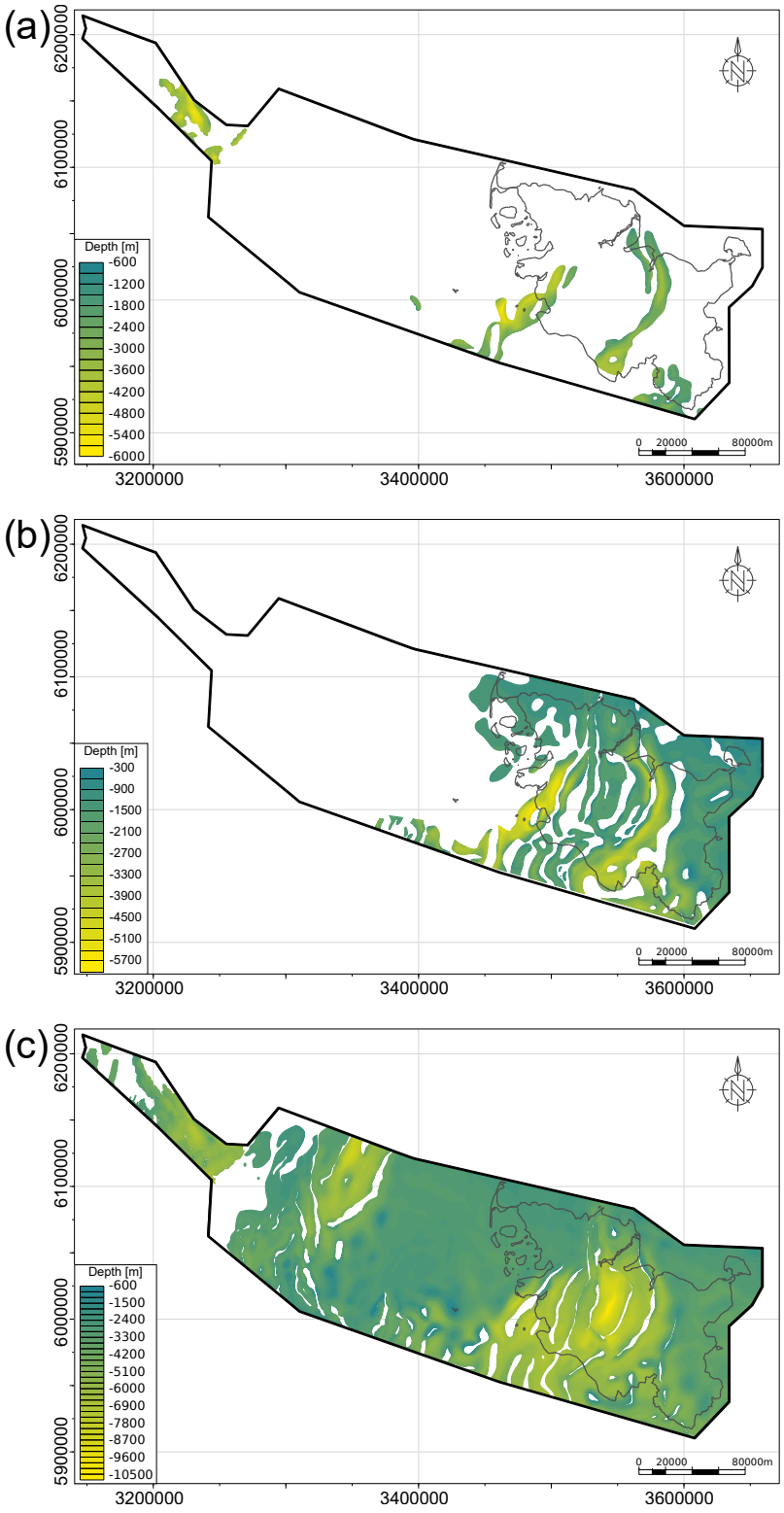

Figure 2.2: Structural map of storage formation distribution within the study area: (a) Dogger formation depth in range 600–6000 m; (b) Rhaetian depth in range 300–5000 m; (c) Quickborn–Volprienhausen in range from 600–10000 m.

schuhn et al., 2001, Hese, 2012]. The Dogger formation's suitable reservoir properties are verified by the existing or depleted oil and gas fields [Boigk, 1981].

2.2.2 Structure screening

Key criteria for site selection for geological energy storage are storage capacity, storage deliverability and storage containment. Geological traps, which provide containment as well as capacity, can be categorised into structural traps (anticline, fault, salt dome flank), stratigraphic traps (pinch-out, unconformity, reef) and combination traps (flank trap sealed by pinched-out or confined to fault blocks) [Levorsen, 1956]. These three trap types were considered potential storage sites and included in the structure screening. Structural traps are the most common types of geological traps and are defined by fault and fold geometries as a result of structural uplift and differential compaction, while stratigraphic traps are formed by depositional processes that produce paleo-topographic heights encased in impermeable material [Levorsen, 1956]. Halokinesis must be considered for the identification of traps at salt dome flanks, as the salt dome may intrude upwards into the overlying sediments and form the cap rock for a storage formation at the dome flank. Geological traps for the study area considered here were identified using spill-point analysis, where the spill point of the trap is determined by the shallowest depth horizon contouring that would lead to spillage. A contour increment of 20 m is applied for all three potential storage formation horizons with the ensured presence of cap rock formations.

Chemical storage technologies, such as hydrogen or methane porous medium storage, and mechanical energy storage have no depth limitations within the upper 10 km of the earth's crust in terms of the phase properties (such as phase transitions) of the stored gas, while such limits do exist, for example, for carbon sequestration [Bachu et al., 2007, Mitiku and Bauer, 2013]. Therefore, no depth restrictions were applied. In light of the interlayering of low permeability materials, it is assumed that the total thickness of a storage formation – as determined from the geological model – does not contribute to storage, but rather a net or pay thickness is applied for each storage formation to account for the effect of such low permeability zones within them. Requirements for trap identification are a formation thickness of more than 10 m pay thickness, a cap rock thickness of more than 20 m, and suitable petrophysical properties of the storage formation (see Table 2.1), which are defined here as porosity of greater than 10% and permeability greater than 100 mD, to support the required injection and withdrawal rates during gas storage [Bennion et al., 2000, Katz et al., 1959]. Furthermore, anticline traps with a high fold interlimb angle (i.e., of the gentle fold type) are excluded owing to fast pressure dissipation as a result of gravity drainage, which leads to small withdrawal rates as well as increased residual trapping and thus loss of the storage gas [Katz et al., 1959]. Screening the newly developed structural model while considering these criteria allowed for the identification of 74 potential storage sites. Of these, 11 are in the Dogger, 19 in the Rhaetian and 44 in the Quickborn–Volpriehausen formations. Because

Table 2.1: *Summary of the general criteria for site screening.*

Criteria	Requirements
Formation lithology	Sandstone
Cap rock lithology	Shales, clays, carbonates and evaporites
Formation pay thickness	≥10 m
Cap rock thickness	≥20 m
Porosity	≥10%

the Quickborn–Volpriehausen formation occurs in most of the study area (2.2c), potential storage sites in this formation are also distributed throughout the entire study area. Of the potential storage sites identified, 6 in the Dogger formation, 2 in the Rhaetian formation and 29 in the Quickborn–Volpriehausen formation are located offshore, with the corresponding onshore numbers being 5, 17 and 15, respectively. Thus, half of all identified storage sites are onshore sites. Most (i.e., 39) of the identified storage sites are formed by structural traps. For each storage site, a detailed attributes catalogue was compiled, documenting the trap geometry type, existing fault systems, and cap rock and formation information.

2.2.3 Storage capacity

To assess storage capacity V_g, the volume of the theoretical free gas (i.e., mobile gas) phase in the pore space of the storage formation if used is estimated and reported as GIP at standard conditions of 273.15 K and 10^5 Pa in this study:

$$V_{gas} = \frac{Ah\phi(z)S_g(\phi(z))}{B_g(Z_f(p,T))} \tag{2.1}$$

where A [m^2] is the area of storage closure, h [m] is the net formation thickness, φ(z) [-] is the depth-dependent formation porosity, S_g [-] is the maximum gas saturation, B_g [rm^3/sm^3] is the gas formation volume factor, Z_f [-] is the dimensionless gas compressibility Z-factor at formation pressure p [Pa] and temperature T [K].

The storage closure area A is determined from the geological model by calculating the area of the spill plane by summation of the respective grid cell areas. Gridded formation inter-

face surfaces are used for geometric modelling and for spill-point analysis, using a 100 m x 100 m grid resolution.

The net formation thickness h, accounting for vertical formation intervals of low permeability, can be derived from borehole log or core analysis data and depends mainly on the depositional environment and structural history of each storage site. For the study region, Hese et al. [2017] provided detailed maps of cumulative net thickness for all three storage formations that included, consideration of lithology and thickness trends. The Rhaetian sandstone thickness is reduced to 75 m in the Eastholstein Trough to the Westholstein Trough (Fig. 2.2b), while the formation has been fully eroded in the Westholstein block. The thickness of the Quickborn–Volpriehausen formation shows the opposite trend [Baldschuhn et al., 2001, Hese et al., 2017, Wolf et al., 2014], with an average total thickness between 175 m and 250 m and a net formation thickness of about 45 m [Geluk, 2005, Kortekaas et al., 2018, Reinhold et al., 2008]. The average net thickness of the Dogger formation varies between 10 m and 30 m [Boigk, 1981, Goffey et al., 2018, Hable et al., 2011]. In the present study, conservative estimates of the net formation thickness of 10 m to 20 m for all storage sites in all three storage formations were used.

The porosity of a potential storage formation can be obtained directly from measurements of drilling cores or indirectly from wireline well logs. Fig. 2.3 illustrates the limited porosity versus depth data available for the study region [Thomsen, 2013]. The literature reports porosity values for the Quickborn–Volpriehausen formation ranging from 12% to 21% [Reinhold et al., 2011] and for the Rhaetian from 15% to 30% [Hable et al., 2011]. Porosity values of greater than 20% are mainly found in the Rhaetian sandstone layers at depths of less than 2500 m [Thomsen, 2013]. The porosity of the Dogger formation at the Eastholstein Trough is in the range of 20%–40% [Dethlefsen et al., 2014], with a median of 22%–24% [Reinhold et al., 2011] for the study region. Additional porosity measurements exist for the northern boundary of the study area [Kristensen et al., 2016], where the overall porosity for the Buntsandstein is 15%–25%, with values greater than 17% for the Quickborn–Volpriehausen [Olivarius et al., 2015] and 15%–30% for the Rhaetian formation [Kristensen et al., 2016].

Formation porosity was observed to decrease with increasing burial depth (see Fig. 2.3 for correlations by Kristensen et al. [2016]) as a result of mechanical compaction [Gluyas and Cade, 1997], which can be correlated as follows:

$$\phi(z) = a \cdot exp^{\left(\frac{bz}{c+dz}\right)} + \gamma \tag{2.2}$$

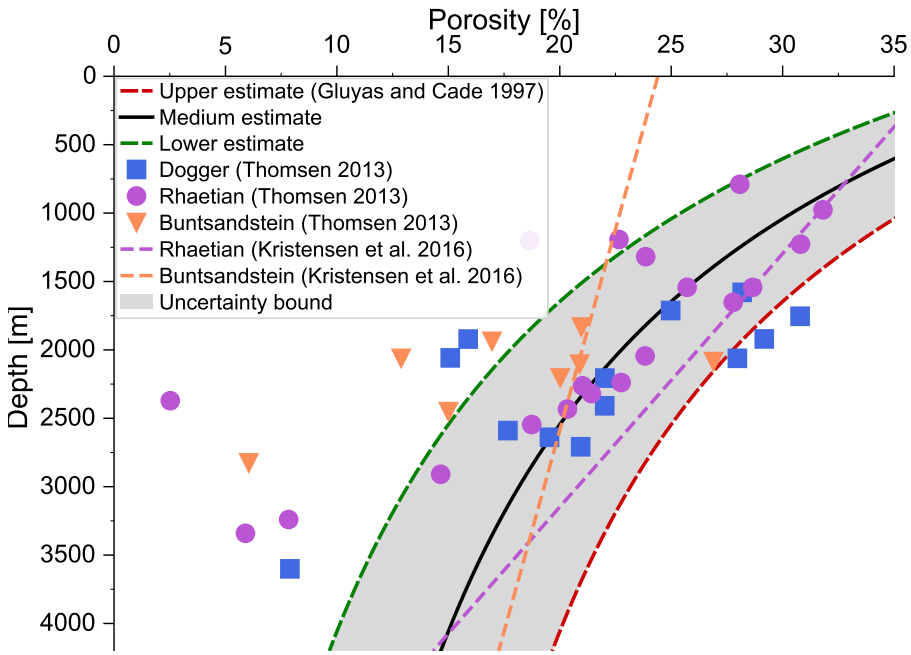

Figure 2.3: Porosity correlation for storage formations against depth. Dashed lines represent porosity correlation models relating to the study area; the symbols represent 'average well' porosity data within the study area [Thomsen, 2013], and the grey area represents the uncertainty range considered in this study.

where a through γ are the parameters with values as given in Table 2.2. The global correlation for the depth dependence of porosity for sandstone formations from Gluyas and Cade [1997] is used in this study as an upper estimate for the depth-dependent porosity (see equation 2.2 and Table 2.2). For a medium estimate, this porosity is reduced by 0.05, and for a lower porosity estimate, this value is reduced by 0.1 (see Fig. 2.3 and equation 2.2). This selection of the porosity–depth relationship covers most of the available data points as well as existing correlation models in the study area (compare 2.3) and forms the basis for an uncertainty quantification of the estimated stored energy, stored exergy and storage deliverability (see Section 2.2.4). Some of the low porosity values shown in Figure 2.3 are not represented by these correlations because the lowest occurrence of storage sites in the Rhaetian formation within the study area is at a depth of 2500 m, whereas the low porosity values are reported at depths greater than 2500 m and thus are not representative of the

Table 2.2: *Parameters for Eq.2.2*

Parameters	a	b	c	d	γ
Upper estimate [Gluyas and Cade, 1997]	0.5	10^{-3}	2.4	$5x10^{-4}$	0
Medium estimate	0.5	10^{-3}	2.4	$5x10^{-4}$	-0.05
Lower estimate	0.5	10^{-3}	2.4	$5x10^{-4}$	-0.1

study area. However, those small values indicate that porosity may be lower locally than is predicted using equation 2.2.

The pore volume [rm^3] of an individual storage site was calculated by multiplying the storage closure area with the net formation thickness and the porosity at the respective depth. Not all pore space can be used for gas storage, as not all formation water can be expelled from the pores during gas injection. The irreducible residual water saturation varies within the range of 0.05–0.3 and has a close statistical relationship with formation porosity and permeability [Katz et al., 1959]. Applying Ahmed's relationship for residual water saturation, the maximum gas saturation is parameterised here as a function of porosity and permeability k [mD] as Ahmed [2018]:

$$S_g = 1 - \frac{4.14\phi(z)}{[k(\phi(z)) - 0.02exp^{31.93\phi(z)}]^{0.28}} \tag{2.3}$$

The physical properties of the stored gas can be derived from the formation temperature T [K] and pressure p [Pa], both of which vary with depth. Assuming a normal pressure regime, formation pressure is determined using a hydrostatic pressure gradient of 10.5 MPa/km [Holloway et al., 1996]. Formation temperature was determined using an average temperature gradient of 30 K/km representative of the study area [Hese et al., 2017]. For each storage gas, the corresponding gas formation volume factor B_g is determined to convert the fluid volume at reservoir conditions to the fluid volume at standard surface conditions:

$$B_g = \frac{p_s T Z_f}{p T_s} \tag{2.4}$$

where $p_s = 10^5$ Pa and $T_s = 273.15$ K are the standard pressure and temperature. The compressibility Z-factor Z_f is determined using a correlation from Papay [1968]:

$$Z_f = 1 - \frac{3.53(p/p_{crit})}{10^{0.9813(T/T_{crit})}} - \frac{0.274(p/p_{crit})^2}{10^{0.8157(T/T_{crit})}} \tag{2.5}$$

where p_{crit} [Pa] is the critical pressure and T_{crit} [K] is the critical temperature of the storage gas and the numerical coefficients are given by Papay [1968].

Equation 2.1 is applied to estimate the pore volume for each potential storage site, identified by geometrical modelling and spill-point analysis as well as the GIP for each storage

gas considered. The chemical energy storage potential for methane and hydrogen is then calculated using their lower heating values of 13.9 kWh/kg and 33.3 kWh/kg at standard condition, respectively.

2.2.4 Storage exergy

To compare chemical and mechanical energy storage technologies, a common measure of energy content is required. While for chemical energy storage this is directly provided by GIP volume and heating values, for CAES, the conversion of pressure difference to energy must be accounted for. Therefore, an exergy assessment for hydrogen, methane and CAES technologies must be performed. Exergy is defined as the maximum useful work possible during any process that equilibrates the system with its ambient conditions [Osterle, 1991]. At equilibrium, the exergy is zero. Exergy for stored gases is determined by two terms, where the physical exergy represents the amount of work that can be gained from the difference of temperature and pressure from the ambient environmental values, and the chemical exergy represents the amount of work that can be obtained from the difference between the composition of a component in a system and the composition of the same component in the ambient environment [Szargut, 1989]. For hydrogen and methane storage, both physical and chemical contribute to exergy, while for CAES, only physical exergy contributes, as chemical exergy is zero. Storage gases are pressurised and injected into the subsurface and subsequently withdrawn and de-pressurised again from formation pressure to ambient pressure, so physical exergy for all storage gases is calculated as follows Osterle [1991]:

$$ex_{ph} = m \cdot [\Delta H - T_0 \Delta S] = m \cdot [H(T,p) - H(T_0,p_0) - T_0(S(T,p) - S(T_0,p_0))] \tag{2.6}$$

where ex_{ph} [kJ] is the physical exergy of the gas, m [kg] is the mass of the GIP, H [kJ/kg] is the specific enthalpy, S [kJ/kg · K] is the specific entropy and T_0 [K] and p_0 [Pa] are the ambient temperature and pressure, which in this study are set to 298.15 K and 10^5 Pa, respectively, determining the environmental state and are widely used in the literature [He et al., 2017, Szargut, 1989]. The gas enthalpy and entropy differences are determined using the real gas behaviour by the thermophysical property library CoolProp [Bell et al., 2014].

To determine the contribution from chemical exergy, the chemical composition of the ambient reference air composition was defined according to Szargut [1989]. Tabulated standard chemical exergies for the pure components are used in the present study, where the

chemical exergy is 117.1x10^3 kJ/kg for hydrogen, 51.8x10^3 kJ/kg for methane and zero for compressed air [Szargut, 1989].

The total stored exergy, as the sum of physical and chemical exergy, is independent of the injection and withdrawal operations. To account for dissipative losses during storage operation, exergetic efficiency is used here, defined as the ratio of exergy per kg of stored gas withdrawn from the storage to exergy per kg of injected gas during storage loading. Exergy per kg of injected or withdrawn gas is termed 'specific exergy' in the following. Exergy losses occur due to friction loss, heat loss or internal combustion in the storage plant, but porous media storage also occurs due to different pressures during injection or withdrawal. During injection, pressure higher than the formation pressure is required to store the gas in the formation, while during withdrawal, this pressure must be lower than the formation pressure. This pressure difference, which is basically due to the movement of the storage gas in the porous formation during injection and withdrawal, represents an additional loss in output exergy when gas is stored in a porous formation and therefore must be accounted for in this study. The corresponding formation pressure limits during withdrawal and injection cycles are calculated as outlined in Section 2.2.5.

2.2.5 Storage deliverability

Storage deliverability is estimated on a site-specific base using an analytical approach, accounting for petrophysical properties, initial and boundary conditions, real gas composition and well configuration [Ahmed, 2018]. This approach is also known as the inflow performance relationship and has long been used in the oil and gas industry [Katz et al., 1959]. Assuming a pseudo-steady state flow regime and radial flow in the storage formation, the maximum achievable flow rate Q [m^3/s] to or from a storage well is given by Ahmed [2018] as follows:

$$Q = \frac{2\pi k h T_s \left(\psi(p) - \psi(p_{bhp})\right)}{T p_s [ln\frac{r_e}{r_w} - 0.75 + s]} \tag{2.7}$$

where k [m^2] is the formation permeability, h [m] is the formation net thickness, r_e [m] is the drainage radius, r_w [m] is the wellbore radius, s [-] is the mechanical skin factor, p_{bhp} [Pa] is the bottom hole pressure (BHP) defined as the minimum allowable pressure and $\psi(p)$ [Pa^2/Pa · s] is the real gas pseudo-pressure function [Al-Hussainy et al., 1966], which accounts for the real gas behaviour and stored gas physical properties, such as viscosity and

density. Optimal conditions for storage deliverability are present when the flow rate is not limited by geological factors. Thus, a high hydraulic permeability, high formation thickness, a wide spread between minimum and maximum allowable bottom hole pressures as derived from mechanical considerations, a large borehole diameter and a long screen section all increase the storage deliverability. The maximum achievable rate, as calculated by eq. 2.2, is assumed to be a limiting achievable injection and withdrawal rate during storage operation. In this study, net formation thickness is determined from the geological model individually for each trap, while typical values of r_w = 0.125 m and r_e = 450 m are used assuming a fully perforated vertical storage well, while the skin factor is neglected (see Table 2.3).

Table 2.3: *Main assumption and parameter settings for storage deliverability assessment.*

Parameters	
Flow type	Pseudo steady state
Wellbore perforation	Full formation perforation
Mechanical skin factor	No skin effect near-wellbore
Wellbore radius	0.125 m
Drainage radius	450 m
Maximum allowable BHP	Minimum horizontal stress gradient of 15 MPa/km
Minimum BHP	Half of hydrostatic pressure gradient of 10.5 MPa/km

Achievable flow rates are directly dependant on formation permeability, which varies according to formation type, depth and porosity. In this study, permeability is parameterised by a correlation to formation porosity using a regional permeability prediction model for the Rhaetian and the Quickborn–Volpriehausen [Mathiesen et al., 2011] as well as for the Dogger [Dethlefsen et al., 2014] sandstones of the following form:

$$k = a\phi(z)^b \tag{2.8}$$

which yields k in units of [mD], using dimensionless fitting coefficients for the Rhaetian and the Quickborn–Volpriehausen of a = 19.64x10^5, b = 4.38 [Mathiesen et al., 2011] and a = 2.89x10^4, b = 3.63 for the Dogger [Dethlefsen et al., 2014] and the depth-dependent porosity $\phi(z)$ [-] from equation 2.2. The resulting porosity–permeability correlations as well as the permeability–depth relationships are shown in Fig. 2.4. As can be seen, the Dogger formation has the lowest permeability for a given porosity compared to the Rhaetian or the Quickborn–Volpriehausen formations. The porosity–permeability correlations for the

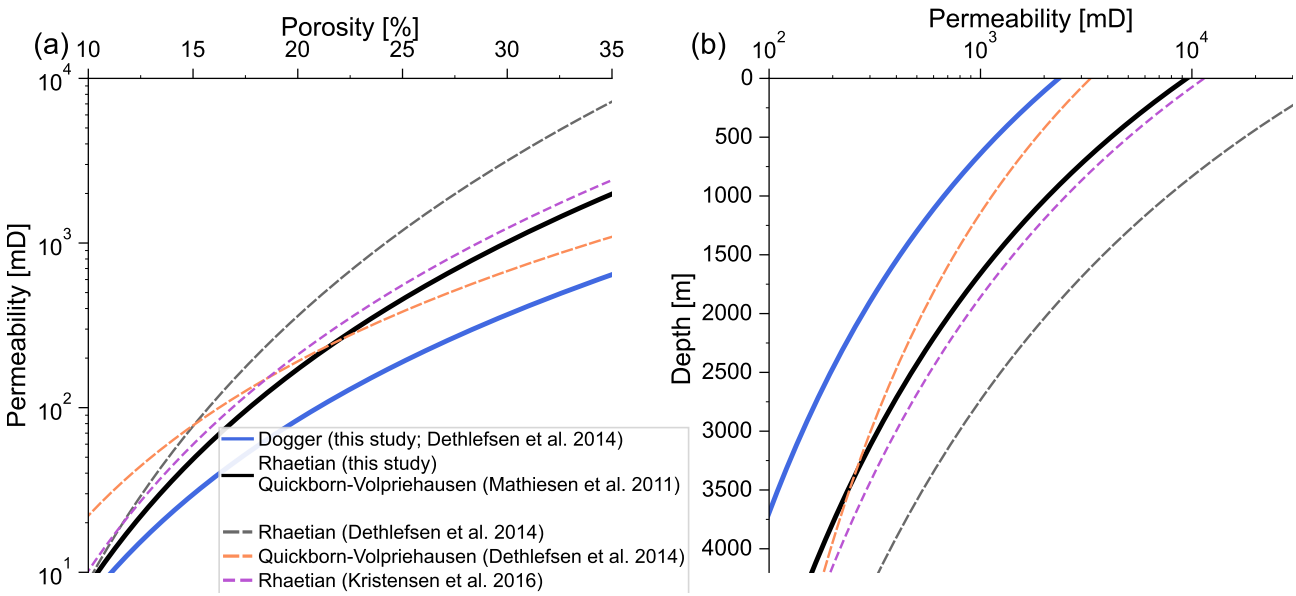

Figure 2.4: (a) Porosity–permeability correlations from the literature for the three storage formations considered; (b) Permeability–depth relationships for storage formations; the solid black line represents the permeability correlation for the Rhaetian and Quickborn–Volpriehausen formations, while the solid blue line shows the correlation used for the Dogger formation.

Rhaetian by Kristensen et al. [2016] (coefficients are recalculated according to dimensionless porosity, see Table 2.4) and for the Quickborn–Volpriehausen by Dethlefsen et al. [2014], also shown in Fig. 2.4, yield similar permeability values for the porosity range used.

Table 2.4: *Parameters for Eq. 2.8.*

Parameters	a	b
Mathiesen et al. [2011]	19.64×10^4	4.38
Kristensen et al. [2016], Rhaetian	23.49×10^4	4.36
Dethlefsen et al. [2014], Dogger	2.89×10^4	3.63
Dethlefsen et al. [2014], Rhaetian	200×10^4	5.36
Dethlefsen et al. [2014], Quickborn–Volpriehausen	2.87×10^4	3.11

While the gas flow rate is directly proportional to the energy withdrawal rate for chemical energy storage (i.e., for hydrogen and methane), a detailed quantification of power output for CAES requires a fully coupled simulation of the coupled geostorage–power plant system [Pfeiffer et al., 2021]. Such investigation lies beyond the scope of this study: such a coupled model would have to be constructed and parameterised for each individual storage site, individually accounting for the geological setting. Additionally, the exergy assessment of the storage sites would depend on the power plant design and distort the comparison. Therefore, only volumetric gas withdrawal rates are calculated and used as a proxy for de-

liverability and energy withdrawal rates.

Storage site operation must account for the minimum and maximum allowable storage formation pressures to prevent harmful mechanical alterations, such as rock consolidation or uplift. These upper and lower allowable pressures are determined using the minimum horizontal stress gradient of 15 MPa/km [Röckel and Lempp, 2003] for sediments above the Zechstein. The upper pressure limit conserves rock integrity by avoiding fracturing, while the lower pressure limit is given by the requirements of the technical facilities at the surface and has to provide for the required well flow rates during withdrawal [Katz et al., 1959]. In this study, the BHP pbhp is set to a limiting lower value of half the initial hydrostatic pressure for each storage site (Table 2.3), assuming that this unloading will not cause formation damage [Bary et al., 2002]. The achievable gas withdrawal flow rate at this minimum BHP is calculated using equation 2.7 and is used to estimate storage deliverability.

2.3 Results

2.3.1 Energy storage capacity

The closure area and pore volume calculations for each storage site are performed using site-specific 3D models. One representative example is shown in Fig. 2.5, depicting neighbouring potential storage sites both in the Quickborn–Volpriehausen and the Rhaetian storage formations. The northern site has two potential storage reservoirs at different depths, both representing structural traps, while for the southern site the Rhaetian storage formation represents combination trap type with an erosional truncation and a faulted anticline trap in the Quickborn–Volpriehausen formation. In Fig. 2.5b, also the crest, spill point and closure of a potential trap are shown. Based on these geometric entities, the results of the capacity assessment of the identified potential storage sites are presented in Fig. 2.6, depicting pore volume and energy storage capacity versus depth for hydrogen and methane for each storage site. The medium porosity–depth correlation is used for parameterisation following equation 2.2 and Table 2.2. The results are summarised in Table 2.5.

As can be seen, only one potential storage site up to a depth of 1000 m in the Dogger formation is identified owing to the limited occurrence of this formation in the study area (comp. Fig. 2.2). For this site, a pore volume of 89x10^6 rm^3 and GIP volumes of about 10x10^9 sm^3 and 8x10^9 sm^3 for methane and hydrogen were estimated, corresponding to energy storage capacities of 95 TWh and 25 TWh, respectively. Within the depth range of 1000 m to

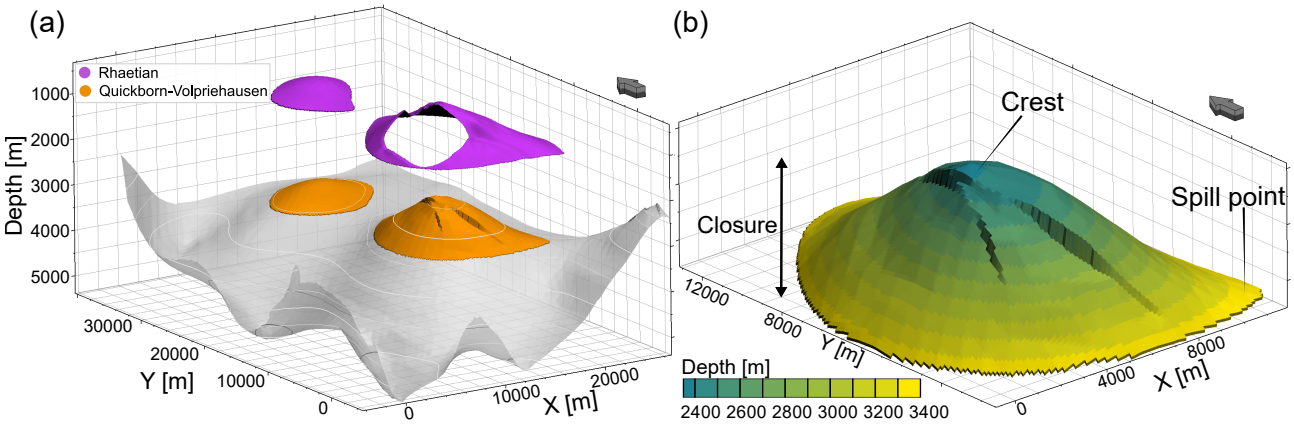

Figure 2.5: a) Exemplary representation of four potential and neighbouring storage sites. The storage closures of the Quickborn–Volpriehausen formation are depicted in orange, the storage closures in the Rhaetian in magenta. The grey surface shows the Quickborn–Volpriehausen storage formation, with while lines indicating equal depths. b) Enlarged view of the southern potential storage site in the Quickborn–Volpriehausen storage formation from a), indicating the main structural features and the formation depth. Vertical exaggeration of both figures is 4, the arrows point North and the axes are absolute values.

2500 m of the Dogger formation, six potential storage sites are identified, with cumulative GIP volumes of $30x10^9$ sm^3 and $26x10^9$ sm^3 and corresponding energy storage capacities of 292 TWh and 77 TWh for methane and hydrogen, respectively. An additional four potential storage sites in the Dogger formation have a trap crest depth larger than 2500 m, with cumulative GIP volumes of $22x10^9$ sm^3 and $20x10^9$ sm^3 for methane and hydrogen, corresponding to energy storage capacities of 217 TWh and 60 TWh, respectively (Fig. 2.6).

Table 2.5: *Assessment results for hydrogen, methane and compressed air for the medium estimate case.*

Storage formation	Depth range [m]	Stored energy [TWh]		Stored exergy [TWh]		
		Hydrogen	Methane	Hydrogen	Methane	CAES
Dogger	<1000	25	95	26	99	1
	1000–2500	77	292	79	307	4
	>2500	60	217	62	229	4
Rhaetian	<1000	368	1361	376	1426	16
	1000–2500	697	2637	719	2769	37
Quickborn–Volpriehausen	<1000	684	2598	702	2725	32
	1000–2500	2762	10530	2859	11068	154
	>2500	1837	6814	1912	7172	111
Total		6510	24544	6735	25795	358

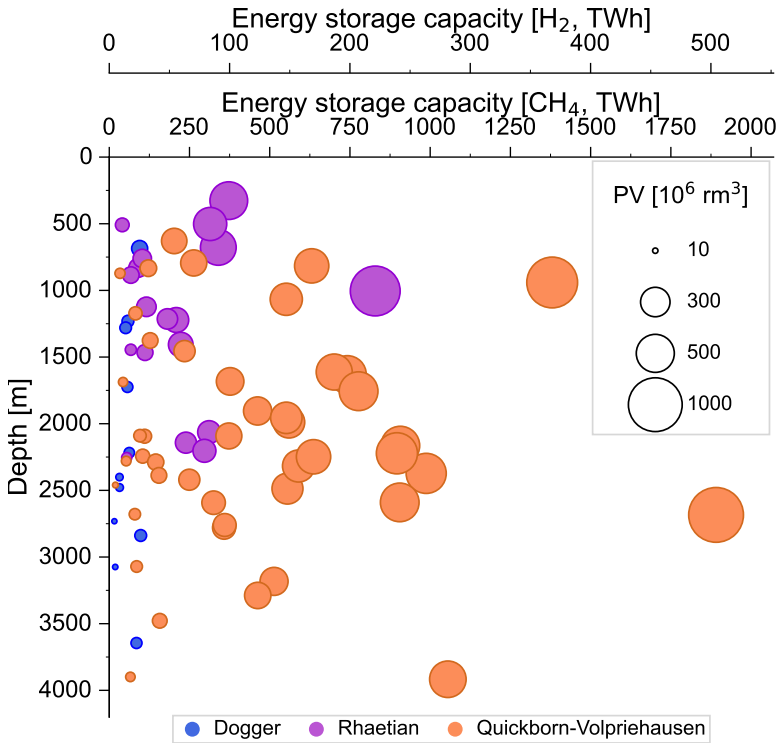

Figure 2.6: Energy storage capacity for methane and hydrogen versus trap crest depth for all identified potential storage sites within the study area. Each circle represents one potential storage site, while the size and colour of each circle indicate the pore volume (PV) and storage formation.

For the Rhaetian formation up to a depth of 1000 m, eight potential storage sites are identified, mainly located at the Eastholstein block (Fig. 2.2a), with cumulative GIP volumes of about 138x10^9 sm^3 and 125x10^9 sm^3, corresponding to energy storage capacities of 1361 TWh and 368 TWh for methane and hydrogen, respectively (Fig. 2.6). Within the depth range of 1000 m to 2500 m, eleven potential storage sites were identified, with total GIP volumes of 268x10^9 sm^3 and 236x10^9 sm^3, corresponding to energy storage capacities of 2637 TWh and 697 TWh for methane and hydrogen, respectively. No potential storage sites below a depth of 2500 m are identified. For the Quickborn–Volpriehausen formation, potential storage sites could be identified at all depth ranges (Fig. 2.6). Five potential storage sites with a depth of up to 1000 m with cumulative GIP volumes of about 264x10^9 sm^3 and 232x10^9 sm^3 corresponding to the energy storage capacities of 2598 TWh and 684 TWh for methane and hydrogen, could be identified. At the depth range of 1000–2500 m, 26 potential storage sites show cumulative GIP volumes of 1070x10^9 sm^3 and 936x10^9 sm^3, corresponding to energy storage capacities of 9198 TWh and 3767 TWh for methane and hydrogen (Fig. 2.6). Below 2500 m, 13 potential storage sites are identified, with cumulative GIP volumes of 692x10^9 sm^3 and 623x10^9 sm^3, corresponding to energy storage capacities of 6814 TWh and 1837 TWh for methane and hydrogen, respectively.

In summary, 44 potential storage sites are identified in the Quickborn–Volpriehausen storage formation, with cumulative storage capacities of 19,942 TWh for methane and 5284

TWh for hydrogen. In the Rhaetian formation, 19 potential storage sites are identified with cumulative energy storage capacities of 3998 TWh and 1065 TWh, while for the 11 sites in the Dogger storage formation, 604 TWh and 161 TWh are estimated for methane and hydrogen energy storage, respectively. The different numbers of identified storage sites for each storage formation are mainly caused by the different spatial occurrence of the formation within the study area (compare 2.2). As the Quickborn–Volpriehausen storage formation is the most abundant, it also hosts the most potential storage sites. Since methane's lower heating value is about three times higher than that of hydrogen and has an approximately 13% higher GIP volume due to its gas compressibility, this results in an energy storage capacity for methane that is four times higher.

Owing to the porosity–depth correlation used, porosity decreases with depth. However, this trend is not clearly discernible in Fig. 2.6, as the geometric size of the geological traps varies strongly between individual sites, overprinting the general porosity decrease with depth. Cumulative energy storage capacity in the depth range of up to 1000 m, 1000–2500 m and below 2500 m are 1077 TWh, 3536 TWh and 1897 TWh for hydrogen energy storage and 4050 TWh, 13459 TWh and 7031 TWh for methane energy storage, respectively. These findings demonstrate that for both storage technologies, large energy storage capacities are available in all depth ranges and formations, with the highest storage capacities present between 1000 m and 2500 m depth in the Quickborn–Volpriehausen storage formation.

2.3.2 Comparision of exergy

For the exergy-based comparison of the storage capacities of the three technologies considered in this study, the exergy of the stored gas is calculated according to the method outlined in Section 2.2.4. The exergy comparison accounts for both physical and chemical exergy and thus considers the GIP volumes of the storage formation, as well as formation pressure and temperature for each individual site. Calculations are based on the medium porosity–depth relationship (Section 2.2.3).

The results for methane, hydrogen and compressed air show that stored exergy for hydrogen and methane is slightly higher than stored energy (Fig. 2.7, Table 2.5). This is because stored exergy considers both the mechanical and chemical contribution, while stored energy is based on the chemical contribution only. For hydrogen and methane, the main contribution to stored energy comes from the chemical part; additional inclusion of the mechanical part changes stored exergy values only slightly. Thus, hydrogen and methane have significantly higher exergy than CAES, for which only mechanical exergy is significant (see Section

2.2.4). For example, at the depth range of up to 1000 m of the Quickborn–Volpriehausen storage formation, stored exergy for methane, hydrogen and compressed air are 2725 TWh, 702 TWh and 32 TWh, respectively. For deeper storage depths of below 2500 m, the corresponding values are 7172 TWh, 1912 TWh and 111 TWh for methane, hydrogen and compressed air, respectively. For any given storage site, the stored exergy of methane is greater than that of hydrogen, which is in turn significantly greater than that of compressed air. Exergy differences between hydrogen and methane primarily result from the different calorific values and thus do not differ greatly according to depth. Contrary to this, the differences between methane or hydrogen and compressed air become smaller with the increasing depth of the storage site as the usable pressure envelope between the upper and lower pressure limits gets larger and thus the mechanical exergy increases.

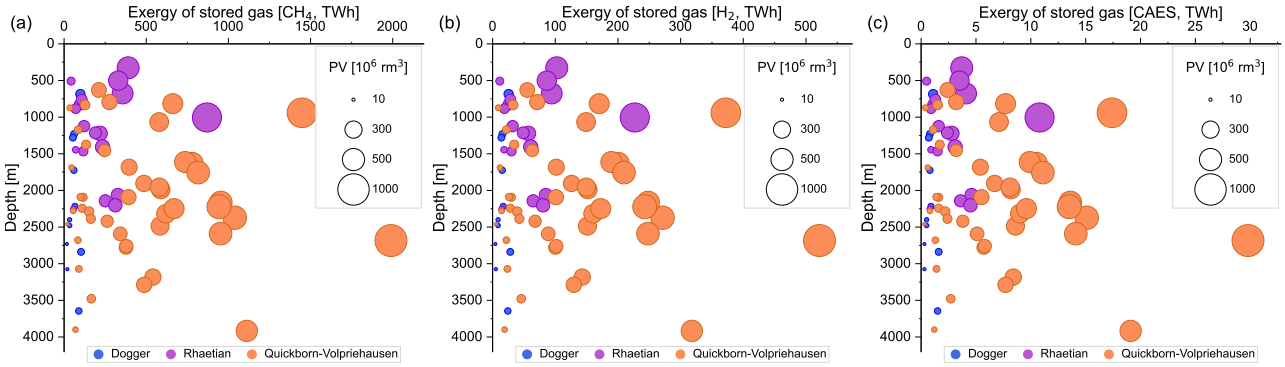

Figure 2.7: Stored exergy versus depth for each potential storage site for (a) methane, (b) hydrogen and (c) compressed air energy storage. Circle size represents storage site pore volume; colour is storage formation used.

For the study area, the total stored exergy summed across all potential storage sites is 25795 TWh, 6735 TWh and 358 TWh for methane, hydrogen and CAES, respectively. However, stored exergy for compressed air is about 30 to 15 times lower than that of hydrogen for the depth ranges of up to 1000 m and below 2500 m, respectively. Separating into onshore and offshore storage potential, it is found that the onshore potential for methane, hydrogen and CAES is 10135 TWh, 2637 TWh and 138 TWh, with the corresponding offshore numbers being 15660 TWh, 4098 TWh and 220 TWh. This demonstrates that the greater proportion, with about 61% of the total storage potential identified in this study, is located offshore.

2.3.3 Storage deliverability performance

Storage deliverability is estimated using the methodology outlined in Section 2.2.5 for estimating achievable well flow rates, using average formation permeability as given by equation 2.8 and the porosity–depth correlation of equation 2.2 (see also Fig. 2.3), and presented in 'per day' units. Gas withdrawal rates vary considerably with the minimum allowable BHP

between individual sites and between storage formations (Fig. 2.8). The calculated theoretical volumetric withdrawal rate is a proxy for the deliverability performance of each storage site, excluding some concomitant effects, such as the turbulence effect, and related skin (see Section 2.2.5) and frictional effects. Maximum theoretical withdrawal rates of about 48x10^6 sm^3/d for methane storage are found for the depth range of up to 1500 m in the Rhaetian storage formation (Fig. 2.8a), decreasing to 19x10^6 sm^3/d in the Quickborn–Volpriehausen storage formation. This depth dependence (compare Fig. 2.4b) is a result of porosity–depth and porosity–permeability relations used in the calculations (see Section 2.2.5), which is also depicted by the circle sizes in Fig. 2.8. Owing to the lower permeability of the Dogger storage formation found for a given porosity, the maximum withdrawal rate for the Dogger formation is only about 10x10^6 sm^3/d and further decreases with depth. Withdrawal rates for individual sites within one storage formation and at the same depth vary owing to different formation thicknesses and average formation permeabilities, which arise when the traps extend across different vertical sections. For the Quickborn–Volpriehausen storage formation, an increase in maximum withdrawal rate with depth is found up to about 2500 m, with values decreasing significantly below this depth. This general behaviour is an effect of the initial pressure, which increases with depth, an increasing pressure difference between the average initial formation pressure and the minimum allowable BHP, allowing for higher withdrawal rates. At the same time, however, permeability decreases with depth, which, in turn, reduces withdrawal rates Table 2.6. The combination of both factors causes the maximum rate found at about 2500 m depth.

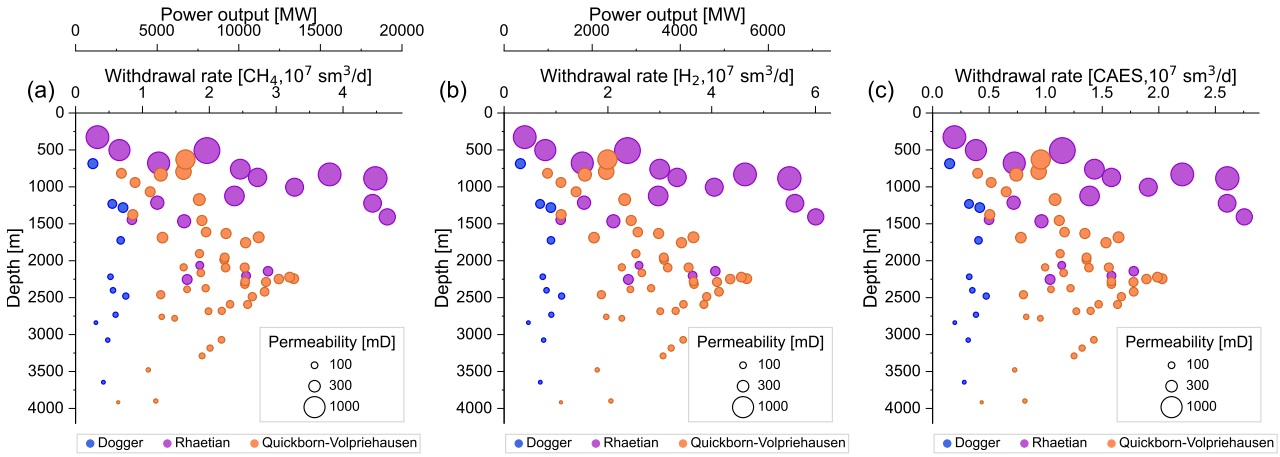

Figure 2.8: Achievable storage gas withdrawal rates at the minimum allowed formation pressure versus depth for (a) methane, (b) hydrogen and (c) compressed air. For hydrogen and methane, energy rates are also given. Circle size represents formation permeability.

Hydrogen should provide the highest achievable withdrawal rates, about 30% higher than those for methane, owing to the lower dynamic viscosity of hydrogen (compare Fig. 2.8). For CAES, achievable rates are lower by a factor of about two compared to hydrogen, owing to the higher dynamic viscosity and lower compressibility of air. However, because hydrogen has a lower calorific value than methane, the power output for methane is higher than

Table 2.6: *Estimated achievable withdrawal rates for hydrogen, methane and compressed air for the medium porosity case.*

Storage formation	Permeability [mD]	Average withdrawal rate [10^6 sm^3/d]			Power output [MW]	
		Hydrogen	Methane	CAES	Hydrogen	Methane
Dogger	<100	8.1	5.3	3.4	953	2186
	100–300	7.1	5.6	3.3	842	2305
Rhaetian	100–300	28.2	20.2	12.4	3328	8286
	>300	31.7	25.7	15.0	3738	10545
Quickborn–Volpriehausen	<100	24.4	15.1	10.0	2875	6182
	100–300	30.5	21.8	13.4	3597	8929
	>300	19.8	16.3	9.4	2336	6663

that for hydrogen by a factor of about three, thus overcompensating for the lower flow rates. Generally, significant variations in the achievable withdrawal rates, resulting from differences in the local setting, such as depth and petrophysical properties, are observed between the individual sites. Nevertheless, all identified storage sites at all depth intervals provide achievable flow rates suitable for gas storage

The results of specific exergy and exergetic efficiency, as defined in Section 2.2.4, for all three storage formations and storage types were evaluated for the withdrawal stage and averaged for the depth ranges, as Table 2.7 illustrates. CAES has a considerably lower specific exergy than hydrogen and methane storage, as only mechanical exergy exists. As noted above, within each storage formation, and with increasing crest depth of the storage site, the specific exergy for compressed air increases (Table 2.7) because of the greater envelope of usable storage pressure during injection and withdrawal. So, for example, at the depth range of up to 1000 m, the calculated specific exergy is about 0.08 kWh/kg and increases to about 0.11 kWh/kg for a storage site at a depth below 2500 m. Owing to the overwhelming share of chemical exergy for hydrogen and methane storage, the calculated specific exergy is considerably higher at 33.95 kWh/kg and 14.56 kWh/kg, respectively. Exergetic efficiency is close to unity for hydrogen and methane, as the chemical component of exergy is entirely reclaimed during withdrawal, while the minor deviation from unity is caused by the pressure difference during injection and withdrawal, which reduces mechanical exergy. For compressed air, the exergetic efficiency increases with depth from 0.77 to 0.82, again a result of the larger usable pressure differences between injection and withdrawal.

2.3.4 Uncertainty quantification

The site-specific properties of geological formations are inherently unknown, so that some uncertainty in the distribution of, for example, the petrophysical properties must always be considered [Durlofsky, 2005]. These originate from missing knowledge on site geometry, trap depth, trap area, spill point location as well as values for porosity and permeability. Because in this study the trap geometry, spill point, depth, thickness and area could be determined on a site-by-site approach using the detailed three-dimensional geological model constructed as described in Section 2.2.1, the petrophysical parameters of porosity and permeability are considered the most uncertain parameters when estimating energy storage capacity. This is in accordance with findings of e.g. [Knopf and May, 2017], who observed the same when estimating the porous media storage potential for CCS. To estimate the effects of a variation of these parameters, two additional scenarios representing an upper and a lower estimate of the storage capacity were investigated. These were generated by varying the porosity–depth function, as discussed in Section 2.2.3 and depicted in Fig. 2.3, by increasing or decreasing the porosity for any given depth by 0.05. This variation in porosity also affects the maximum gas saturation and the formation permeability, which are both parameterised as a function of porosity in this study, thus feeding back into the pore volume and GIP estimates. Owing to the change in permeability, achievable withdrawal rates are also influenced by porosity variation.

The cumulative energy storage potential for upper, medium (i.e., 'most likely') and lower

Table 2.7: *Estimated specific exergy for hydrogen, methane and compressed air during withdrawal stage and average exergetic efficiency at maximum injection and withdrawal. See Section 2.2.4 for the calculation method.*

Storage formation	Depth range [m]	Specific exergy [kWh/kg]			Exergetic efficiency [-]		
		Hydrogen	Methane	CAES	Hydrogen	Methane	CAES
Dogger	<1000	33.69	14.53	0.08	0.99	1.00	0.77
	1000–2500	34.03	14.56	0.10	0.99	1.00	0.81
	>2500	34.24	14.59	0.11	0.99	1.00	0.82
Rhaetian	<1000	33.67	14.52	0.08	0.99	1.00	0.77
	1000–2500	33.97	14.56	0.10	0.99	1.00	0.81
Quickborn–Volpriehausen	<1000	33.74	14.53	0.08	0.99	1.00	0.78
	1000–2500	34.05	14.57	0.10	0.99	1.00	0.81
	>2500	34.23	14.59	0.11	0.99	1.00	0.82

porosity estimates are presented for each storage formation in Fig. 2.9, and detailed numbers are given in Table 2.5. Fig. 2.9 indicates that a porosity variation of ± 0.05 with respect to the medium case causes changes in the estimated energy storage capacity for both hydrogen and methane of about ± 30% for the Dogger, ± 20% for the Rhaetian and ± 30% for the Quickborn–Volpriehausen storage formations, respectively. Changes were greatest for the deeper storage sites, as the relative change in porosity for these sites is also greatest. Consequently, the potential storage sites in the Rhaetian formation exhibit a reduced uncertainty compared to the Quickborn–Volpriehausen or Dogger formations. Cumulative storage capacity estimated from the high porosity case is almost twice that estimated from the low porosity case. As changes in porosity directly affect GIP calculations, the estimated storage capacity variations are identical for both hydrogen and methane. Uncertainty quan-

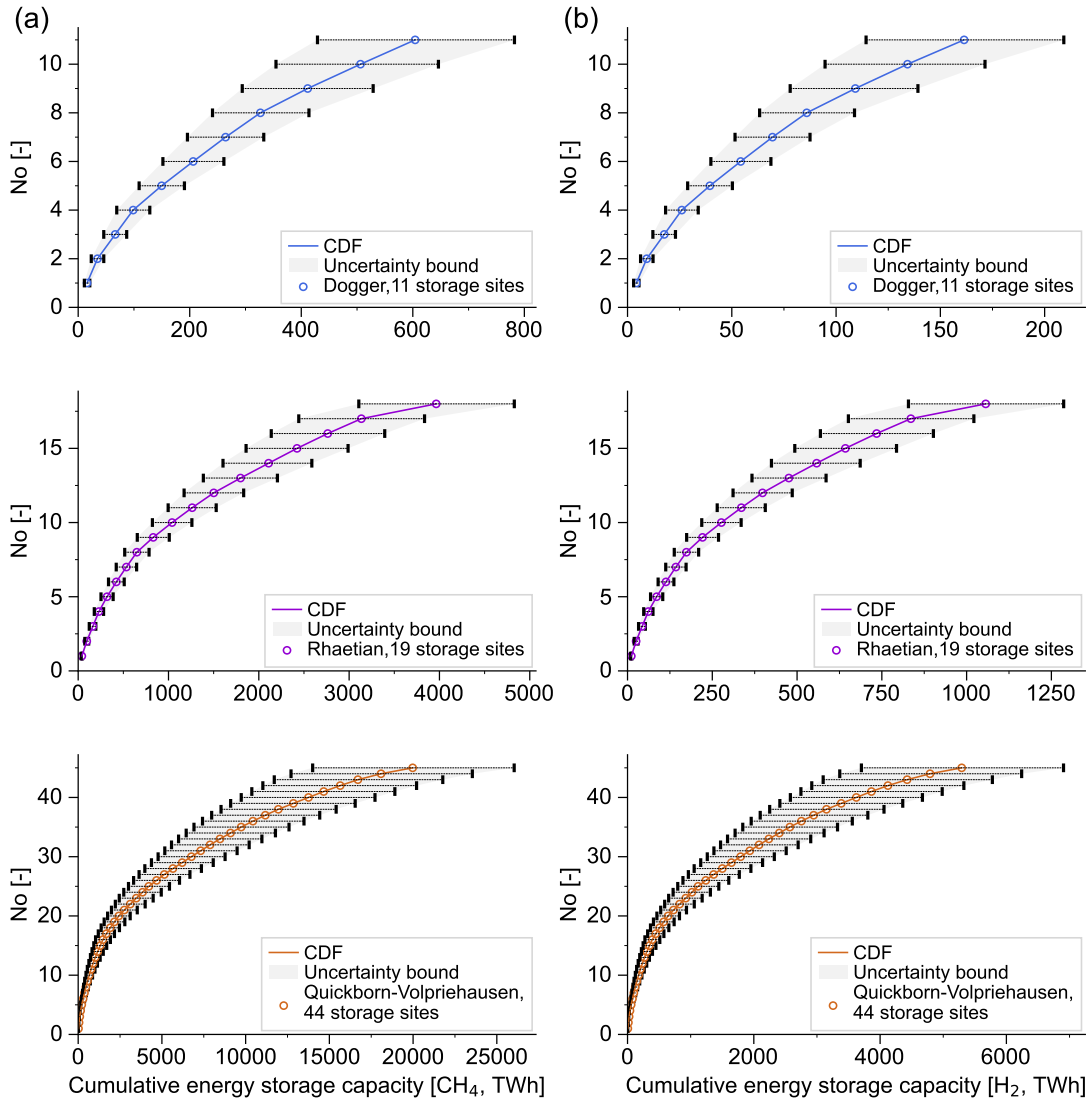

Figure 2.9: Cumulative storage potential for each storage formation for (a) methane and (b) hydrogen. The medium porosity case is depicted with coloured circles, while the high and low estimates are depicted by black vertical markers and the shaded area depicts the uncertainty range. Storage sites are ordered according to their estimated storage capacity from lower to higher capacity; No. is the ordered number of the storage site.

tification for exergy comparison of methane, hydrogen and compressed air exhibits the same trends as for energy (i.e., the higher the porosity, the higher the storage capacity), because the change in porosity affects the GIP for both energy and exergy storage capacity estimations. Formation pressure and temperature are not varied in this analysis; thus, gas enthalpy and entropy remain unchanged. The variation between the upper, medium and lower estimates for stored exergy are ± 30% for the Dogger, ± 20% for the Rhaetian and ± 30% for the Quickborn–Volpriehausen storage formations, respectively (Fig. 2.9).

Because of the porosity–permeability relationships used, changes in porosity affect storage deliverability. Owing to the nonlinear porosity–permeability correlations used (Eq. 2.8), a porosity variation of ± 0.05 leads to higher permeability variation for the low porosities than for the higher porosities range (compare Fig. 2.4). Consequently, the achievable withdrawal rates for all storage gases and storage formations vary by factors of 2.7 for the Dogger, 2.4 for the Rhaetian and 3.3 for the Quickborn–Volpriehausen storage formations from the medium case, depending on the porosity variations (Fig. 2.10). For greater depths, in particular, the achievable withdrawal rates are strongly influenced by uncertainties in the formation porosity, yielding an uncertainty range of achievable rates of about one order of magnitude.

2.4 Discussion

The approach for storage capacity estimation used in this study – screening for individual potential storage sites in specific geological porous formations with suitable petrophysical properties and existing cap rock layers – yields geometrically well-defined potential storage sites with crest depth, formation volume and GIP volumes. This method requires a consistent 3D geological model of potential storage formations, which can only be constructed if adequate subsurface information is available. For the NGB, these data on the deeper subsurface are available from oil and gas exploration, but data may be insufficient or missing in other places, even if formations are present. This would only facilitate a more generic and formation-based approach, as has been applied by Reinhold et al. [2011] for parts of the NGB, which would likely yield a less conservative storage capacity estimate, as has been shown by a method comparison for CO_2 storage [Knopf and May, 2017]. The increased accuracy of the approach adopted in the present study thus requires a pre-existing large dataset on subsurface geological layers.

In addition to the geological model, site-specific petrophysical data would also be required for an accurate estimation of pore space and deliverability. As these data are typically even

scarcer than the basic geological information and are not available for the local potential storage sites of this study, correlation models based on available data considering regional

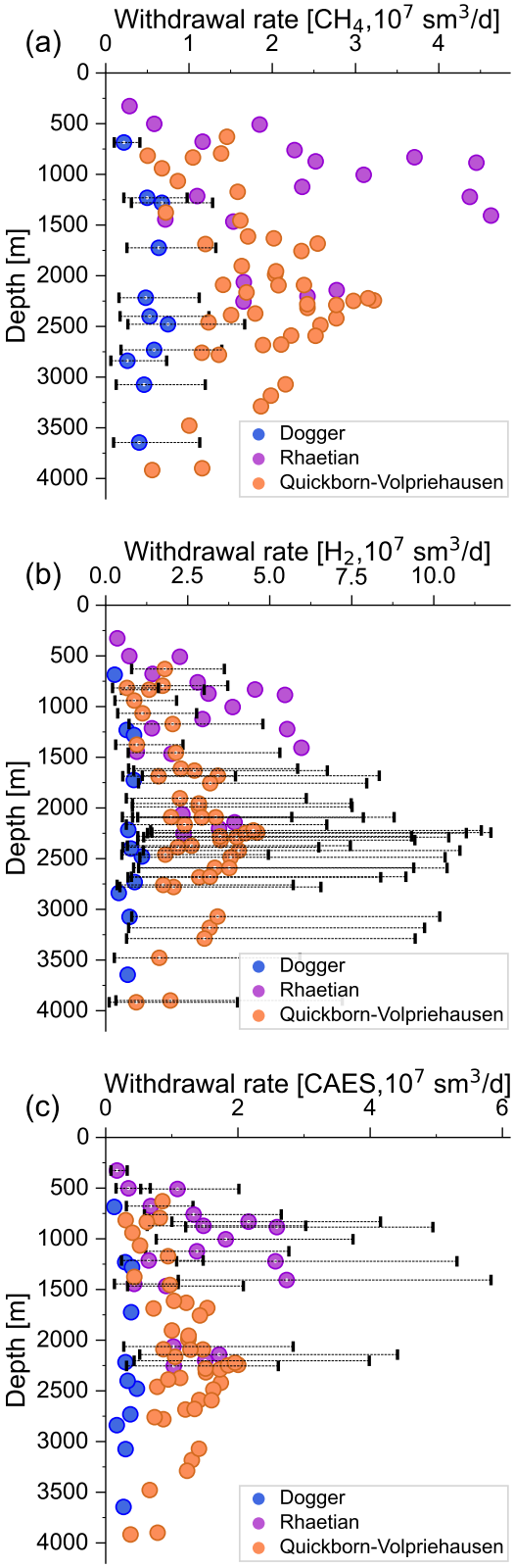

Figure 2.10: Achievable withdrawal rates for high, medium and low porosity cases for (a) methane (b) hydrogen and (c) compressed air energy storage. Variability for the Dogger storage formation is indicated in (a), for the Quickborn–Volpriehausen in (b) and for the Rhaetian in (c).

lithological trends and characteristics for the storage formations must be used. However, while these may capture trends such as the depth dependence of porosity, the significant variabilities in petrophysical parameters known from studies of individual cores or boreholes cannot be directly represented but must be considered in sensitivity and uncertainty studies. While the depth dependence of porosity is explicitly considered in the present study, including an uncertainty margin, some of the data points from earlier studies are still not covered by correlation models (see Fig. 2.3). As data compilations by Dethlefsen et al. [2014] and Kristensen et al. [2016] show, spatial variability may be considerable. To capture these variances, more formation or site-specific data are required for the investigated area of the NGB (i.e., drilling and core measurements).

Potential storage sites can be identified at all depth ranges, with the highest energy storage capacity located in the Quickborn–Volpriehausen formation at the depth range of 1000–2500 m. Since this is the deepest formation considered, storage site development is costly owing to high drilling and completion expenses [Katz et al., 1959], in combination with generally lower formation porosity and permeability, potentially restricting achievable flow rates. As geological and petrophysical data are less frequently available with depth, uncertainty is also higher at higher depths. This is further supported as the effects of variations in the petrophysical properties on storage metrics, such as energy and exergy storage capacity, as well as withdrawal rates and, consequently, charging and discharging power ratings increase with depth. However, already at depths shallower than 1000 m, the potential storage capacity determined from stored exergy is about 1100 TWh for hydrogen, 4250 TWh for methane and 50 TWh for CAES. Compared to an estimated storage demand of about 50 TWh for overwhelmingly renewable energy production, this indicates that each storage technology would be suitable to satisfy such a storage demand and that additional criteria, such as achievable rates, cycle times and energy system service, can be considered when selecting storage technology and site. As the identified energy storage capacity is significantly higher than the predicted demand, shallow potential storage sites are preferable for further investigation.

This study provides a general approach to screen for, assess and quantify the storable energy for a potential storage site in a porous geological formation. This approach was tested and applied to a part of the NGB that was used as the study area, and the quantitative results are thus limited to this region. However, because the NGB is a part of the larger Central European Basin System, which encompasses parts of the United Kingdom, the Netherlands, Germany, Denmark, Poland and offshore parts of Sweden as well as the Baltics [Donadei and Schneider, 2016], the same approach can also be applied to the wider basin. Owing to the regional geological setting of the study area, which is characterised both by salinar

progression to shallow depths and thus strong vertical shifts in the porous formations as well as stratified parts with flat-laying formations [Hese, 2012], the study area is considered representative of the larger basin's geological situation. This was indicated by a large-scale study of potential CO_2 storage sites for the NGB [Reinhold et al., 2011], but suitable porous storage formations in comparable geological basin structures are available throughout much of the world [Vangkilde-Pedersen et al., 2009]. This suggests that the approach adopted in this study can be applied globally and will thus also allow the estimation of geological storage potential on the global scale.

Although energy storage capacities – particularly loading and unloading rates – can be limited by the geological parameters at a specific site, the high number of available potential storage sites as well as their large capacities shows that only a small fraction of the potential sites identified will be required to meet the predicted energy storage demand of about 50 TWh for Germany [Klaus et al., 2010]. These sites can therefore be selected from the optimum settings found, allowing them to optimise deliverability and match the required capacity to the subsurface situation as well as to limit the risks associated with the uncertainty of the geological parameters. This approach thus represents a first site selection step, and only a few of the identified potential storage sites would require further, closer investigation in the subsequent, more extensive site selection steps (i.e., seismic surveys or drillings). The suitability of a potential storage site will not only be determined by geological considerations: proximity to renewable power plants or large energy consumers as well as connectivity to power and gas networks are also selection criteria worth considering [Bauer et al., 2017]. In such a site selection approach, the uncertainty quantification provided in the current study represents a first step towards an economical risk assessment and can be extended to a multidisciplinary risk and uncertainty analysis, which also considers the requirements of the energy sector and the renewable energy regulatory framework [Child et al., 2019].

The capacity estimation performed here does not consider dynamic effects during storage, such as mutual well interference, pressure propagation into surrounding cap rock [Benisch and Bauer, 2013, Birkholzer et al., 2015], gravity override [Juanes et al., 2010] or permeability heterogeneity on the scale of the storage site, leading to a decline in usable pore space and deliverability [Al-Khdheeawi et al., 2017, Pfeiffer and Bauer, 2019]. Additionally, all storage technologies considered require the presence of cushion gas, which may typically account for one-half or even two-thirds of the total storage capacity [Katz et al., 1959]. Generally, consideration of all these effects reduces the estimated capacity. Quantification of these effects, which is important at the stage of storage site dimensioning, requires the use of process-based quantitative multiphase flow models for the individual storage site con-

sidered, as stressed by Bachu [2015], for example, and demonstrated in many site studies. For example, Mitiku and Bauer [2013] found in a site-specific study that only about half of the estimated PV of an anticline could be effectively used for CO_2 storage. For CO_2 storage potential assessments, a so-called storage efficiency factor (e.g., Holloway et al. [1996]) was introduced, which typically includes factors accounted for in this analysis, such as residual water saturation or trap geometry, as well as factors not considered here, such as proximity to sources for the storage gas or the distribution network, technical installations and regulatory limitations. These factors are applicable on the basin scale and not in a site-specific approach, such as that used here. Furthermore, as the technology employed rapidly evolves and depends significantly on local site-specific conditions, such as the connection to the power grid and proximity to sources of renewable energy, a consistent approach to quantifying a technology efficiency factor is not feasible and has thus been excluded from this comparison. Energy storage capacity and stored exergy, together with deliverability, form a basis for storage site identification and characterisation and can thus be used for all future subsurface storage development studies to aid comparisons.

To compare the energy storage capacity of individual potential storage sites consistently for the three storage technologies considered herein, it is necessary to determine the respective exergy that is provided for a consistent comparison and, thus, an assessment of the use options for an individual site. Because this exergy assessment considers pressure and temperature conditions in the storage site as mechanical exergy, in addition to site geometry and petrophysics – which mainly influence chemical exergy – storage exergy for hydrogen and methane is slightly higher than that for stored energy (see Table 2.5). The exergy concept can, in principle, be extended to include power plant design, cycle duration, cushion gas and individual operating conditions (see, e.g., He et al. [2017]). This may offer a valuable contribution when planning an individual storage operation but requires local and site-specific data and assumptions, given that the power plant and storage design would vary for different depths (e.g., Pfeiffer et al. [2021]). Thus, it is not suitable for a regional screening, as in this study. This is particularly true for CAES, as only mechanical exergy contributes to stored exergy, which shows a nonlinear dependence on formation and limits bottom hole pressures.

Storage deliverability has been shown to rely heavily on gas properties in combination with formation permeability and achievable maximum pressure difference. The highest withdrawal rates were found for the shallower Rhaetian formation, owing to the high average formation permeability. Withdrawal rates vary significantly for all storage formations, depending on the specific depth, while uncertainty increases for deeper storage sites. However, even for the lower estimate, the achievable withdrawal rates for each identified site in this

study were sufficiently high to support gas storage. While a significant uncertainty in storage capacity is not a decisive factor, given that the total estimated storage capacity is much larger than predicted demand, reduced deliverability would diminish storage performance and energy rates for each site. However, increasing the number of storage wells can mitigate deficits in storage performance if the achievable withdrawal rates are indeed a limiting factor, albeit at additional investment and operational costs. This again highlights the need for site-specific formation data for the design of individual storage plants.

The detailed characterisation of storage capacity and deliverability is an important step in designing future geological energy storage sites, not only by providing the available capacity, but also by allowing the ranking of available sites according to energy storage capacity, achievable rates and background formation pressure. This facilitates an optimised application of storage technology for an individual site, i.e. by using the sites with the highest deliverability for CAES, as the deliverability is more important for physical gas storage than for chemical gas storage, while for seasonal storage using e.g., synthetic methane the capacity may be more important. Furthermore, provision of the required well number allows to estimate the installation costs for the subsurface part of such a storage site. A reliable, site-specific estimation of rates and capacities is further required when integrating the storage sites into existing energy networks for power or gas using a model-based approach (i.e., to determine storage cycles or cycle times).

Typical CAES employment with frequent and short-term cycles amplifies the dependency between favourable reservoir conditions and high flow rate deliverability. Appropriate storage sites with high formation permeabilities and suitable pressure ranges for CAES are mainly present in the Rhaetian formation as well as in the shallow parts of the Quickborn–Volpriehausen formation and are thus situated in the onshore region of the study area. For hydrogen and methane storage, high flow rates are also advantageous but less important owing to the typically lower cycle frequency and the higher chemical exergy of the energy carriers, providing greater technical and economic freedom during site selection. Thus, potential storage sites can be found in the shallower parts of all storage formations considered herein.

Overall, the estimated subsurface potential is sufficiently large to cover national-scale storage demand for the three storage types considered here; however, depending on energy system planning strategy from policy makers and intensity of energy system decarbonisation, the number of storage sites, locations and storage types can vary. For example, the exclusive use of CAES in the United Kingdom offshore means that offsets between energy demand and availability can be achieved on a national scale [Mouli-Castillo et al., 2019].

For the Nordic countries with expected grid capacity expansion to the continental European countries [Research and IEA, 2016], maintenance of a distributed energy system and of co-ordinated subsurface storage utilisation is more effective. In Germany, with a rapid growth of renewable installed capacity [BMWi, 2018], particularly offshore wind capacity (i.e., 17% growth in 2019 [UBA, 2020]), consideration of small-scale CAES close to offshore wind farms may be plausible. At the same time, additional storage sites for chemical energy carriers might be required and integrated into an existing gas infrastructure to dampen seasonal fluctuations in the energy sector.

Because the geological situations present in the study area are representative for many geological basins both in the European context [Vangkilde-Pedersen et al., 2009] and worldwide [Bradshaw and Dance, 2005], the methods and approaches presented here can be applied to various other porous media storage formations in sedimentary basins and the results of this study can thus contribute to an improved estimation and assessment of global geological energy storage capacity. Even assuming less favourable geological conditions in other geological basins and regional settings, the considerable potential capacities identified indicate that geological storage capacity by one or several of the storage technologies considered here will be sufficient to dampen fluctuations from renewable energy production in most parts of the world in which porous formations may be found. These subsurface energy storage technologies thus present one possible pathway to meet the large-scale energy storage demand arising from the transition to a renewable energy supply in many parts of the world, which is the scale required for the energy transition to sufficiently mitigate the adverse climate effects associated with fossil fuel emissions.

2.5 Conclusion to this chapter

Increasing the share of renewable energy sources will lead to fluctuations in energy production on daily to seasonal time scales, for which subsurface energy storage offers a promising solution. Porous media storage sites are suitable for storing synthetic hydrogen or methane as well as compressed air and are available worldwide, owing to the universal occurrence of the required geological formations. In this study, a 3D spatial screening approach was employed to identify potential storage sites within the NGB, and energy storage capacity, energy rates and stored exergy were quantified for hydrogen, methane and CAES on the basis of individual potential storage sites. These investigations have yielded the following conclusions:

- The site-based approach applied in this study, which accounts for geological setting, trap type, depth and site-specific gas properties, allows for a quantification of stored energy and exergy for individual sites, individual storage formations, or specific depth ranges. It is, thus, a versatile approach to site screening and planning of storage sites with respect to subsurface and energy system requirements and conditions.

- Potential storage sites are found within each main porous formation present and between about 400 m and 4000 m depth. Energy storage capacities for individual sites range from TWh to hundreds of TWh. The potential total energy storage capacity identified for the study area is several orders of magnitude larger than the predicted demand. Therefore, only the most suitable of the 74 potential storage sites identified should be considered for a more detailed characterisation.

- Determination of stored exergy for an individual site allows for a systematic and consistent comparison of the retrievable energy using hydrogen, methane or CAES. Stored exergy is significantly higher for hydrogen and methane than for CAES owing to the high share of chemical versus mechanical exergy. Additionally, exergetic efficiency assessment indicates that anticipated mechanical exergy losses are significant for CAES but negligible for hydrogen or methane storage owing to the excessively high proportion of chemical exergy. Thus, the sites with the highest permeability should be prioritised for CAES.

- Deliverability rates can be estimated for individual sites, providing maximum achievable injection or withdrawal rates during cyclic energy storage. While these can be used to directly assess achievable energy storage rates for hydrogen or methane storage, determination of achievable power output for CAES requires a coupled approach that also explicitly considers the power plant.

- Restricted knowledge and uncertainty around geological parameters leads to considerable uncertainty of estimated storage capacities and storage rates. This study has shown that even considering this uncertainty, storage capacities will be sufficiently large to compensate for fluctuating renewable energy production, while the uncertainty of achievable storage rates may considerably limit a potential storage site's suitability. As geological information becomes scarcer and uncertainty increases with depth, shallow storage sites offer the lowest uncertainty and should thus be prioritised, in line with reduced exploration and drilling costs.

- As the study area is considered representative of the setting encountered in a typical

sedimentary basin structure, the approach detailed herein can be applied on a global scale, as suitable geological conditions are present in many places around the globe. These findings thus indicate that one or a combination of the storage technologies considered here may significantly contribute to meeting the energy storage demand required to dampen fluctuations from renewable energy production and thus stabilise and secure the energy supply.

3 Integration of geological energy storage into energy systems

Part of the content in the following chapter has appeared in the Energy Conversion and Management:

Firdovsi Gasanzade, Francesco Witte, Ilja Tuschy and Sebastian Bauer (2023) Integration of geological compressed air energy storage into future energy supply systems dominated by renewable power sources. doi:10.1016/j.enconman.2022.116643

3.1 Introduction

The transition from a carbon-rich energy system to a system dominated by renewable energy sources is a prerequisite for reducing CO_2 emissions [IEA, 2021] and stabilising the world's climate [Clarke et al., 2022]. However, power generation from renewable sources like wind or solar power is characterised by strong fluctuations [Gerhardt et al., 2015]. To stabilise the power grid in times of high demand but low renewable power production, energy storage on various scales is required. For example, assuming shares of renewable energy sources (RES) of 80% or higher, an energy storage capacity of up to 83 TWh with instantaneous power loads of 8 GW–140 GW may be required [Cebulla et al., 2018].

The geological subsurface, particularly porous formations, can offer grid-scale energy storage options [Bauer et al., 2012, Kabuth et al., 2017], either by storing a chemical energy carrier, such as hydrogen or methane [Pfeiffer and Bauer, 2019, Sainz-Garcia et al., 2017, Tarkowski et al., 2021] or by storing mechanical energy as compressed air [Gabrielli et al., 2020, Hartmann et al., 2012, Mouli-Castillo et al., 2019, Sopher et al., 2019] or as sensible heat (e.g., Bloemendal et al. [2018], Fleuchaus et al. [2018]). Geological storage of gaseous methane, which is the major constituent of natural gas, has been well investigated and implemented for decades to stabilise seasonal mismatches between production and demand. Storing mechanical energy in the subsurface using pressurised air for strongly fluctuating conditions represents a novel application.

PM-CAES facilities have historically been used for peak-shaving and load-levelling applications, with a smaller adverse impact on the environment than a conventional peak power plant, where a significant fraction of the electrical output is used to run a compressor sta-

tion [Budt et al., 2016, Glendenning, 1981]. No commercial CAES facility currently operates in porous media, as the two existing sites, with a total installed power capacity of 0.6 GW [Succar and Williams, 2008, Tuschy et al., 2002], operate in salt caverns and are used to balance power output from connected power plants. The most recent commercialised facility at the Goderich site in Canada has been designed as a merchant plant to compete in the electricity markets; however, it has a storage capacity of 15 MWh and an installed discharge power capacity of 1.75 MW only [King et al., 2021]. Porous media CAES (PM-CAES) has been identified as offering significant advantages in terms of total energy (exergy) capacity per site, cost per unit of power (1050 $/kW–2544 $/kW) and per unit of storage capacity (94 $/kWh–229 $/kWh) [Mongird et al., 2019]. Moreover, the worldwide occurrence of porous formation deposits is considerably wider than that of salt deposits, allowing this technology to be elevated to the global scale. Recent studies have demonstrated that PM-CAES may provide storage capacities of tens of TWh in sedimentary basins [Gasanzade et al., 2021, Mouli-Castillo et al., 2019], thus potentially offering grid-scale storage on the national scale [Adamek et al., 2012, Cebulla et al., 2018]. While for chemical energy carriers like hydrogen and methane as well as for carbon dioxide the storage capacity is largely determined by geological factors like available pore space and trap size [Bachu et al., 2007, Birkholzer et al., 2015, Mitiku and Bauer, 2013, Ringrose and Meckel, 2019], PM-CAES additionally strongly depends on the technical configuration of the surface power plant and the short term temporal behaviour of the power system. A coupled assessment with a dedicated software tool is thus required [Budt et al., 2016] when estimating PM-CAES performance. While Pfeiffer et al. [2021] have recently developed a coupled model approach, they presented only synthetic application scenarios, employing simplified load curves to validate the simulator's capabilities. However, as their study and other applications of PM-CAES have demonstrated [He et al., 2021], storage capacity and power delivery are heavily influenced by the short-term fluctuations encountered in the power systems.

All available PM-CAES studies hitherto have been based on a reference power plant originally designed for salt caverns [Gabrielli et al., 2020, Guo et al., 2016, Mouli-Castillo et al., 2019, Sopher et al., 2019, Wang and Bauer, 2017]. However, in view of fundamentally different pressure propagation within a porous medium compared to a void space (salt cavern), power plants have to be specifically designed for PM-CAES applications [Pfeiffer et al., 2021]. Also, both adiabatic as well as diabatic power plant topologies are theoretically possible, which result in unique pressure effects in the porous formation and thus directly influence storage capacity and efficiency. To date, no investigation of real-world geological storage sites and fluctuating load profiles, as found in realistic future energy systems dominated by RES, has been reported.

Therefore, in this manuscript, we provide an integrated assessment of PM-CAES, considering the specifics of the geological storage site, the power plant as well as the energy system. For this, we consider a set of future energy system scenarios, each representing a significant contribution of RES, and the effects of three surface power plant setups as technology variations. For the geological storage site, an existing storage formation with a suitable trap structure is used, and well design variations are evaluated in terms of their effects on achievable storage capacity and loading rates. This study is thus the first to offer a complete framework for assessing achievable storage rates and capacities for PM-CAES based on detailed future energy systems forecasts, the geological and geotechnical settings and engineering components of the compressed air energy power plant.

3.2 Methodology

To perform an integrated assessment of PM-CAES, an energy system model is coupled with a surface power plant model and a subsurface geological storage model. Figure 3.1 illustrates the concept applied herein in detail. The energy system model represents the time-dependent power sources and power demand for a single year and triggers the loading or unloading of the PM-CAES system via a dispatch signal. Power plant and geological storage operations are each represented by dedicated models, coupled via energy and mass balances, proving the respective power rates to the energy system model. Pfeiffer et al. [2021] describe the coupled three-step model in greater detail (Fig. 3.1a) as well as implemented and tested an iterative coupling of the power plant and the geostorage model using a model interface. Figure 3.1 shows the target air mass flow rate designed at the power plant level to generate a target power required by the energy system model, which also provides the times for surplus power used to compress and store the air in the subsurface. Actual air mass flow rates and achievable power for the given actual storage pressure are calculated by the coupled model based on the prior history of the coupled system. Power mismatches occur when the target mass flow rate cannot be met by the power plant (see Fig. 3.1a, interface). The present study represents the first attempt to assess PM-CAES operation in an energy system dominated by RES for a set of future energy system pathways. The energy system pathways represent each one future year of the energy transition with increasing RES shares of 76% in 2030, 86% in 2040 and 100% in 2050 in the energy system. This is achieved by assuming total installed solar power (218 GW) and on- and offshore wind power (183.5 GW) production capacities in 2050. The detailed energy system development pathways with all assumptions regarding energy supply and demand and the respective technical installations have been extensively documented by Hilpert et al. [2020]. Quantitative predictions were performed using the Open Energy Modelling Framework [Hilpert et al., 2018] within the ANGUS re-

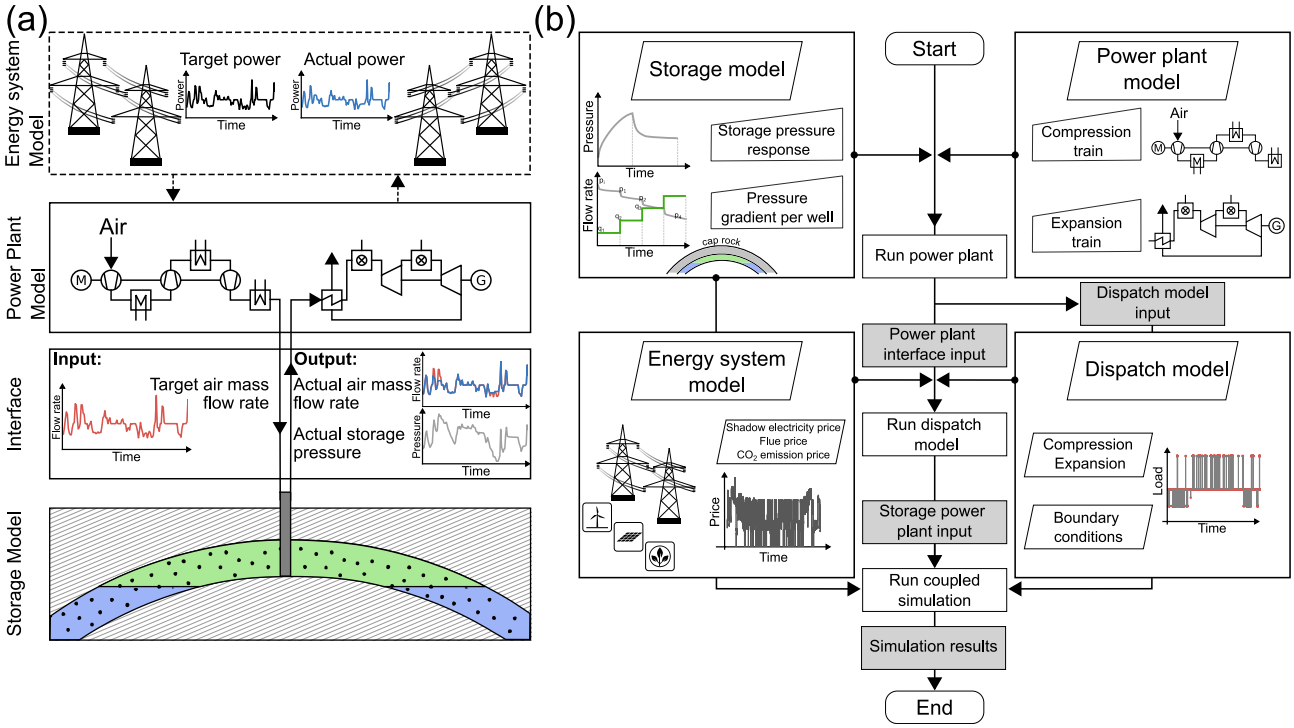

Figure 3.1: (a) Schematic of the coupled simulator for a porous medium CAES (after [Pfeiffer et al., 2021]). (b) The detailed integrated PM-CAES assessment workflow showing the coupling of the power plant–geostorage model with the energy system model using dispatch optimisation.

search project [Kabuth et al., 2017]. The energy system scenarios represent possible future energy markets in Germany for RES to varying degrees in terms of shadow electricity price, CO_2 emission price and fuel price, providing an economic signal for the loading or unloading of the PM-CAES (i.e., the dispatch signal) (Table 3.1). To obtain the power dispatch of the PM-CAES from the national-scale energy system, an optimisation scheme is integrated into the energy system model using predefined power plant and geostorage characteristics

Table 3.1: *Energy system scenarios, power plant type and share of renewable energy sources as well as the main input parameters for scenario assessment.*

Scenario year	Power plant type	Renewable share [%]	Average shadow electricity price [EUR/MWh]	CO_2 emission price [EUR/t]	Fuel price [EUR/MWh]	Target annual energy [GWh]	
						Charge	Discharge
2030	D-CAES	76.3	52.6	29.4	26.40	148.1	259.0
2040		85.9	83.7	126.0	30.24	304.9	531.2
2050		100.0	88.3	150.0	43.72	230.5	400.9
2030	2-AA-CAES	76.3	52.6	-	-	150.0	89.1
2030	3-AA-CAES	76.3	52.6	-	-	150.6	90.2

derived during the power plant design (Fig. 3.1b). The objective is to minimise the total operational costs from an operator's perspective for a specific power plant and geostorage configuration, using mixed-integer linear programming [Gurobi Optimization, 2021] and a perfect foresight approach wherein shadow electricity prices and CO_2 emission and fuel prices (for a diabatic setup) serve as the economic boundary conditions for generating a time-dependent representation of the electricity load. In the following sections, the power plant and the geostorage model setups are introduced and based on this a more detailed description of the assessment workflow applied in this study is provided in Section 3.2.4.

3.2.1 Surface power plant facility

Two commercial CAES power plant facilities—in Huntorf (Germany) and McIntosh (USA) — each represent a diabatic power plant design combined with cavern storage, with reported cycle efficiencies of 42% and 54% [Succar and Williams, 2008, Tuschy et al., 2002], respectively. The diabatic design requires an external heat supply during expansion, i.e., when discharging the storage. In this study a diabatic and two adiabatic power plant topologies are used. The diabatic topology (D-CAES) uses a three-stage compression and two-stage expansion with a heat recuperator to preheat the air from the storage. In the adiabatic concepts an internal thermal energy storage unit is used to store the heat released during compression (charging), thus no external heat supply is required during discharging (expansion). One adiabatic set-up, from herein referred to 2-AA-CAES, uses a two-stage compression drivetrain and a two-stage expansion turbine, the other set-up, termed 3-AA-CAES, uses a three-stage compression drivetrain and a three-stage expansion section. All power plant facilities are specifically designed to accommodate a porous media storage site—that is, to account for storage depth, well length, temperature and the alternating reservoir pressures during injection and withdrawal. Table 3.2 presents the power plant configurations used, with a maximum installed power generation capacity of 115 MW. This value is design-specific and will vary for other sites and PM-CAES applications (see also Section 3.2.4). The compression pressure ratios of 10 and 5 have been chosen so that homogenous temperature levels for all stages are achieved. The pressure ratios at the design point are thus given by the nominal pressure ratio of 115 bar to the power of $\frac{1}{2}$ and $\frac{1}{3}$ for the two and three stage compression setup, respectively.

The power plant configuration and the required components of both an adiabatic and diabatic setup were implemented using the open-source simulator TESPy [Witte and Tuschy, 2020]. The power plant model uses the Newton-Raphson method to solve a set of non-linear equations, which are based on the properties and physical operations of the individual com-

ponents and consider the conservation of mass and energy. For the configurations used in this paper, the equations (3.1) to (3.5) show the most important relationships: Equation (3.1) is the general energy balance for open systems with a single mass flow m. In case of adiabatic components (compressor, turbine), the heat transfer $\dot{Q}$ is equal to zero, in case of heat exchangers the transfer of work $\dot{W}$ is equal to zero. For the combustion chamber, the reaction enthalpy as well as the different definitions of the zero point of enthalpy h for the fluids have to be considered, since the fluid composition changes (equation 3.1), with LHV_{fuel} the lower heating value of the added fuel and flue designating the burnt gas mixture. The isentropic efficiency $\eta_{s,cmp}$ of compressors (equation 3.3) and turbines $\eta_{s,exp}$ (equation 3.4) is defined reciprocally and relates the enthalpy difference to the enthalpy difference in an isentropic process. The pressure drop along the well with a compressed air velocity v is determined using the Darcy-Weisbach equation (equation 3.5), which takes into account a dimensionless friction factor f_D, the well diameter D, Reynolds number Re and the roughness k_s (for values see Table 3.2). A detailed overview of the individual power plant components and the applied equations is given in the TESPy online documentation [Witte and Tuschy, 2020]. Operation fields of individual units were pre-defined through systematic calculation of relevant operating points for all power plant components during charging and discharging at various loads. The reference temperature and pressure are set to 273.15 K and 1.013 bar, respectively.

$$0 = \dot{m} \cdot (h_{out} - h_{in}) - \dot{W} - \dot{Q} \tag{3.1}$$

$$\begin{aligned} 0 = \dot{m_{flue}} \cdot (h_{flue} - h_{flue,ref}) - [\dot{m_{air}} \cdot (h_{air} - h_{air,ref}) + \\ \dot{m_{fuel}} \cdot (h_{fuel} - h_{fuel,ref}) + \dot{m} \cdot LHV_{fuel}] \end{aligned} \tag{3.2}$$

$$0 = \eta_{s,cmp} \cdot (h_{out} - h_{in}) - (h_{out,s} - h_{in}) \tag{3.3}$$

$$0 = \eta_{s,exp} \cdot (h_{out,s} - h_{in}) - (h_{out} - h_{in}) \tag{3.4}$$

$$0 = \frac{\rho v^2 f_D(Re, D, k_s)}{2D} + (p_{out} - p_{in}) \tag{3.5}$$

3.2.2 Geological setting of storage site

Porous formations that are suitable as storage sites for PM-CAES are characterised by a reservoir volume that is sufficiently high to accommodate the amount of compressed air required

Table 3.2: *Power plant and geostorage parameters for the scenario simulations.*

Component	Parameter	Value
Compressors	nominal power	230 MW
	isentropic efficiency, $\eta_{s,cmp}$	0.92
	isentropic efficiency control stage, $\eta_{s,cmp,cs}$	0.85
	pressure ratio stages 1 and 2 (diabatic, three-stage adiabatic)	5
	pressure ratio at stage 1 (two-stage adiabatic)	10
Turbines	nominal power	115 MW
	isentropic efficiency, $\eta_{s,exp}$	0.90
	isentropic efficiency control stage, $\eta_{s,exp,cs}$	0.85
Coolers	temperature after cooling (diabatic)	298.15 K
	temperature after cooling (adiabatic)	338.15 K
Generator & Motor	efficiency, $\eta_{el,mech}$	0.97
Combustion	fuel type (diabatic)	CH_4
	turbine inlet temperature	1473.15 K
	outlet temperature (diabatic)	423.15 K
	pressure loss	3%
Heat exchangers	temperature after reheating (adiabatic)	573.15 K
	pressure loss	2%
Storage	nominal pressure compression	115 bar
	nominal pressure expansion	100 bar
	vertical well length, L	1055 m
	vertical well number	9 / 3
	pipe roughness, k_s	0.04 mm
	well diameter, D	0.25 m
	horizontal well number	2 / 2
	horizontal section length,L_h	450 m / 850 m
	total completion length,L_c	150 m / 500 m

for both cyclic storage and cushion gas, a gas-tight cap rock above to stop the buoyant rise of the gas, and a high intrinsic hydraulic permeability to allow for the movement of the injected compressed air and thus the required high loading and unloading mass flow rates. These criteria resemble those typically applied for gas storage of methane, hydrogen or carbon dioxide (e.g., Bennion et al. [2000]). Incorporation of this storage option into the energy system does not pose new regulatory challenges, as the subsurface storage of gas, as e.g., for natural gas, has been used for decades, so that adequate and tested regulations are in place. However, a high intrinsic permeability is imperative for PM-CAES, as the energy is stored as pressure and low intrinsic permeabilities increase the pressure losses during storage operation. This resulted in the abandonment of an investigated PM-CAES site in Iowa, as the achievable power output was not considered economically attractive at that time [Holst et al., 2012]. The potential storage site used in this study was selected from Gasanzade et al. [2021] site-screening study, which explicitly accounted for depth-dependent hydraulic permeability and porosity. The site represents a 'sweet spot' for PM-CAES in view of both its high potential storage capacity and high achievable loading and unloading mass flow rates.

The storage trap is formed by an anticline structure on the Eastholstein block (see Fig. 3.2) in the Rhaetian (Upper Keuper) sandstone formation, which facilitates porous storage formation. The trap has a crest depth of around 1000 m and a net usable thickness of 20 m, while marlstone and clay-rich rocks with more than 50 m thickness from the Lias formation (Lower Jurassic) provide the required cap rock [Hese et al., 2017]. The exergetic assessment of this storage site performed by Gasanzade et al. [2021] yielded an upper estimate of 3.67 TWh and a total air-in-place mass of around 34 million tonnes of compressed air. Preliminary design estimates and simulations revealed that only around 17% of this potential storage capacity was required for the energy system pathways investigated here. Table 3.3 details the main parameters characterising the geological storage site.

3.2.3 Geostorage model

A 3D geological model of the storage site was constructed and parametrised according to the regional geological setting (Fig. 3.2b). The numerical model domain for the scenario simulations has a horizontal extension of 12.5 km × 15.5 km. Immiscible two-phase flow of water and gas is assumed. Fluid properties are derived from the CoolProp library [Bell et al., 2014]. Brooks-Corey formulations are used for phase permeabilities and capillary pressure [Brooks and Corey, 1964]. All numerical simulations are performed using the proprietary simulator ECLIPSE [Schlumberger Ltd., 2017]. The ECLIPSE simulator has been developed for the oil and gas industry and been validated and applied in numerous test and

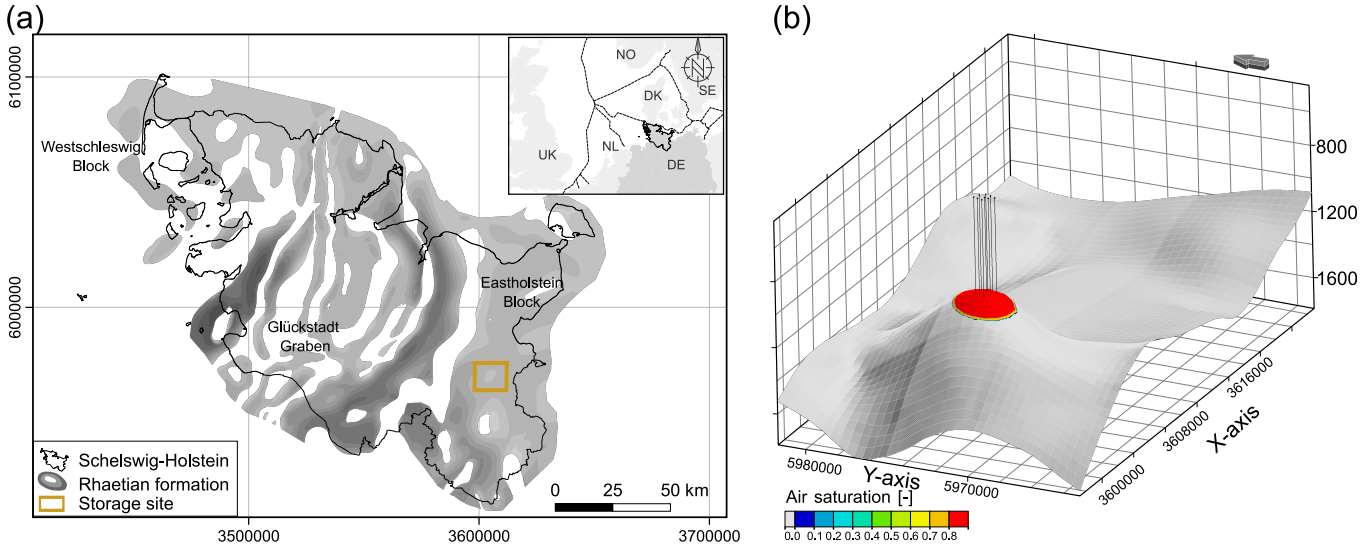

Figure 3.2: (a) Geological setting of the study area in the North German Basin with the potential storage site. (b) Perspective view from the southwest on the anticline storage site; the grey colour marks the porous storage formation; the red colour indicates the distribution of the compressed air, the black lines indicate the nine vertical boreholes with an average distance of 400 m.

application cases for subsurface gas storage. An initial air mass of 5.56 Mt is provided by setting the air-water contact at 1100 m depth, followed by a 10-year spin-up simulation using a constant rate condition to obtain realistic initial conditions for pressure and gas phase distribution. The spin-up simulation consists of 100 d continuous air withdrawal and injection phases, with a mass flow rate of 125 kg/s and intermediate shut-in phases of 100 d and 65 d, respectively. This yielded an initial storage pressure of 112 bar at the storage crest point, while the injected air gas phase shows a lateral extension of 4.5 km by 3.5 km. The hydraulic boundary conditions explicitly account for the large-scale geological setting and the lateral extension of the storage formation in order to obtain precise pressure levels during the operation phase. This is technically achieved by applying a pore volume multiplier at and adapting the permeability of the boundary elements.

The cap rock above the storage formation is assumed to be impermeable. All petrophysical properties within the storage formation are assumed to be homogeneous and isotropic (Table 3.3). Nine vertical storage wells with a distance of at least 400 m, each with a full completion section (see main well settings in Table 3.2) within the storage formation, were used to inject and withdraw the compressed air. The well number was estimated following the procedure described in Gasanzade et al. [2021]. Avoiding formation damage by applying a pressure higher than the fracturing pressure of the formation is a major concern in subsurface storage operations. In this work, the bottom hole pressure is limited to values below the local vertical stress, which precludes formation damage. If higher margins of safety are required, an increased cushion gas volume as well as longer screen sections in combination with horizontal wells provide technical options for reducing pressures while maintaining

the higher air mass flow rates required. The maximum allowable well BHP is limited to 130 bar, a value derived from the local geological stress regime and corresponding to 84% of the minimal horizontal stress of 0.15 bar/m [Röckel and Lempp, 2003]. Minimum well BHP during air withdrawal is 80 bar for all wells, to provide the high gas flow rates required during storage unloading. The expected pressure loss along the well for the given pipe setup (see Table 3.2) is accounted for in the power plant model using the Darcy–Weisbach approach (eq. 3.5).

Table 3.3: *Main geostorage parameters for scenario simulation.*

Parameter	Value
Dry air composition	$N_2/O_2/Ar/CO_2$ (0.7553/0.2314/0.0129/0.0004)
Molar mass of air	28.965 g/mol
Critical temperature	132.53 K
Critical pressure	37.86 bar
Air density at standard condition	1.205 kg/m^3
Initial pressure gradient	0.105 bar/m
Reservoir temperature (isothermal)	311 K
Permeability	700 mD
Porosity	0.27
Residual water saturation	0.15
Residual gas saturation	0
Max. relative gas permeability	0.9
Max. relative water permeability	1
Capillary entry pressure	0.1 bar
Pore size distribution index	2
Initial air in place mass	5.56 Mt
Maximum/minimum allowable BHP	130 / 80 bar

3.2.4 Integrated PM-CAES assessment

To conduct an integrated assessment for PM-CAES as illustrated in Figure 3.1a for a potential storage site three major steps have to be evaluated. In the first step, as shown in flow diagram Fig. 3.1b, using the geostorage and power plant models, the dimensions and energetic characteristics of the coupled power plant - geostorage are determined. As a result of this step, power plant interface and dispatch model inputs are derived. In the second step, the dispatch model is used to generate optimal hourly operation patterns (Fig. 3.1b, dispatch model). In the third step, the technical feasibility of the predicted optimal operation is verified and assessed using the coupled geostorage and power plant models via the simulator interface.

The dispatch model connects the physical PM-CAES with an economical assessment. The operational revenue of the power plant is calculated for each scenario year using the shadow electricity price on an hourly basis. Costs occur during energy storage, as the electric energy required for the compressors is obtained from the market, and revenue is generated by selling electric energy back to the market. For diabatic setups, the additional costs for fuel and CO_2 emission allowances during discharging have to be accounted for. Furthermore, variable costs of operation for both charging and discharging are set to account for maintenance. High fluctuations of electricity prices, i.e., a large spread between maximum and minimum prices which can be economically exploited, increase the PM-CAES dispatch. For D-CAES, a higher CO_2 emission price as well as a higher fuel price increase costs and thus reduce the economic attractiveness and therefore the dispatch of the storage facility.

To inform the dispatch model of the physical properties of the plant and the geostorage, a response surface linking pressure, mass flow and power for both charging and discharging as well as shut in periods of the geostorage is constructed from a set of precalculated and linearly interpolated operating conditions. For this, multi-rate injectivity and deliverability tests with injection and withdrawal rates varying from 80 kg/s to 640 kg/s over 7 days each are performed, as well as pressure fall-off tests, where air is injected at a constant rate of 320 kg/s for 20 days followed by an 80-day pressure fall-off. Thus, the transient three-dimensional storage processes occurring in the subsurface are accounted for in the energy system model when identifying economically feasible storage operations and load profiles while avoiding the long run-times of the fully coupled model during optimisation. An additional constraint in the dispatch model ensures that the storage filling level at the start of the scenario year is identical to the level at the end, to guarantee the long-term operation of the PM-CAES. The dispatch thus generated by the dispatch model us then used as input for the fully coupled power plant and geostorage model to simulate all physical

processes in the power plant and the geostorage and thus to verify the operation pattern.

Depending on the energy system scenario year, the electrical energy charged into or discharged from the storage varies from 148 GWh to 305 GWh and from 89 GWh to 531 GWh, respectively (see Table 3.1). Frequent storage operation and the charging and discharging of high amounts of energy occur for scenarios with high RES shares in excess of around 80%, high fuel prices and emission prices greater than 126 EUR/t. The developed framework facilitates the realistic assessment of the power plant facility and the geostorage within the time-dependent energy system and the evolving power markets by comprising the precise subsurface geological storage setting with all relevant storage processes as well as the technically detailed surface power plant. Use of the PM-CAES is evaluated from an operator's perspective to maximise the plant's operating profits within the specific scenario for the future energy system. To this end, the time-dependent relevant economic parameters, such as electricity price, as determined in the energy system model, are passed to the site-specific power plant and geostorage models.

3.3 Results and Discussion

The sections that follow present and discuss the results of the energetic evaluation regarding the different energy system pathways, the variations in power plant technology and design variations for storage wells and their relevance. For the first step, the most common power plant concept. i.e., the diabatic plant configuration, is considered under varying economic boundary conditions. For the variations in power plant topology, a near-time future scenario is evaluated, to open up future perspectives. Variations and potential improvements of the geostorage configuration are investigated using the scenario with the most intense use of the storage, as for this case the effects will be most pronounced.

3.3.1 Energetic assessment for the three energy system pathways

The coupled simulation results of three scenarios with a high fraction of renewable power sources in the energy system are presented as hourly loads for each representative year in Figure 3.3, depicting power rates, cumulative energy and required cumulative heat representing the power plant operation, as well as storage pressure and air-in-place representing the subsurface storage. The blue line in Figure 3.3 represents the actual power from the PM-CAES, while the red squares represent the target power required by the energy system

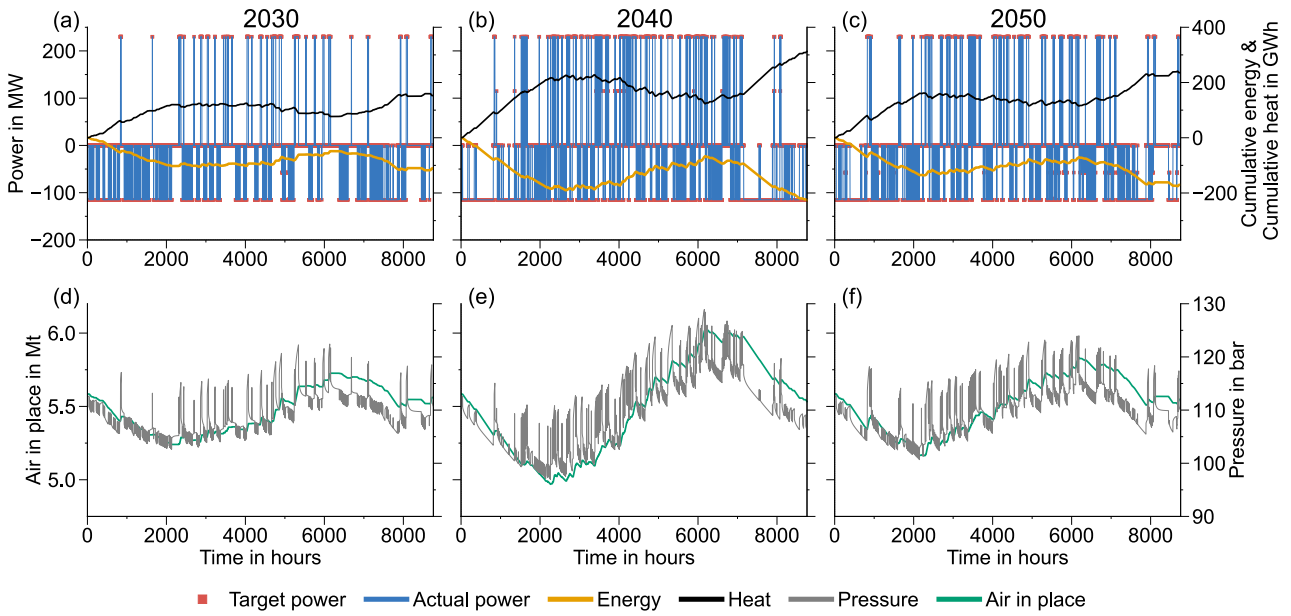

Figure 3.3: Coupled simulation results for scenario year (a) 2030; (b) 2040; and (c) 2050 using a diabatic power plant setup. The start of simulation is January 1st. Positive power or energy designates loading of the storage and negative power unloading. Air-in-place in the storage and storage pressure for scenario years (d) 2030, (e) 2040 and (f) 2050. More frequent storage use and higher discharged cumulative energy correspond to greater pressure and air-in-place fluctuations.

model. The solid orange line is the energy provided by the storage to the energy system, while the black line is the amount of heat required due to the diabatic concept. Figure 3.3a indicates that for scenario year 2030, with a RES share of 76%, the PM-CAES facility provides power to the energy system for 2291 hours and an overall electrical energy output of 259 GWh. Given the diabatic design, this requires 301 GWh of additional heat input. For the scenario years 2040 (RES=86%) and 2050 (RES=100%) the storage facility provides power for 4619 h and 3600 h with annual electrical energy outputs of 531 GWh and 401 GWh, respectively (Fig. 3.3b, c). The target power required by the energy system can be satisfied by the PM-CAES system in all instances, and no power mismatch occurs at any time. The cumulative electrical energy balance reveals that more electrical energy is discharged than stored. This is an effect of the additional heat source required by the diabatic set-up, as this energy difference is added in the form of heat during the expansion step. The corresponding cumulative electrical and heat energy amounts are reported for all scenarios in Table 3.4. Storage pressure is a key parameter characterising the subsurface storage site during operation, as this is the pressure that needs to be reached by the compressors during air injection as well as the pressure provided during withdrawal. At the same time the storage pressure may not exceed the allowable pressure limits (see Section 3.2.4) to avoid formation damage. The applied mass flow rates are automatically throttled if the storage pressure approaches the defined limits. Figures 3.3d, e and f indicate that the storage pressure for all scenario years falls within the allowable limits of 80 and 130 bars. Thus, all injection and withdrawal rates required by the energy system can be supported. Close inspection of sce-

nario year 2040 reveals that the storage pressure reaches 129 bar during charging (at around 6000 h), indicating that the storage site is operating close to the maximum rate. In Section 3.3.3, optimisation of the storage well design is investigated to avoid these conditions. The minimum observed storage pressure during discharging for all scenario years was above 95 bar, indicating that the storage site could accommodate even higher withdrawal rates. At the end of each scenario year, storage pressure is close to its initial condition and above the hydrostatic pressure of 105 bars, demonstrating that the determined power rates and the inferred air mass flow rates permit long-term operation. A second key parameter character-

Table 3.4: *Summary of scenario simulation results with both power plants averaged storage efficiencies (6 cycles).*

Scenario year	Power plant	Cumulative electrical energy [GWh]		Cumulative heat [GWh]		Storage efficiency [-], diabatic at η = 58.5%
		During charging	During discharging	During charging	During discharging	
2030	D-CAES	148.1	259.0	148.2	301.0	0.547
2040		304.9	531.2	296.4	617.2	0.546
2050		230.5	400.9	230.6	466.2	0.542
2030	2-AA-CAES	150.0	89.1	139.8	103.8	0.662
2030	3-AA-CAES	150.6	90.2	139.7	99.7	0.670

ising geological PM-CAES is air in place (Fig. 3.3d, e, f), which represents the total amount of air at the storage site. Analogous to pressure, greater changes to air in place are observed for scenarios with high RES shares, with maximum changes to the stored gas falling within the range of 6%–11% (0.34 Mt–0.62 Mt) of the initial air in place. As discussed in section 3.2.4, the CO_2 emission price and the fuel price both affect the storage dispatch, with rising prices reducing dispatch as the storage operation becomes less economically attractive. The evolution of the air-in-place clearly shows, that the storage operations have a long-term seasonal pattern in addition to short-term fluctuations, with an effective storage loading during summer and unloading during winter. The initial air in place of 5.6 Mt is large compared to the amount cycled during a one-year period. This supports a stable air-water contact level in the geological storage formation, minimising the energy required for moving formation water during the cyclic operation. This allows for high injection and withdrawal rates and thus a higher overall efficiency.

A prerequisite for the stable long-term operation of the PM-CAES is that air injection and withdrawal are mass balanced over the yearly cycle, in order to keep the air in place mass

stable and thus ensure an adequate pressure support as well as the high injection and withdrawal rates. All load profiles shown here are mass balanced within 1%, and the proposed method would ensure this mass balance during storage operations by, for example, compensating for slight mismatches in subsequent cycles. The duration of the discharging periods is generally short, typically on the order of a few hours. However, also longer energy shortage periods occur in the energy system, with the PM-CAES system continuously providing energy up to the weekly time-scale at electrical power loads of 115 MW. For this, the maximum continuous discharge period was extracted from the simulated scenarios (see Fig. 3.3a, b, c) by identifying the longest sequence in continuous discharge mode within the time series and calculating the cumulative electric energy provided by the PM-CAES during that time. The maximum continuous discharge period reaches 106 h (4.4 d), 273 h (11.4 d) and 429 h (17.9 d) for scenarios 2030, 2050 and 2040, respectively, corresponding to respective cumulative electrical energy outputs of 12.1 GWh, 38.3 GWh and 49.9 GWh. This demonstrates that PM-CAES can be employed to stabilise future energy systems with high RES shares on short-term intra-day as well as up to weekly time scales, for example, by compensating for fluctuating solar energy production or fluctuating wind power production resulting from changing weather conditions.

3.3.2 Technology variations of the surface power plant

Power plant topology plays a significant role in the PM-CAES performance. In addition to the diabatic power plant with heat recuperator, as detailed in Section 3.3.1, two adiabatic power plant topologies were designed, to test different setups (see Table 3.2., Fig. 3.4). An additional thermal storage module is integrated into the adiabatic power plant concepts, whereby the heat released during the compression stage was stored and subsequently used to reheat the air during expansion (Fig. 3.5b, c). All three power plant setups have a lower isentropic efficiency at the control stage compressors and turbines, respectively (see Table 3.2), as the inlet pressure of the first turbine varies for different working conditions and this first turbine thus acts as a control stage. To characterise the power plant setup, continuous charging and discharging tests were performed in accordance with Pfeiffer et al. Pfeiffer et al. [2021]. To test the maximum time period for which the PM-CAES system will be able to store or provide energy, continuous loading and unloading simulations are performed using the same geostorage setup with nine vertical wells (Fig. 3.4). Target power rates are set to 115 MW for discharge and 230 MW for charging (see Table 3.3).

Figure 3.4a outlines the continuous charging test for the diabatic setup. The first mismatch between the target and the actual power occurs after 238 h (i.e., 10 d), due to the power

plant's having reached the minimum required flow rate of 362 kg/s for the target power. This is direct result of the negative feedback between required mass flow rate and pressure during charging as explained in Pfeiffer et al. [2021], where the increasing storage pressure results in a decrease in the required mass flow rate to achieve a given target power. After 329 h (13.7 d), the maximum allowable storage pressure of 130 bars is reached. Form this point onwards the operation of the plant is restricted by the geostorage (pressure limit) and the power plant (minimum flow rate limit) itself which results in decreasing power uptake. After 847 h (35.3 d) the injection flow rate reaches the lower technical limit of the compressor and the storage facility is entering a shut-in mode and no gas is injected. After the air injection phase has been completed the pressure within the storage formation continues to equilibrate, resulting in a pressure reduction at the storage wells (Fig. 3.4a).

For the adiabatic setups, the power plant behaviour is similar, but the individual restraints become significant at different times (Fig. 3.4b, c). The upper pressure limit is reached after 490 h (20.4 d) and 392 h (16.3 d), and loading ceases completely after 1023 h (42.6 d) and 918 h (38.3 d) for 2-AA-CAES and 3-AA-CAES, respectively. Maximum mass flow rates of 379 kg/s, 309.4 kg/s and 347.4 kg/s are reached within the first hour of loading for D-CAES, 2-AA-CAES and 3-AA-CAES, respectively, causing storage pressure increases of about 5–6 bars within the first hour. This demonstrates that an adiabatic power plant exhibits high charging performance at lower mass flow rates and consequently also allows for longer continuous charging times than those of the diabatic setup. During compression, the diabatic plant's intercooler reduces the air temperature to 298 K, while for the adiabatic setup the temperature is reduced to only 338 K. Meanwhile, a higher air mass flow rate is required to compensate for the lost temperature contribution to exergy. The continuous discharging tests show that the required 115 MW power output can be sustained for the full 1418 h (59 d) period when using the diabatic setup (Fig. 3.4d). Given that the storage pressure remains significantly higher than the lower limit at the end of the simulation run, even longer discharging times could be sustained. By contrast, for the adiabatic power plant concepts (Fig. 3.4e, f), a power mismatch occurs after 1340 h (55.8 d) for 2-AA-CAES and 1120 h (46.7 d) for 3-AA-CAES, respectively. In the case of the two-stage configuration 2-AA-CAES, only the power plant's minimum operational flow rate of 242 kg/s limits the power output. For the three-stage configuration (3-AA-CAES) additionally, the lower BHP limit is reached after 1251 h (52.1 d). However, this also indicates that an adiabatic concept could provide continuous power to the power grid for longer than 45 d.

In the case of a diabatic plant, the heat released during compression is lost. The installed heat recuperator at the expansion stage absorbs heat from burning the additional fuel in the gas turbine at a temperature of 500 K to preheat air from the storage reservoir at a rate of

134 MW (Fig. 3.4d). For the adiabatic plant setups, heat from compression is stored in an internal thermal storage unit at 338 K. During discharge, the air from the storage reservoir is then preheated to 423 K with a heating rate of 134 MW and 127 MW for the 2-AA-CAES and 3-AA-CAES plant setups, respectively. The 3-AA-CAES plant setup thus requires a lower heat input, demonstrating a higher performance during power generation. In instances of power mismatch, the heat rate declines accordingly, as observed for 3-AA-CAES following 1120 h (Fig. 3.4f). Both charging and discharging tests confirm that a PM-CAES can meet medium-term storage demands and address power shortages in the order of several hours to a few weeks.

To substantiate these findings, the three power plant topologies are also compared for realistic load profiles using scenario year 2030 (Fig. 3.5d, e, f), which has relatively low shadow electricity prices and an impact on dispatch signals and is better suited to comparative analysis (see Table 3.1). All three setups were simulated using the same assumptions for the energy system model and the geostorage model, as Section 3.3.1 demonstrated. The energy system model generates different dispatch signals for the different power plant configurations, as different price signals are obtained.

The different power plant configurations are evaluated here based on air mass flow rate and storage pressure (Fig. 3.5d, e, f). Owing to the high-frequency storage loading and unloading cycles, the longer-term limitations associated with continuous charging and discharging tests are not encountered. Frequent switching to shut-ins or loading/unloading modes equilibrates storage pressure and adjusts the mass flow rate for PM-CAES. Air mass flow rate and

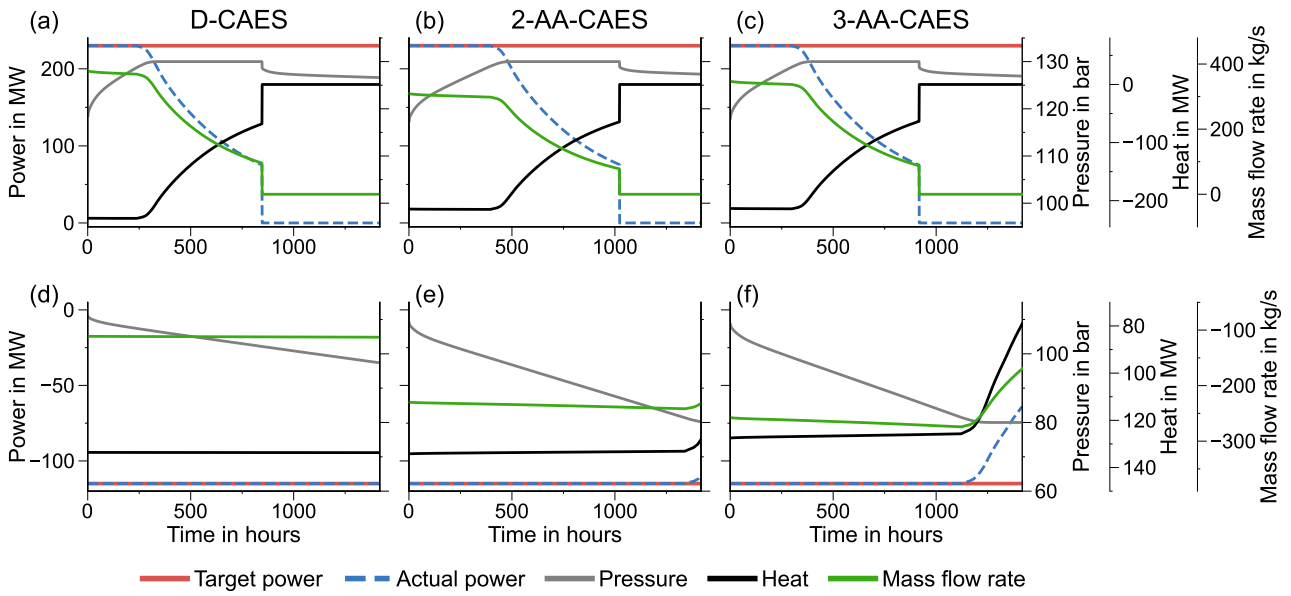

Figure 3.4: Power plant performance during 1418 hours' (59 days) of continuous charging (top row: a, b, c) and discharging (bottom row: d, e, f) for D-CAES (a, d), 2-AA-CAES (b, e) and 3-AA-CAES (c, f).

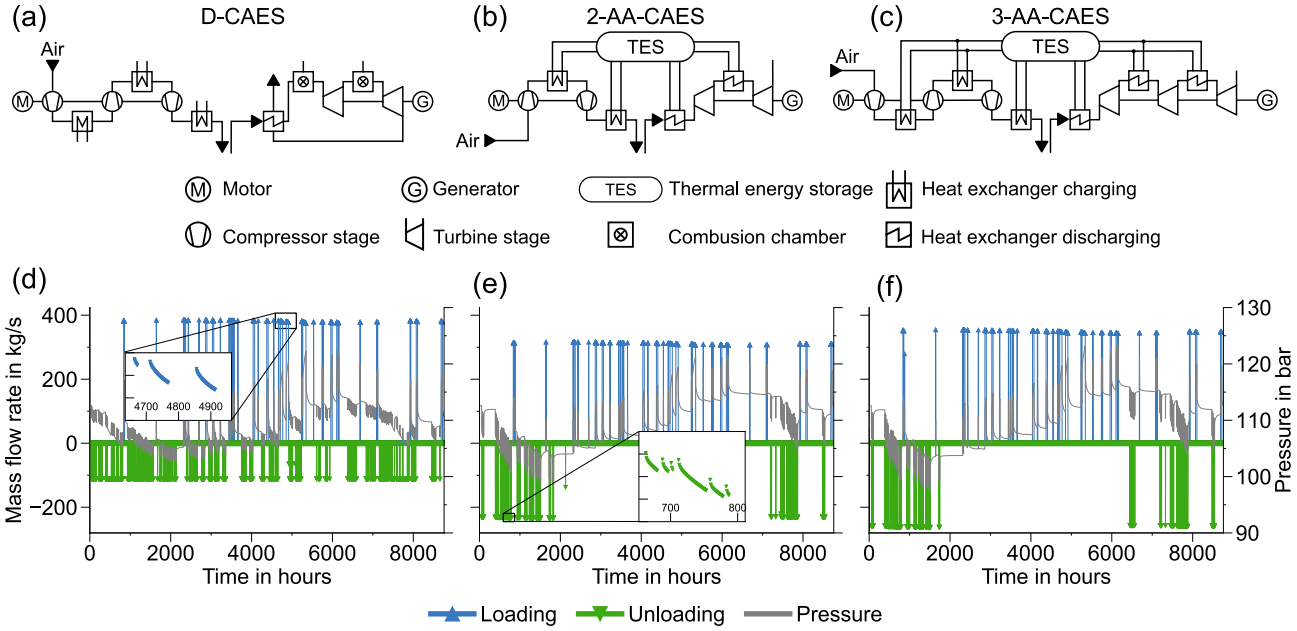

Figure 3.5: Power plant configuration schemes and actual flow rate for scenario 2030 with corresponding schemes for D-CAES (a, d), 2-AA-CAES (b, e) and 3-AA-CAES (c, f). A different flow rate is required to charge/discharge the same power.

storage pressure are thus always within the permissible ranges, and no power mismatches are observed. The maximum flow rate reaches 385.3 kg/s, 316.3 kg/s and 354.5 kg/s for D-CAES, 2-AA-CAES and 3-AA-CAES, respectively, during storage loading. At higher storage pressures, a slightly lower air mass flow rate is required to store the same amount of energy compared to lower storage pressures, as a result of the increased physical exergy at higher pressures, as Figure 3.5d illustrates in the embedded detail from 4700 h to 4900 h.

To sustain the required 115 MW power rate, the adiabatic power plant topologies require mass flow rates that are higher by a factor of about 2.1 to 2.3 than those required by the diabatic setup (see Fig. 3.5d, e, f during discharge), since, in the diabatic case, fuel combustion supplies additional energy. Maximum mass flow rates of 263 kg/s, 233.3 kg/s and 112.1 kg/s are required for 3-AA-CAES, 2-AA-CAES and D-CAES, respectively. This induces a greater reduction in storage pressure for the adiabatic concepts and the occurrence of pressure limitations. This finding emphasises the need to explicitly account for formation pressure history in the geostorage model, both for the high-frequency cycles and the continuous charging and discharging tests and achieved in this study through the application of the coupled model. Although the maximum discharge rate of 115 MW is the same for both adiabatic concepts, the cumulative required heat during annual discharges is 99.7 GWh for 2-AA-CAES and 103.8 GWh for 3-AA-CAES (Table 3.4). To quantify storage efficiency for realistic, strongly fluctuating load profiles, subsets of the load profile must be identified which represent mass balanced time intervals—that is, where injected and withdrawn air mass is equal. Six cycles were evaluated, each representing tens of GWh of charged and discharged

energy, with the average efficiency given in the last column of Table 3.4. For the adiabatic power plant setups, the overall storage efficiency $\eta_{sto,a}$ is the ratio of the energy provided by the PM-CAES during discharging $E_{discharge}$ to the energy used for charging E_{charge}:

$$\eta_{sto,a} = \frac{E_{discharge}}{E_{charge}} \tag{3.6}$$

Overall storage efficiency is found to be about 67% in both adiabatic cases in this study. The storage efficiency estimation for the diabatic power plant setup must account for the external heat source m_{fuel} LHV_{fuel} required during discharge to heat the discharged air from the storage. For calculating the storage efficiency of the diabatic CAES, an approach developed by Tuschy [2008] and successfully applied in former studies [Budt et al., 2016, Pfeiffer et al., 2021] is used. For this, the diabatic storage efficiency is calculated using a reference approach according to assuming a reference efficiency η_{ref}=58.5% for the generation of the additional heat.

$$\eta_{sto,d} = \frac{E_{discharge} - \eta_{ref} \dot{m}_{fuel} LHV_{fuel}}{E_{charge}} \tag{3.7}$$

This corresponds to a modern but not high-end combined cycle power plant and accounts for the fact that the gas could have been used in a gas fired power plant instead of in the diabatic CAES system. The average storage efficiency for the diabatic power plant setup was found to be about 55% with this reference system (Fig. 3.6). Unsurprisingly this reveals that storage and reuse of the heat that occurs during air compression can significantly increase the efficiency of a PM-CAES system, in our case from about 55% to about 67%. However, already at a reference power plant efficiency of around 52% the diabatic storage efficiency would match the adiabatic storage efficiency of 67%. This means that the diabatic system performs substantially better than a combination of the 2-AA-PM-CAES or 3-AA-PM-CAES and peak load generation using an open cycle gas turbine (OCGT) with a power generation efficiency of 35% to 40%, but worse than a combination of any of the two advanced adiabatic PM-CAES topologies together with a combined cycle power plant (CCGT). Both approaches are depicted in Fig. 3.6, showing that the diabatic storage efficiency decreases with increasing efficiency of the reference gas fired power plant, while the adiabatic efficiency is independent of this external reference. The lines cross for a reference plant efficiency of 52%, as stated above. Overall storage efficiency could be increased by using turbomachinery with an improved efficiency, by employing heat exchangers with a lower temperature difference and by applying a higher turbine inlet temperature (in case of the diabatic configuration). Comparing PM-CAES with cavern CAES, it is found that the efficiency is generally lower due to

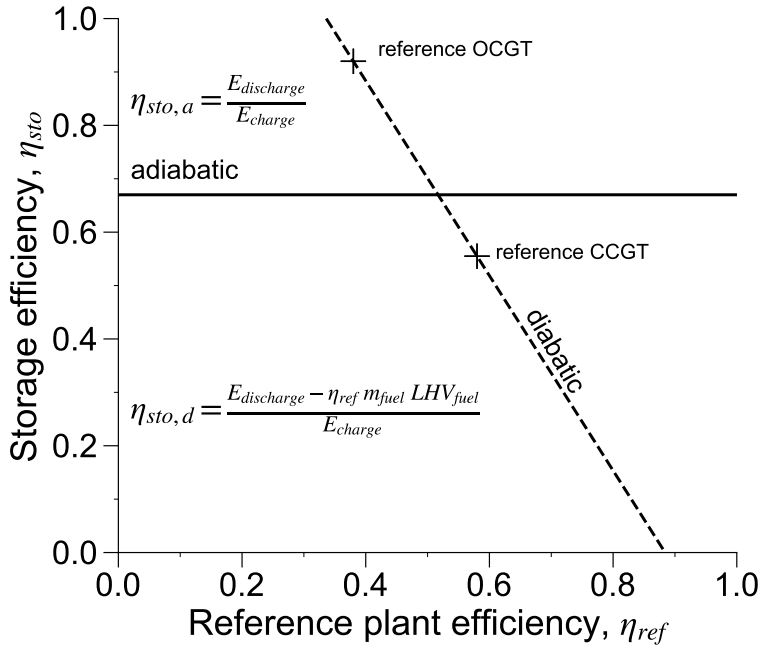

Figure 3.6: Storage efficiency calculation approach for the diabatic and adiabatic plant topologies.

the required pressure gradient at the storage/borehole interface to inject and withdraw the compressed air in the porous formation. This effect is discussed and evaluated in detail in Gasanzade et al. [2021], where three measures to improve the system's overall efficiency are identified: reducing the charging and discharging air mass flow rates, increasing the number of storage wells, and increasing the storage pressure. The first two options reduce the pressure gradients and thus pressure losses during injection and extraction, while the third option reduces the impact of the pressure gradient at the storage/borehole interface relative to the larger overall pressure difference between storage and surface plant.

The different plant designs are also represented in a different energy density (i.e., the ratio of power to required air flow rate), with a value of 0.285 kWh/kg for the diabatic design and 0.137 kWh/kg and 0.121 kWh/kg for the 2-AA-CEAS and 3-AA-CAES, respectively. Again, the difference is a result of the added heat from the fuel of the diabatic design. These values represent site-specific values, accounting for the power plant design and the geological setting and the high-frequency usage cycles associated with scenario year 2030.

3.3.3 Technological variation in geostorage installations

Drilling and completion of boreholes capable of accommodating the required gas flow rates is a proven technology in the hydrocarbon industry. In view of high drilling costs, however, the installation cost of a PM-CAES plant will depend on both the number and lengths of

wells required. A horizontal well has a deviated drilling path above the storage reservoir and thus perforates the storage section horizontally, allowing for increased contact area and thus easier air injection or withdrawal, thus reducing the number of wells needed. Therefore, this study examines whether it is possible to replace the nine vertical wells with horizontal wells that vary with respect to screen length. Scenario year 2040 is applied to investigate the benefits of horizontal well placement, as it is characterised by the highest storage cycle frequency and a high total electric energy output of 531 GWh, causing well effects on storage performance to be most pronounced.

The different well configurations are evaluated based on storage pressure and air in place, as Figure 3.7 illustrates. Two horizontal wells, each with an 850 m-long horizontal segment, are sufficient to achieve the required mass flow rates at storage pressures within the pressure limits (Fig. 3.7d). The horizontal wells have three completion sections of 150 m in length, each within the horizontal segment and one completion at the heel (Fig 3.7a). The larger contact area allows the PM-CAES to operate with lower pressure fluctuations (compare Fig. 3.7d and Fig. 3.3e). The maximum storage pressure was 125 bar at 6160 h (256.7 d), providing a 5-bar safety window to the maximum allowable pressure (Fig. 3.7d). The maximum air mass flow rate during loading is 369 kg/s, which is 5% lower than that for the nine vertical wells, because total pressure loss along the nine vertical wells is higher than along the two horizontal wells. However, this difference occurs only during peak loading and thus has no discernible impact on air-in-place content (compare Figs. 3.7d and 3.3e). If the horizontal segment length is reduced to only 425 m while three completion sections are maintained at a length of 50 m each (Fig. 3.7b), the maximum pressure limit of 130 bar is reached and a power mismatch following 6133 h (255.5 d) will ensue (Fig. 3.7e). A similar behaviour was shown and discussed in Section 3.3.2. At the end of the PM-CAES operation, the air-in-place content is 2.8% lower than the initial value (Fig. 3.7e), as curtailing occurs only during storage loading.

If only three rather than nine vertical wells are drilled at a distance of 425 m (instead of the 400 m for the nine wells), storage pressure will show stronger fluctuations, frequently causing rate reductions as the maximum pressure limit is reached (Fig. 3.7f). This is an effect of the pressure perturbations originating at each storage well overlapping within the formation, causing so-called well interference. The first power mismatch occurs after 4078 h (169.9 d) when the power plant reaches the minimum mass flow rate requirement of 362 kg/s. After 4172 h, the maximum allowable pressure limit will limit the storage operation to reduced charging rates for the next 2946 h/122.8 d (compare Fig. 3.7f with respect to pressure). This causes the air-in-place content to decline from its initial level by around 6%. Although the power mismatch is restricted—as, in most instances, the storage can accom-

modate the power rates required by the energy system—long-term storage operation would be limited as a result of this reduction as a result of declining pressure support and more frequent encounters with the maximum pressure limit in subsequent years. This is already discernible at the end of the simulation at 8670 h when storage pressure has dropped below the hydrostatic level. In the case of such mismatches additional loading cycles must be included in the storage operation with the aim of maintaining the long-term air mass balance and stabilising the storage pressure required to support the high power rates required. The configuration variations demonstrate that, in addition to well number, well

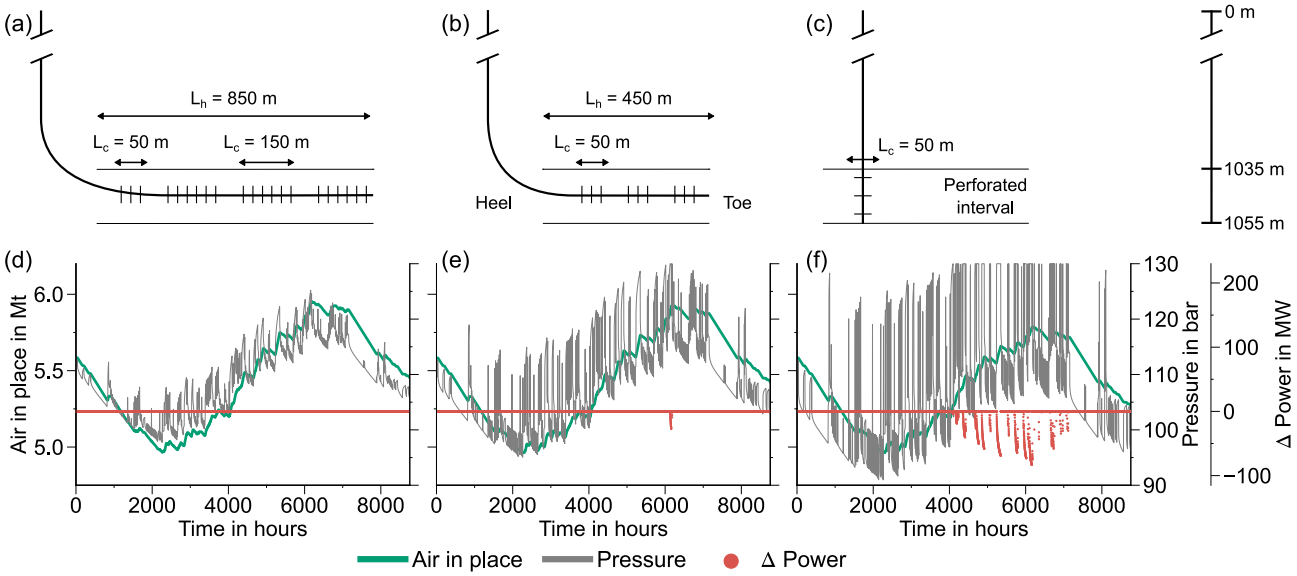

Figure 3.7: Geostorage configuration schemes (top row) and simulation results (bottom row) with (a, d) two wells with L_h of 850 m, (b, e) L_h of 425 m, (c-f) three vertical wells. Red dots represent power mismatches between the target power required by the energy system model and actual power from PM-CAES for scenario year 2040.

type can exert a strong impact on PM-CAES operation and must thus be optimised for any given storage site. The workflow and methods detailed herein constitute a suitable framework for this. Reducing the number of vertical wells or switching to horizontal wells will renders PM-CAES more economically attractive, as construction costs depend strongly on formation depth and well number Lukawski et al. [2014]. Increasing the horizontal segment length, even when the screened sections are maintained at the same length, will reduce storage pressure fluctuations and thus increase achievable air flow and power rates. Moreover, a longer horizontal length section may furnish some backup capacity should increased rates be required in the future, as this would allow for additional or longer completion sections, which may be installed later on during storage operations, if desired.

The PM-CAES simulated herein are designed for grid-scale energy storage and thus require high air mass flow rates, causing significant pressure fluctuations in the storage formation. In order to avoid geomechanical effects, such as formation or cap rock failure, maximum

and minimum pressure limits must be observed. The injection of air into a deep formation may induce geochemical reactions and alter formation properties such as porosity or permeability due to, for example, mineral dissolution or precipitation. Geochemical reactions were not considered in this study. However, as Wang and Bauer [2019] have recently demonstrated, these may only lead to small changes in the petrophysical properties, based on a detected increase in porosity by up to 1% and in permeability by up to 5%. For long-term cycles, a portion of the oxygen injected as part of the air may be lost as a result of some of the induced geochemical reactions [Wang and Bauer, 2019]. This reduction may ultimately affect the operation of the diabatic power plant setup, as oxygen is required for the combustion of fuel to heat the expanding air.

However, for large air in place volumes and frequent cycles, as considered herein, this effect will most likely be minimal because of mixing within the storage and frequent replenishment with oxygen-rich air in the vicinity of the storage wells. Moreover, a large air-in-place volume will also lead to a smaller water–air ratio, thus avoiding the extraction of formation water along with the stored air during storage discharge. These effects indicate that large subsurface PM-CAES sites are preferable to smaller ones.

Compared to the maximum storage capacity of the geological storage site investigated here, which Gasanzade et al. [2021] estimated at around 3.67 TWh (see also Section 3.2.2), only around one-third of the available capacity is required to accommodate the load cycles and capacity demands of the three future scenario years investigated and to provide a base load of 115 MW and up to 50 GWh electrical energy output (see Section 3.2). This demonstrates that a PM-CAES facility will likely encounter rate constraints for both surface and subsurface facilities rather than be restricted by a storage capacity limit.

3.4 Conclusion to this chapter

PM-CAES provides an option for balancing and stabilising future power grids with high fluctuating RES shares. In this study, achievable power rates and storage capacities were determined for a set of realistic future energy system development pathways, and suitable power plant setups and geostorage installations were identified. The following conclusions may be drawn based on the findings:

- The integrated assessment workflow developed in this study has been shown to be suitable for dimensioning, planning and optimising PM-CAES facilities at any potential

storage site worldwide. Storage sites in porous media can be used for GWh PM-CAES applications in future energy supply systems with a renewable energy share of up to 100%.

- The intricate nature of PM-CAES requires specifically designed power plants that account for both the energy system characteristics as well as the geostorage's geological setting. The presented approach allows site-specific design and optimisation of such power plants to be performed for a given energy storage application and market scenario.

- Adiabatic PM-CAES plants do not require additional heat sources and are characterised by low CO_2 emissions but also comparably low storage efficiencies. Additionally, the required thermal storage poses technological challenges as a result of the high rates required. Diabatic PM-CAES may provide higher storage efficiencies; depending on how the required external heat is assessed. However, in today's D-CAES plants this additional heat source is natural gas that would have to be replaced by fuels generated from renewable sources for a 100% renewable energy future.

- Borehole number and well design provide the flexibility to reach the required rates and capacities for a wide range of subsurface conditions and thus allow the application of this technology in sedimentary basins worldwide.

4 Approximating storage in integrated assessments of grid scale energy storage

Part of the content in the following chapter has been submitted for publication and some parts of the chapter have already appeared in the Energy Proceedings:

Firdovsi Gasanzade, Wolf Tilmann Pfeiffer and Sebastian Bauer (2022) Proxy Model Development and Application for Coupled Power Plant and Geostorage Simulations of Compressed Air Energy Storage. doi:10.46855/energy-proceedings-10154

4.1 Introduction

Countries worldwide currently transition from conventional hydrocarbon-based to renewable energy sources to mitigate the effects of climate change by reducing greenhouse gas emissions and diversifying electricity production [Clarke et al., 2022]. However, the fluctuating weather-dependent nature of renewable power generation can negatively impact the stability of the energy system and lead to blackout events [Adamek et al., 2012, Pape et al., 2014]. Therefore, large-scale proven energy storage technologies are required to mitigate these fluctuations and support the economic feasibility of a renewable-dominated energy system. Potential energy storage technologies, such as electrical, electrochemical, chemical, mechanical and thermal, each with unique characteristics, are currently in active use or being researched [Luo et al., 2015, Zakeri and Syri, 2015]. Storage technologies that exploit the energy stored in gases are typically discussed for medium to large-scale storage options. For example, chemical energy carriers such as hydrogen and methane can compensate for monthly to seasonal energy imbalances, or compressed air energy storage can be used to balance the grid during on-peak hours [Kabuth et al., 2017].

CAES is a mechanical energy storage type, whereby energy (exergy) is stored in the form of pressurised air during times of surplus power generation and released during times of peak demand or insufficient renewable power generation. The conversion of electrical energy into high-pressure compressed air has been used for decades to store secondary energy for grid management, such as at the Huntorf site in Germany and the McIntosh plant in Alabama [Succar and Williams, 2008]. The ability of CAES power plants to balance short-term daily fluctuations in energy production within electric grids with a high proportion of renewable energy sources has renewed interest in this technology. CAES can be categorised as an en-

vironmentally benign option that leads to deep grid decarbonisation with fast start-up and ramp rates, allowing operators to quickly respond to changing grid and market conditions by flexibly changing from generation to compression modes [Budt et al., 2016, Wang and Bauer, 2017]. Hence, this study is focused on a storage type that absorbs surplus energy generated from intermittent renewable sources and delivers it back to the grid during peak load to offset volatility in electricity prices, in the same way, that natural gas storage has served the gas market. This may lead to operators bringing the plant closer to a steady state and enhancing grid stability.

Historically, CAES facilities have been deployed in salt caverns for peak shaving and load-levelling applications rather than to meet the needs of the electricity market [Tuschy, 2008]. The most recent commercialised facility at Goderich site in Canada is designed as a merchant plant to compete in the electricity markets, but it only has a storage capacity of 15 MWh. The main limitation of salt cavern facilities is their available volume, which makes scaling up difficult to cover large storage demands. Additionally, suitable subsurface settings for CAES applications in salt caverns are limited by geological conditions [King et al., 2021].To address these limitations, researchers have turned to porous medium compressed air energy storage, which can provide large storage capacities with high charging/discharging rates and can be found in sedimentary basins worldwide [Bradshaw and Dance, 2005]. While decades of CAES activities in porous media did not produce desirable pilot scale results, there is still a large storage capacity potential [Gasanzade et al., 2021, Mouli-Castillo et al., 2019], as well as the technological capability for CAES for power sector decarbonisation.

PM-CAES comprises a power plant on the land surface equipped with gas compression and expansion machinery such as a compressor drivetrain and a generator connected to a turbine. The storage of compressed air is provided by a porous geological formation in the subsurface, which requires a tight overburden to contain the gas in the formation. The compressed air is stored in the pore space of the geological formation, and injection and withdrawal are performed using boreholes with open screen sections. Recent studies have demonstrated that PM-CAES has the potential to operate at a grid-scale level and can offer both large storage capacities and high charging/discharging rates [Gasanzade et al., 2023, Pfeiffer et al., 2021].

The charging and discharging power of a PM-CAES system is highly dependent on storage pressure and mass flow rates, which are strongly influenced by geological factors affecting flow processes within the porous storage formation [Pfeiffer et al., 2021]. However, limitations are imposed during operation by the power plant and the geostorage, such as safe

pressure and mass flow rate limits of individual components. To accurately model all relevant processes and limitations of a PM-CAES system, a simulation tool that couples power plant and geostorage are necessary [Budt et al., 2016]. To this end, a dedicated power plant simulation code (TESPy [Witte and Tuschy, 2020]) and a proprietary reservoir simulator (ECLIPSE [Schlumberger Ltd., 2017]) have been combined and connected through a coupling interface [Pfeiffer et al., 2021]. While the developed tool provides an accurate representation of the storage operation of any PM-CAES, its application for scenario simulations or assessment studies, which typically require the performance of hundreds of individual simulations with varying power plant and geostorage settings, is extremely time-consuming or even unfeasible. Conducting a three-dimensional and transient storage reservoir simulation at large spatial scales poses a high numerical burden. Additionally, the coupled simulation tool requires access to the proprietary ECLIPSE reservoir simulator and a corresponding license package.

In this work, therefore, the focus is on developing a lower dimensional proxy/semi-analytical model for the geostorage component of the coupled power plant – geostorage simulator. The aim is to significantly reduce the simulation runtimes required for scenario analysis and optimisation studies while providing accurate predictions of reservoir pressure, achievable mass flow rates and storage capacity. To this end, the storage reservoir is conceptually simplified so that analytical and semi-analytical solutions for gas flow in porous media can be applied and combined with a storage gas mass balance. The suitability of the newly developed geostorage model is evaluated by comparing its results with those obtained using the full-scale reservoir model for two PM-CAES storage scenarios. The effectiveness of the developed approach in providing rapid and reliable results for evaluating PM-CAES performance is discussed. These evaluations demonstrate the potential of the developed approach to significantly accelerate the assessment of PM-CAES as a large-scale energy storage application.

4.2 Methodology

To accurately simulate compressed air energy storage in porous formations, the intricate and strongly coupled processes occurring within the surface power plant and the subsurface geostorage facilities have to be adequately represented for the wide range of expected operational modes. In a prior study, a suitable coupled simulator has been developed and verified [Pfeiffer et al., 2021]. Subsequently, an integrated PM-CAES assessment framework is developed for dimensioning PM-CAES in renewable dominated energy systems [Gasan-

zade et al., 2023], where a coupled power plant – geostorage simulator is utilised for scenario simulation.

While the accuracy of the coupled power plant - geostorage approach has been demonstrated, it presents several limitations when integrated with a detailed energy system model. Specifically, it requires extensive computational resources and long simulation runtimes, rendering it unsuitable for design studies and sensitivity simulations. The geostorage model is identified as the main contributor to the computational burden of the coupled model. Therefore, to develop a more efficient simulator, an efficient representation of the subsurface storage processes is required. In the following section, brief overview of coupled power plant – geostorage approach is given to explain this limitation.

To model the surface power plant, a set of nonlinear equations based on the power plant topology are generated and solved. These equations provide the target mass flow rate as well as the system pressure required to meet a specific power load. The geostorage model then provides the actual mass flow rate, which can be supported by the geological storage formation, as well as the pressure response of the geostorage by solving the corresponding three-dimensional and transient balance equations based on an extended Darcy's law and mass conservation. Mass flow rates and pressures are coupled at the boreholes and made consistent by iterating between the power plant and the geostorage models.

The following section provides a brief overview of the coupled power plant-geostorage approach and highlights its limitations. A new approach is then proposed to address these limitations and demonstrate its effectiveness in simulating PM-CAES. This alternative approach enables more efficient design studies and parameter variations, offering a valuable tool for optimising CAES systems in future energy systems.

4.2.1 Storage model development

The assumptions for the development of a simplified and thus more efficient semi-analytical solution for the geostorage are based on observations of the typical conditions in the storage required to meet the energy demands. From detailed prior work [Gasanzade et al., 2023, Pfeiffer et al., 2021, Wang and Bauer, 2017] it has found, that a large gas phase is required, which supports the large mass flow rates required mainly by expansion and compression, as opposed to moving the gas–water contact in the porous formation. It could thus be assumed, that the volume of the gas phase in the storage formation is constant and the mass flow rates are supported by varying storage pressure and thus varying compressed air density [Katz

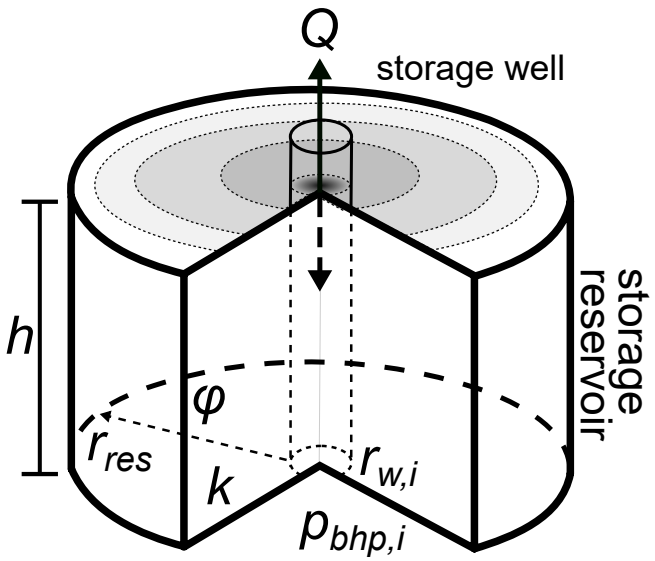

Figure 4.1: Conceptual model with fully perforated vertical storage well in a cylindric reservoir with uniform petrophysical settings. Gray isolines represent pressure responses near the wellbore.

et al., 1959]. Due to the physical laws governing fluid and gas flow in porous formations, the pressure at the boreholes will differ from the storage pressure, due to the pressure gradient required to drive the gas through the formation towards the borehole (Fig. 4.1).

The conceptual model consists of a cylindrical storage reservoir with associated formation petrophysical settings such as permeability k and porosity ϕ, and storage well with borehole radius r_w. The geostorage model employs a gas mass balance calculation based on PVT data for the stored gas, thus linking gas density and viscosity to the storage pressure. The fluid density can thus be calculated after each time step based on the gas mass injected or withdrawn through the boreholes, and can be used to determine the pressure boundary condition pres at the outer boundary of the gas phase (eq. 4.1), assuming a stable gas-water contact level and isothermal conditions.

$$\rho_{res} = \frac{M_{gas}(t-1) + Q(t)\Delta t \rho_{surf}}{V_{gas}(A, h, r_{res}, \phi)} \tag{4.1}$$

with M_{gas} the total mass of gas within the storage formation in kg, V_{gas} is the initial gas in place volume in m^3 and Q the flow rate of gas in m^3/s at surface conditions (in this study 293.15 K and 101325 Pa). Flow to or from the well in a homogeneous storage reservoir of constant thickness are determined using analytical solutions for stationary radial gas flow (eq. 4.2):

$$p_{bhp,w} = -Q\frac{\rho_{surf}}{\rho_{res}}\frac{ln(\frac{r_{res}}{r_w} + s)\mu_{res}}{2\pi kh} + p_{res} \tag{4.2}$$

with $p_{bhp,w}$ the bottom hole pressure at the borehole (Pa), ρsurf the gas density (kg/m^3) at surface conditions, ρres the varying gas density in the storage formation and pres the reservoir pressure at the outer boundary of the gas phase (Pa). k is the formation permeability (m^2) and μ_{res} the dynamic viscosity at reservoir conditions (Pa·s). The radius r_w is the borehole (m), while r_{res} is the reservoir radius of the outer gas phase boundary.

In the context of storage applications, a large borehole diameter or multiple well setups are often required to increase a storage target mass flow rates during injection and withdrawal. The semi-analytical simulator developed in this study accommodates both single and multiple well setups, by applying a superposition technique for the individual pressure perturbations caused by each well the reservoir pressure is obtained (Fig. 4.2a). The bottom hole pressure $p_{bhp,i}$ for each borehole is determined at each timestep, and it is limited to safe operating values to prevent mechanical alterations to the formation rock integrity. The user-defined safe operating pressures are set based on the minimum and maximum well BHP limits and borehole radius for each individual well. If the current $p_{bhp,i}$ violates the safe operating pressures, the developed model automatically adjusts the flow rates at the boreholes in an iterative manner to ensure that the safe pressure limits are not exceeded (as illustrated in Fig. 4.2b). The geostorage model described in the previous section has

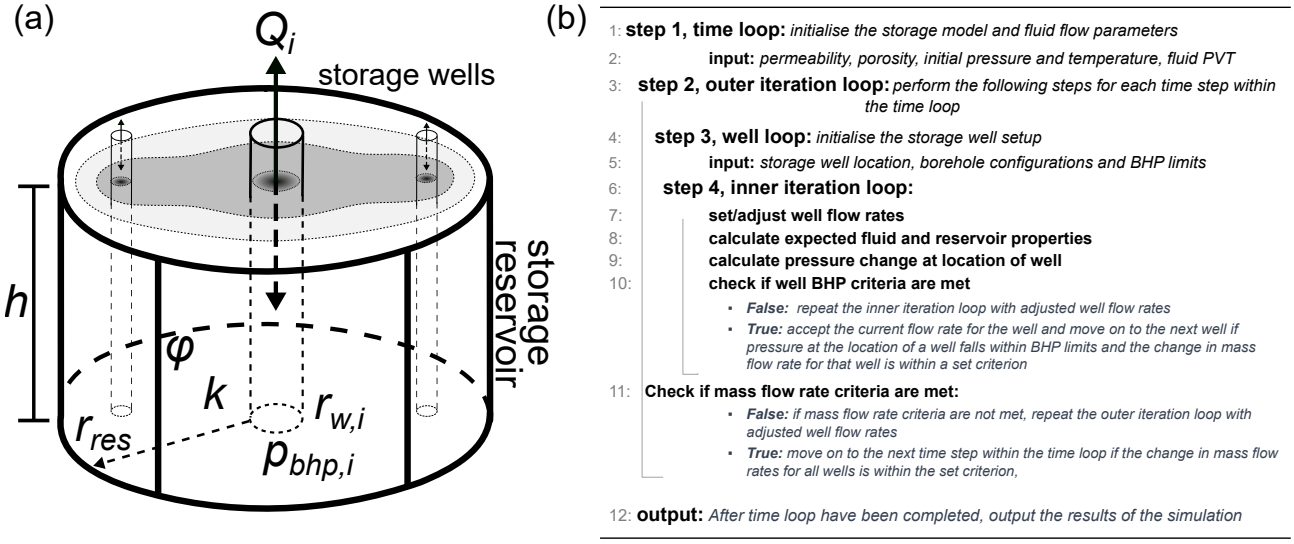

Figure 4.2: (a)Schematic settings of storage reservoir with three vertical wells and calculated bottom hole pressures for various well settings (distance, well radius, limits). (b) Pseudo code of implemented semi-analytical storage simulator with iteration controls.

been implemented using an in-house build code, which facilitates model setup and initialisation, unit conversion and parameter specification. The code comprises a series of input decks that enable the user to define the storage reservoir settings, fluid PVT properties [Bell et al., 2014], and well design separately. To enable efficient result evaluations, simulation output generation is considered for both primary vectors associated with storage wells and the field pressure through the model domain at specific timesteps using ASCII data format.

As a result, the developed method has a reproducible workflow with an efficient simulation analysis feature. The computational efficiency of the geostorage model is crucial for its practical application. The object-oriented C++ code used in the model ensures efficient computation and allows for the implementation of essential features. Additionally, the simulation output generation feature enables convenient analysis of simulation results, which is crucial in optimising CAES system design for energy storage applications.

4.2.2 Semi-analytical storage simulator

To validate the developed geostorage model, a test model is designed with three storage wells in a simplified reservoir with a 500 m diameter. The storage reservoir has a thickness of 10 m, with 20% effective porosity and 0.1 mD permeability. The model is subjected to continuous injection and withdrawal, and cyclic operations for a period of 125 days. Different operation phases, flow rates (0.5×10^6 kg/d, 2.5×10^6 kg/d and 1×10^6 kg/d) and time durations (23 d, 50 d, 7 d and 10 d) are simulated and presented in Fig. 4.3. The simulation results show the target flow rate injected into storage and withdrawal from storage with negative sign, and the actual flow rate that can be partially or fully covered by the storage reservoir. However, all three wells reached the allowable BHP limits, both upper 90 bar and lower 40 bar, leading to reductions in actual flow rates within the first 100 days, even leading to a forced shut-in phase, where the actual flow rate equals zero. At the same time, the target mass flow rates are covered for relatively short time durations and low flow rates during the withdrawal phase, starting from 100 d at 1×10^6 kg/d flow rate and injection phase from 113 d at 0.5×10^6 kg/d flow rate (Fig. 4.3). The results demonstrate the capability of the developed geostorage model to simulate various operation scenarios and its potential for optimizing CAES system design for future energy systems.

The automatic well flow rate adaptation depends on each individual well BHP, which can be affected also by interference effects when the distance between wells is short. Figure 4.4 illustrates the field pressure for the entire model domain induced by storage wells located at a distance of 100 m, therefore pressure interference radiuses are different for central and flank wells (well #2, 3). Therefore, the contribution of well flow rate to the total actual flow rate when the pressure at upper or lower limits distinguishes. The developed tool demonstrates the limitations in storage well planning and enables the consideration of site-specific settings, even for a simplified reservoir model. Post-processing routines allow for rapid results evaluation and visualisation of storage pressure distribution.

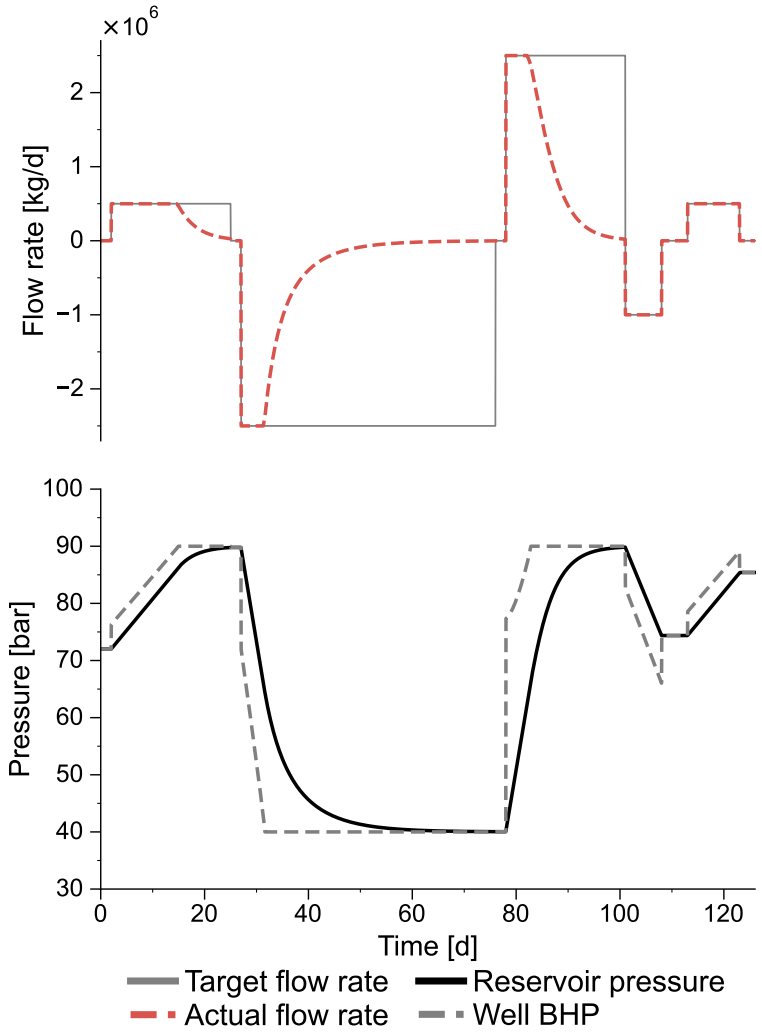

Figure 4.3: Exemplary continuous injection, withdrawal and cyclic operation test with actual achievable mass flow rates from the storage simulator at different storage pressure levels (dashed red lines) and pressure response in the storage reservoir (black solid line) and central well BHP.

4.2.3 PM-CAES application

The application study presented here aims to showcase the potential of PM-CAES for storing renewable energy, using a simplified geostorage model. However, as a prior work, it is important to note that the study considers a realistic energy system with a high share of renewable energy sources and a technically feasible power plant facility. To achieve an integrated assessment, we couple an energy system model with a surface power plant model and a subsurface geological storage model, as shown in Figure 4.5. The energy system model represents the time-dependent power sources and demand over the course of a year and controls the loading or unloading of the PM-CAES storage using a dispatch signal. The power plant model is designed to take into account the geostorage settings, including the formation depth, well setups, and temperature and pressure ranges. To simulate the cou-

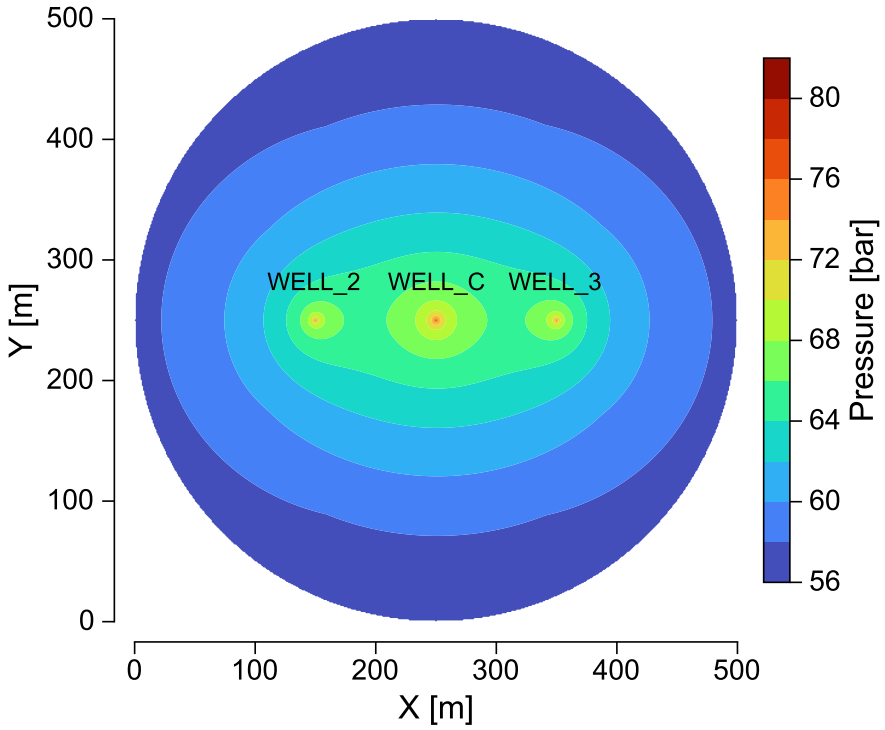

Figure 4.4: Pressure response during build-up phase from three wells located 100 meters apart, the pressure isoline is shown in 2 bar increments, the view is from the top.

pled power plant-geostorage system, the newly developed geostorage model replaces the three-dimensional numerical storage model entirely (Fig. 4.5). This enables us to assess the performance of the PM-CAES system in a more computationally efficient manner, while still capturing the key physical processes of the subsurface storage.

The scenario definition for the application study involves the consideration of two development pathways for the German energy system towards 100% renewable power generation. The input for these scenarios assumes total installed capacities of 218 GW and 183.5 GW for solar and wind power generation respectively and 45 GW for biomass capacity. The detailed pathways for energy system development, including all assumptions on energy supply and demand and the respective technical installations, are well documented in Hilpert et al. [2020]. To perform quantitative predictions, the Open Energy Modelling Framework is utilised to cover Germany and its electrical neighbours [Hilpert et al., 2018], as part of the ANGUS research project [Kabuth et al., 2017]. The energy system scenarios represent possible future energy markets in Germany for varying degrees and types of renewable energy sources, which are reflected in the shadow electricity price, CO_2 emission price, and fuel price. This provides an economic signal for the loading or unloading of the PM-CAES storage via the dispatch signal.

To obtain the power dispatch of the PM-CAES from the national-scale energy system, an

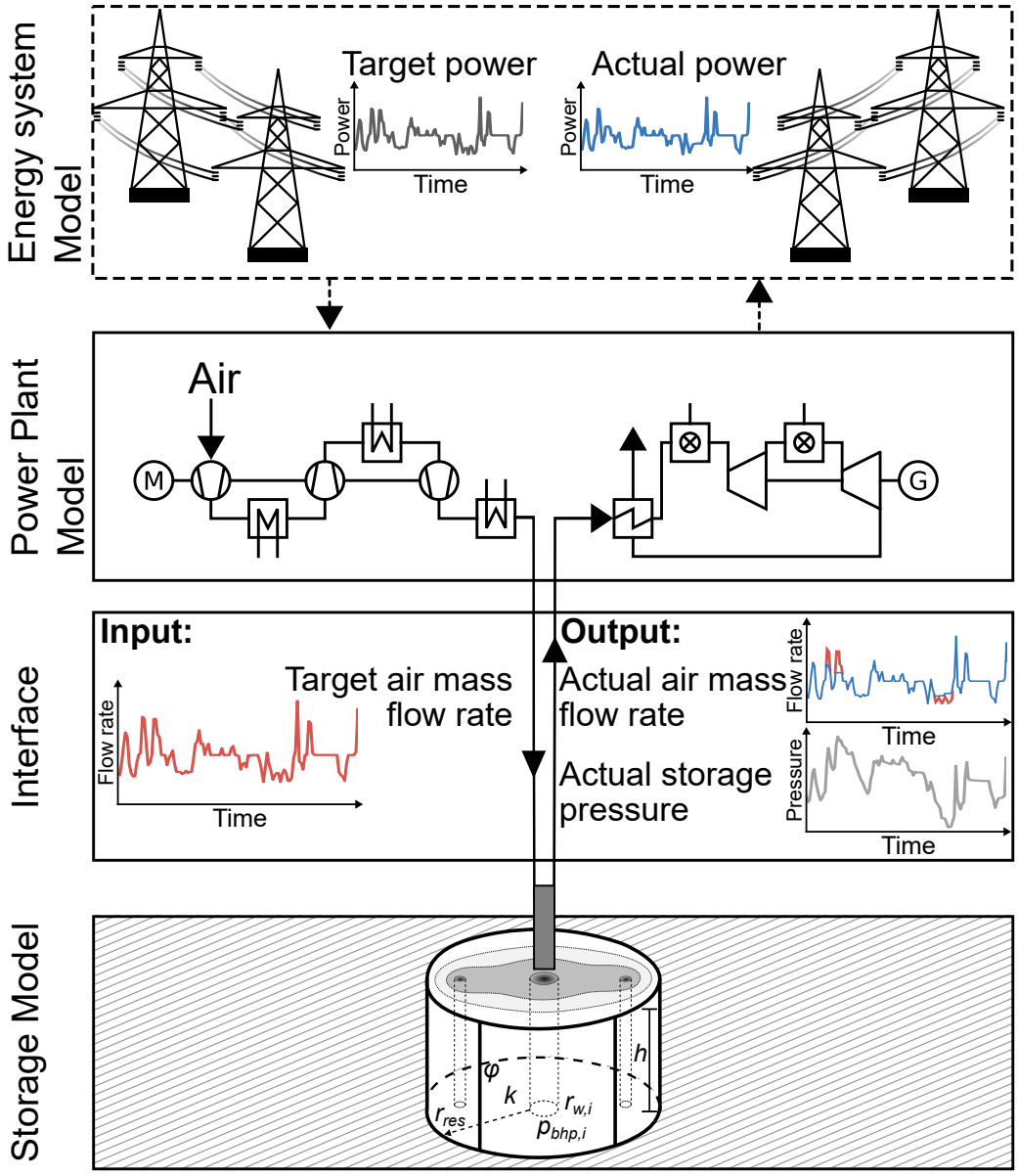

Figure 4.5: Schematic of the coupled simulator for CAES modelling (adapted from Pfeiffer et al. [2021] and Gasanzade et al. [2023]) The diagram illustrates the iterative coupling between a diabatic power plant and a geostorage model, facilitated by a model interface. The power plant is designed to achieve a target air mass flow rate, which in turn generates the required power for the energy system model. The actual air mass flow rates and achievable power at a given storage pressure are calculated by the coupled model, based on the prior history of the coupled system. The geostorage model is represented by a newly developed semi-analytical code.

optimisation scheme is integrated into the energy system model using predefined plant and storage characteristics obtained during the pre-processing design of the power plant. The dispatch optimisation scheme is based on mixed-integer linear programming [Gurobi Optimization, 2021] using a perfect foresight approach, where shadow electricity prices, CO_2 emission, and fuel prices are considered as the economic boundary conditions to generate a time-dependent representation of the electricity load. Two scenarios, namely Scenario #1 and Scenario #2, are generated based on different economic conditions and biomass installation capacity. The scenario generation description for a site-specific PM-CAES setup with

all assumptions is documented in Gasanzade et al. [2023].

The optimised energy system model generated two mass-balanced load profiles with hourly resolution. Scenario #1 requires a total annual storage discharge of 147.713 GWh and 81.550 GWh of charging. In contrast, scenario #2 has a much lower total storage demand of only 54.1 GWh (discharging) and 28.977 GWh (charging) during the year. During discharging, compressed air is delivered from the geostorage to drive a generator for power generation, while during charging, off-peak power at low electricity prices is used for ambient air compression. The energy imbalance of the load profile is compensated by an external heat source for the diabatic power plant facility. The number of charging and discharging cycles varies significantly between the two scenarios. For validation and performance comparison purposes, all simulation runs are performed using both the semi-analytical solution and the numerical solution in the coupled model.

4.2.4 Power plant facility

The performance of a PM-CAES facility is heavily influenced by the design of its surface power plant Despite the existence of only three commercial CAES power plants, with two of them featuring a diabatic power plant design that utilises salt caverns for storage media [Budt et al., 2016]; this design necessitates external heat supply during expansion stages due to the absence of heat storage. In this study, a diabatic CAES power plant with a three-stage compression, two-stage expansion, and a heat recuperator is selected as a realistic test case for the newly developed geostorage model. This design is comparable to the plant in McIntosh, USA (Fig. 4.5). Detailed surface power plant configurations and input parameters for the coupled model are presented in Table 4.1, with a maximum installed power capacity of 50 MW.

The power plant configurations are accurately represented through the use of the open-source TESPy simulator [Witte and Tuschy, 2020]. This allowed for the generation of operating characteristics corresponding to partial load calculations, which are mapped precisely to the components of the diabatic setup. The power plant model utilised a Newton-Raphson method to solve a set of non-linear equations based on the properties and physical operations of each individual component, ensuring the conservation of mass and energy. Numerical solution parameters are used to describe the thermodynamic state variables of the power plant at specific operating points, and operation fields for each unit are determined through systematic calculation of relevant operating points under both injection and withdrawal conditions.

Table 4.1: *Power plant and geostorage parameters for the scenario simulations.*

Component	Parameter	Value
Compressors	nominal power	50 MW
	isentropic efficiency	0.92
	isentropic efficiency control stage	0.85
	pressure ratio at stages	5
Turbines	nominal power	50 MW
	isentropic efficiency	0.90
	isentropic efficiency control stage	0.85
Coolers	temperature after cooling	298.15 K
Generator & Motor	efficiency	0.97
Combustion	fuel type	CH_4
	turbine inlet temperature	1473.15 K
	outlet temperature	423.15 K
Storage	nominal pressure compression	75 bar
	nominal pressure expansion	65 bar
	permeability	500 mD
	initial air in place mass	329 kt
	initial pressure	72 bar
	maximum / minimum allowable BHP	90/40 bar
	well length	720 m
	well number	9
	pipe roughness	0.04 mm
	well radius	0.125 m

The power plant model played a crucial role in the integrated assessment, serving as a mediator between the energy system model and the geostorage model. Hourly dispatch signals are applied to determine times of economically attractive storage operation for both loading and unloading. By accurately representing the behaviour of the power plant components, the model is able to provide a realistic assessment of the system's overall performance.

4.2.5 Geostorage setup

The geostorage model for this study assumes nine vertical wells with an initial pressure of 72 bar and minimum and maximum bottom hole pressure limits of 40 bar and 90 bar, respectively. These pressure limits are taken into consideration to prevent harmful mechanical alterations, such as rock integrity, consolidation, or uplift [Röckel and Lempp, 2003]. The storage model domain has a lateral dimension of 1 km x 1 km with a discretisation of 10 m, and storage wells are fully perforated into a 20 m thick storage reservoir with a porosity of 0.25. The average distance between wells is 250 m with a wellbore radius of 0.125 m.

The well positions are defined elements-wise within a semi-analytical storage simulator. The pipe roughness and length are considered during power plant design, and expected pressure losses are taken into account in the power plant model using the Darcy-Weisbach equation, which takes into account well configurations. The pressure losses reduce the available pressure at the power plant inlet, which in turn affects the amount of work that can be extracted from the compressed air. Therefore, the exergy of the compressed air at the power plant inlet is also affected by the pressure losses. The geostorage model accounts for these effects by simulating the pressure and temperature profiles in the storage reservoir and wells, which are used as inputs to the power plant model. The air used in the diabatic CAES power

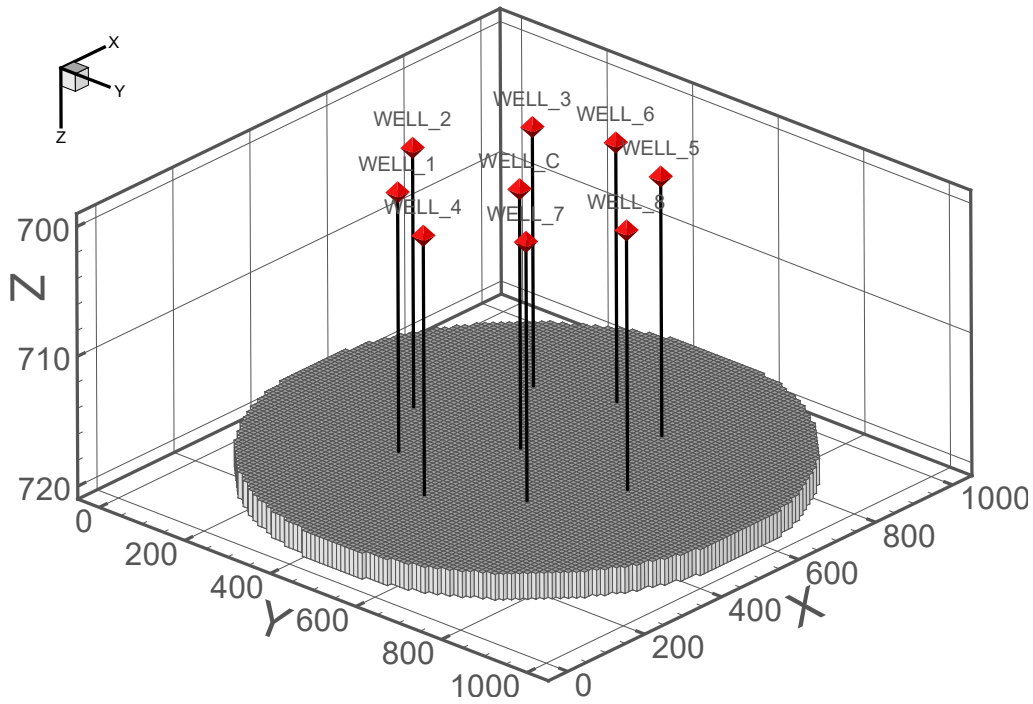

Figure 4.6: Storage model setup for scenario simulation with nine fully perforated vertical wells in a 20 m thick storage reservoir. The deepest slice is visually represented in the figure, with a distance of 250 m between wells.

plant is composed of 0.7553 N_2, 0.2314 O_2, 0.0129 Ar and 0.0004 CO_2, where fluid physi-

cal properties are explicitly defined as pressure-dependent tables using the thermophysical property library CoolProp [Bell et al., 2014]. At surface condition, the density of the air is 1.2046 kg/m^3 and the molar mass of dry air is 28.965 g/mol. The storage temperature is set to 302.35 K, and temperature changes within the formations during the PM-CAES modelling are excluded. To validate the new PM-CAES assessment approach, a full-scale numerical model is applied using the ECLIPSE simulator as a reference geostorage model [Schlumberger Ltd., 2017]. The ECLIPSE 100 black-oil model is used to model the dry gas fluid type with the same pressure-dependent physical properties and corner-point grid for storage model setup. The model discretization and initial conditions are the same, and the model boundary pore volume is adjusted to represent the same initial air in place mass of 329 kt (kiloton).

4.3 Results and Discussion

4.3.1 Scenario simulation

The results of the scenario simulations encompass an annual load profile that takes into account both the energy system and PM-CAES signals. The target power load from the energy system has stochastic charging and discharging modes, where off-peak power with a positive sign is used to compress ambient air into the storage unit at a rate of 50 MW (Figure 4.7). Iterative coupling simulation demonstrates that the dispatch signals can be met by the PM-CAES facility most of the time for scenario #1 (Figure 4.7a). No mismatches between the target power required by the energy system and the actual power provided by the coupled PM-CAES power plant occur during the discharging periods (a total of 3032 hours). The storage pressure at the well bottom hole is always within the specified BHP limits of 40 bar and 90 bar for all nine wells. The minimal storage pressure of 50.6 bar is observed at 2241 h during discharging. Overall, 147.7 GWh of annual electrical energy is generated from the PM-CAES system.

Different mass flow rates are delivered to the surface power plant during PM-CAES discharging, depending on the storage pressure level. The maximum discharge mass flow rate is 53.8 kg/s, with the average being 51.4 kg/s for scenario #1. Storage level analysis is conducted by cumulative air mass calculation, which is the proximity of gas in place fluctuation in a typical porous media storage found in an aquifer system. For scenario #1, the storage level has a seasonal fluctuation pattern, where the minimum level is 213.1 kt and the maximum is 399.2 kt. Such a significant working gas content can mainly/typically be allocated

for porous media CAES applications. For example, large-scale CAES facilities in salt caverns have available cavern volumes in the range of 310 000 m^3– 560 000 m^3, leading to limited working gas content.

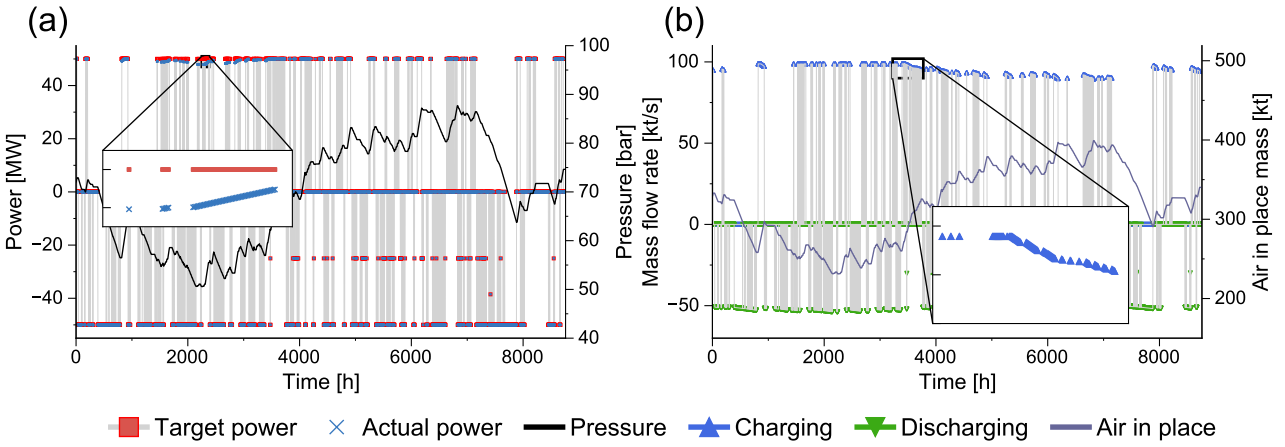

Figure 4.7: Coupled simulation results for scenario #1. (a) Power and pressure profiles were obtained from the proxy geostorage model, where the negative sign indicates the required power for the PM-CAES facility. The inset figure shows the power mismatch between time steps 1450 and 1800 hours during the storage charging phase. (b) Actual air mass flow rates during charging and discharging, and corresponding cumulative air in place mass-storage level. The simulation starts in January 2050. Pressure is shown in the bar and the flow rate is in kg/s.

During the charging periods, a small mismatch between the target power and actual power occurs, as shown in the inset of Figure 4.7a, and the total duration of the charging mode is 1631 hours. However, the total energy stored is only insignificantly lower than the target, with 81.157 GWh stored compared to the target of 81.550 GWh, indicating that this effect does not impair storage operation. The observed mismatch during the charging of the storage is attributed to the specifications of the power plant. Although the storage pressure remains within the allowable pressure range at all times, the low storage pressure (e.g., 51 bar) at the beginning of the charging period results in large target mass flow rates, which exceed the power plant's maximum flow rate limit of 98.8 kg/s, as shown in Figure 4.7b and 4.8b. Consequently, the charging power is reduced to ensure that the maximum mass flow rate is within the plant's specification. As the storage pressure increases, a reduced mass flow rate is sufficient to achieve a given target power, as can be seen from 3000 h onward in Figure 4.7b. The maximum storage pressure during storage feed-in is 87.7 bar at 6820 h, with the end of the simulation year being at a level of 74.6 bar.

The simulation results for scenario #2 indicate that the PM-CAES facility is utilised less frequently when compared to scenario #1 (refer to Figure 4.7a and 4.8a), with a total of 595 hours and 1082 hours spent on charging and discharging, respectively. A total of 54.098 GWh of electrical energy is discharged from the storage, while 28.718 GWh is fed-in dur-

ing charging. The reduced storage demand observed in this scenario can be attributed to the assumed energy system development pathways in Germany, which includes a significant capacity of biomass installations. The obtained results indicate that the PM-CAES system was able to meet the energy storage requirements while satisfying the designated pressure and mass flow restrictions in both scenarios. Nonetheless, it is worth noting that the achieved values fell marginally below the targeted values of 54.1 GWh and 28.977 GWh for scenario #2. Similar to scenario #1, the observed reductions in power rating during the

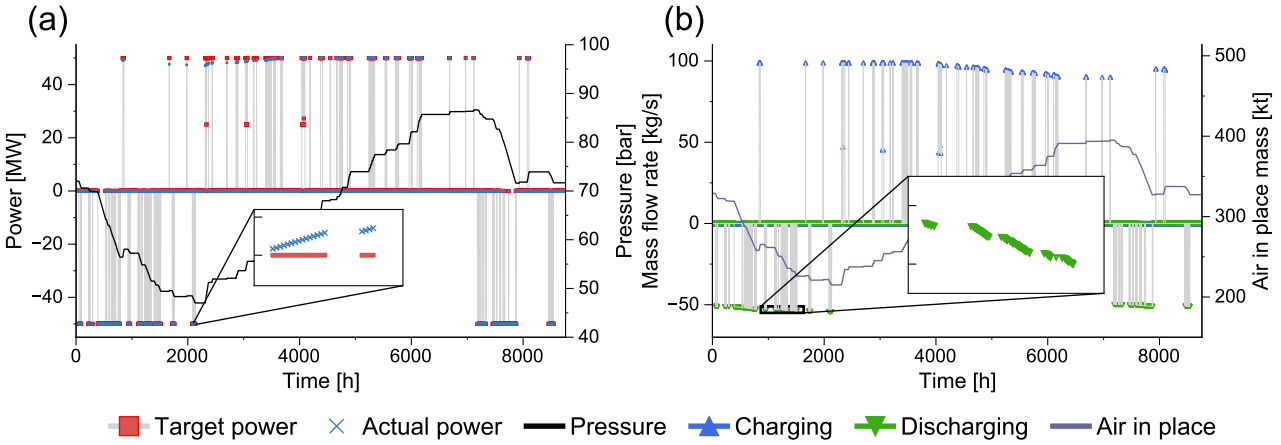

Figure 4.8: Coupled simulation results for scenario #2: (a) actual power and pressure; (b) actual air mass flow rate and cumulative air in place changes from 250 kt to 400 kt.

simulation of scenario #2 (Fig. 4.8a, mismatch), which are also observed during discharging, are a consequence of the limitations in the power plant design. To maintain a constant target power output during discharging, the required mass flow rate increases with decreasing storage pressure (Fig. 4.8b). Given the low storage pressures, the required mass flow rates to maintain the target discharging power of 50 MW violate the power plant's mass flow rate between 2088 h and 2100 h (Fig. 4.8a, embedded figure), and reach the limit of 54.3 kg/s, and the power rate is thus curtailed from 2105 h to 2140 h (Fig. 4.8b). Coupled simulation results demonstrate that the PM-CAES system delivers continuous power during 139 h (5.8 d) in scenario #1 and 60 h (2.5 d) in scenario #2. During the year-long storage operation, the storage pressure remains within a pressure envelope of 47 to 86.6 bars (Fig. 4.8a), and thus within the BHP-limits of the storage formation. The minimum pressure level is observed at 2133 h and reaches a level of 71.7 bars at the end of the operational year. The same seasonal storage level change is presented, where air in place content reaches a minimum level of 215 kt and a maximum level of 395.2 kt.

While most of the time electrical energy demand is predicted for short cycles of a few hours in length, the PM-CAES may also compensate for energy shortages up to the daily scale, supplying electrical power of 50 MW continuously. It is found that the maximum continuous discharge period reaches 139 h (5.8 d) and 60 h (2.5 d) for scenarios #1 and #2, respectively,

corresponding to cumulative electrical energy outputs of 6.69 GWh and 3 GWh, respectively. This demonstrates that PM-CAES can be employed to stabilise future energy systems with high shares of RES on short-term intra-day as well as up to weekly time scales.

In order to discharge the stored energy, an external heat source is required for both scenarios, as the power plant used in this study is a diabatic design. The pressurised air at 302 K reservoir temperature is realised by storage wells and subsequently reheated using an average 58.8 MW thermal power input. The amount of heat required for PM-CAES storage plant is 173.7 GWh and 63.6 GWh for scenario #1 and scenario #2, respectively. The study does not include reference power plant settings and plant topology, assuming the combustion of methane with a lower heating value in the combustion chamber. In terms of energy storage efficiency, the efficiency of the PM-CAES system is analysed through eight mass-balanced cycles. The results show that the average storage efficiency is 0.53 at the reference plant's Carnot efficiency of 0.61 (see Table 4.2 with detailed cyclic analysis results).

4.3.2 Model comparision

In order to validate the accuracy of the new model, a comparison is made between the results obtained from the semi-analytical solution and those obtained from the coupled simulator using the ECLIPSE code. The results, as shown in Fig. 4.9, demonstrate a very good agreement between the two simulation approaches, with the actual power rate difference between the geostorage models being less than 1 MW for both scenarios during the entire storage cycle. The numerical model predicted an annual electrical energy discharge and charge of 147.71 GWh and 81.44 GWh, while the proxy model predicted 147.71 GWh and 81.16 GWh for scenario #1. For scenario #2, the numerical model predicted 54.08 GWh and 28.86 GWh, while the proxy model 54.10 GWh and 28.72 GWh.

Regarding storage pressure, both models show good agreement, with the pressure curves following the seasonal cycle. However, storage pressure in the proxy model has no sharp peaks and during long shut-in periods does not tend towards the initial hydrostatic conditions. The reason for the first effect is the stationary flow assumption inherent to equation 2 for flow to the borehole, while the second effect is due to the assumption of a constant volume of the gas phase. In reality, the gas phase volume expands slightly when pressures are higher than the hydrostatic pressure. For scenario #1, this leads to an annual average pressure difference of up to 1 bar, although pressure from the proxy model may be too high as well as too low. Even though systematic differences exist, the effect on the storage and power plant operation is small and well within the short-term variability of the realistic

Table 4.2: *Cyclic analysis results for both scenarios, start and end of the cycle period is mass balanced.*

	Cycle [h]		Cumulative electrical energy [GWh]		Cumulative heat required during discharging [GWh]	Storage efficiency [-]
	start	end	charging	discharging		
scenario #1	3	8684	79.5	147.7	173.7	0.527
	626	3487	27.0	51.3	60.4	0.522
	862	3443	23.3	44.3	52.1	0.522
	1624	2877	11.0	21.1	24.8	0.519
	4381	7524	27.1	48.9	57.5	0.528
	5000	7390	20.1	36.0	42.4	0.525
	6210	6863	5.4	9.7	11.4	0.536
	6385	7172	7.1	12.8	15.0	0.535
scenario #2	53	8533	28.7	53.6	63.1	0.529
	1252	3040	4.6	8.9	10.5	0.513
	1980	2328	0.9	1.7	2.0	0.509
	5240	7811	8.7	15.8	18.6	0.539
	5723	7698	5.7	10.3	12.1	0.539
	6681	7265	0.7	1.2	1.4	0.540
	6972	7219	0.3	0.5	0.5	0.540
	7813	8455	1.6	2.9	3.4	0.536

load curves, so that the proxy model can be regarded as a valid approximation of the governing storage processes. Table 4.3 provides more detailed information on the comparison of the two models. These results demonstrate the validity and accuracy of the developed new model for simulating the operation of PM-CAES in a renewable energy system.

The current simulation approach has some limitations, particularly in terms of spatial resolution, as it may not be able to capture small-scale geological heterogeneity within the reservoir. This is because the model is based on simplified equations that may not account for all geological parameters. However, recent literature has demonstrated a method for representing heterogeneity in a homogeneous model, which can partially address this limitation.

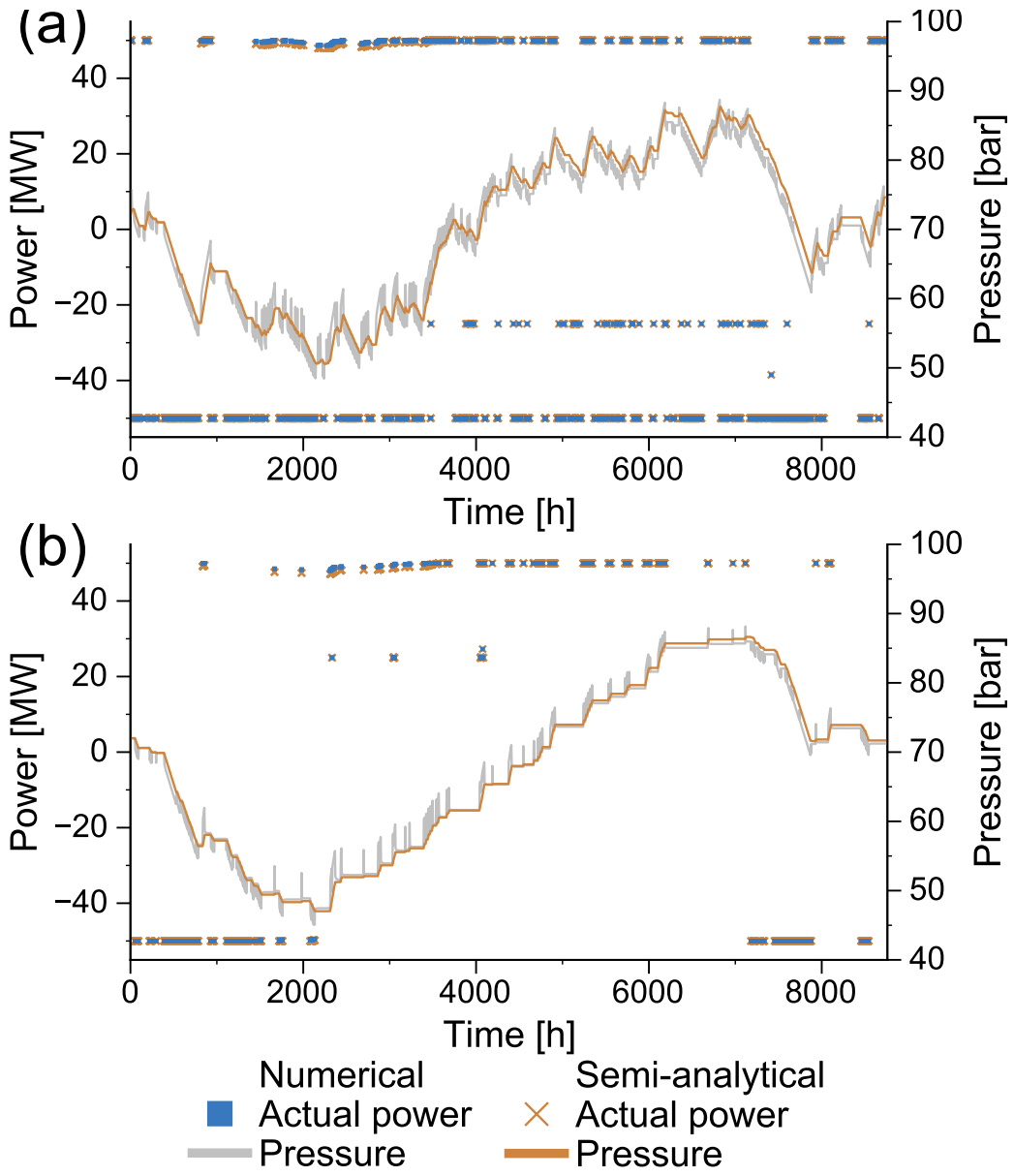

Figure 4.9: Comparison of coupled simulation results between the fully discretised numerical model in ECLIPSE simulator and semi-analytical solution for scenario #1 (a) and scenario #2 (b). Filled square dots represent actual power from PM-CAES at different pressure levels, with shut-in modes excluded for comparison.

Another limitation of the semi-analytical model is that it does not capture all factors that affect temperature changes within the reservoir, such as heat transfer between the fluid and the surrounding rock formation. Additionally, the long-term pressure build-up or draw-down may not be well-modeled in the semi-analytical model, although frequent utilisation of CAES in energy system compensates for this limitation by reducing the need for long shut-in phases. In contrast, this simplified model can be easily used to model CAES in a salt cavern, since the pressure history is absent in salt cavities, this is because salt caverns are relatively homogeneous and have a high permeability, which allows for more linear/predictable pressure patterns.

4.3.3 Computational performance

Both geostorage models are compared also in terms of computational performance. All simulations are run as single-threaded processes on the same workstation using an Intel Xeon E5-1650 v4 @3.60GHz. Figure 4.10 shows the computational performance comparison of the two models. The total runtime for the coupled simulation for one year with the hourly resolution is 2.92 h for scenario #1 and 2.55 h for scenario #2 using the semi-analytical geostorage model. In contrast, the corresponding times using the fully discretised numerical model are 47.7 h and 40.6 h, respectively. Thus, this represents a significant reduction in runtime to about 6%, achieved by using a simplified reservoir model and analytical solutions for the boreholes. Both geostorage code simulations use the same workstation and settings and the numerical model has already been significantly improved by avoiding static parameter calculations (e.g., element transmissibility, grid pre-processing, volume calculation) during every restart using the fast restart option, reducing computation time from hundreds of hours to tens. This study considers isotropic parameter distribution within storage reservoir, considering formation heterogeneity will increase the runtime using numerical solutions, which cannot be modelled using the newly developed method presented here. Although modelling such a reservoir is not technically difficult, the focus of this study is on a homogeneous and isotropic reservoir. Because for the site-selection study or preliminary design usually geological information is limited within basins. To address this limitation, a low-dimensional model can be used for initial facility definition and site selection. This approach is suitable for basins with limited data or where no model is available. After conducting scenario simulations, a detailed numerical model can be created for further analysis, such as deriving rate information. This allows the numerical storage model to be used separately, avoiding iterative coupling and enabling all simulations to be done through a dispatch signal.

Table 4.3: *Comparison of simulation results obtained from numerical and semi-analytical solutions.*

			Semi-analytical		Numerical	
	Target annual energy [GWh]		Actual annual energy [GWh]		Actual annual energy [GWh]	
	discharging	charging	discharging	charging	discharging	charging
Scenario #1	147.71	81.55	147.71	81.16	147.71	81.44
Scenario #2	54.10	28.98	54.10	28.72	54.08	28.86

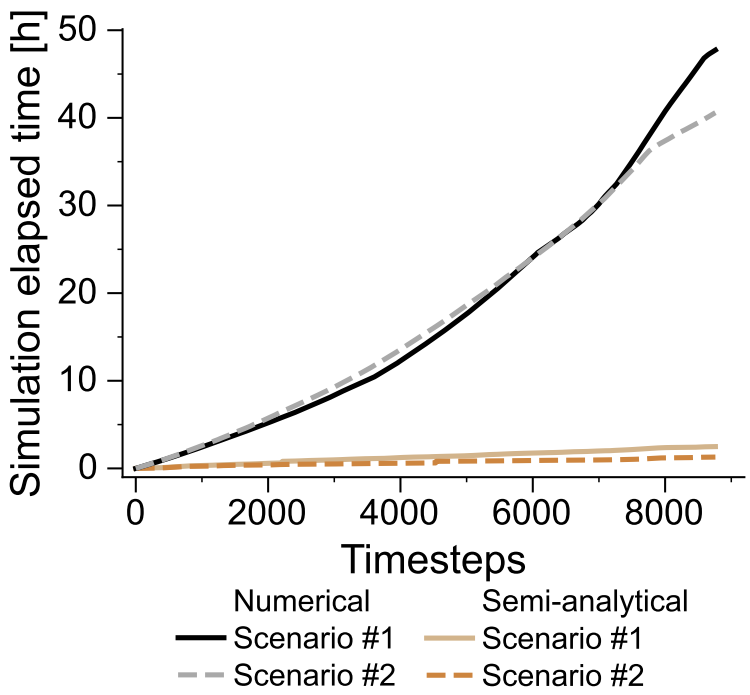

Figure 4.10: Computational performance comparison between numerical and semi-analytical solutions for two simulated scenarios

The semi-analytical geostorage model developed in this study provides a faster and more efficient alternative to the numerical reservoir model for PM-CAES applications. The use of simplified reservoir models and analytical solutions for boreholes significantly reduces the runtime, making it a valuable tool for optimising the design and evaluation of operational conditions for renewable energy storage applications. Further optimisations of the power plant model and coupling routines can be explored to improve computational performance even further.

4.4 Conclusion to this chapter

The study demonstrates that the newly developed approach provides an accurate approximation of the geostorage processes occurring during PM-CAES. The model coupling approach applied here enables the simulation of behaviours and interactions within a PM-CAES system explicitly. The flexibility of the geostorage model allows it to represent typical subsurface storage settings and storage well designs, making it a valuable tool for assessing the feasibility of PM-CAES in future energy system market conditions. Based on the results, the following conclusions can be made:

- The coupled simulator using the semi-analytical solution provides a tool for assessing the feasibility of porous media compressed air energy storage for future energy system market conditions, allowing thus the optimising the power plant set-up and storage operation.

- The storage performance metrics obtained with the semi-analytical solution are in good agreement with those obtained by the numerical geostorage model, even when accounting for technological and geological constraints.

- The developed method can be used for site screening studies to evaluate the potential storage site hypothetical performance characteristics with a feasible power plant and conduct sensitivity analyses, to investigate the impact of various geological and operational parameters on the performance of PM-CAES.

- Subsequent enhancement of computational performance should be done within the power plant simulator and coupled interface code. Future research should focus on optimising these areas and integrating geostorage into national-scale energy system modelling frameworks.

5 Gas leakage through a fault zone during gas storage

Part of the content in the following chapter has appeared in the Advances in Geosciences:

Firdovsi Gasanzade, Sebastian Bauer and Wolf Tilmann Pfeiffer (2019) Sensitivity analysis of gas leakage through a fault zone during subsurface gas storage in porous formations. doi:10.5194/adgeo-49-155-2019

5.1 Introduction

Worldwide, countries are promoting a transition from conventional to renewable energy sources to mitigate global climate change [IPCC, 2014]. In Germany, the so-called "Energiewende" resulted in 31.6% of the total power generation in the year 2016 being based on renewable sources, with the overall aim being 80% by the year 2050 [BMWi, 2018]. However, power generation from renewable sources is stochastic, so that the fluctuating availability of wind and solar radiation can cause challenges for an optimal management of energy system and energy storage on various scales might be required in systems largely based on renewable power generation [Schiebahn et al., 2015]. The geological subsurface and specifically porous formations can provide large storage capacities for gases [Bauer et al., 2013, Kabuth et al., 2017], either for a mechanical energy storage concept utilising compressed air [Mouli-Castillo et al., 2019, Sopher et al., 2019, Wang and Bauer, 2017] or for storing a chemical energy carrier, such as hydrogen or methane [Matos et al., 2019, Pfeiffer et al., 2017, Sainz-Garcia et al., 2017].

The North German Basin has previously been investigated for CO_2 storage [Kempka et al., 2015, Schäfer et al., 2010]. This led to the identification of several potential storage sites [Hese, 2012], which used for storing other gases such as methane or compressed air. However, fault systems exist throughout the NGB, including the identified storage sites, which introduces uncertainty regarding the possibility of gas leakage [Folga et al., 2016, Oldenburg et al., 2002]. Such a leakage of gas would not only result in a reduced gas in place, but also in a potential drop in formation pressure, both resulting in a reduced storage capacity and storage self-discharging over time. Furthermore, gas leaking from a subsurface storage site into shallow formations can trigger chemical reactions and can have an adverse effect on e.g. drinking water supplies Kempka et al. [2015]. Consequently, an assessment of potential gas leakage rates is useful to be able to assess potential impacts prior to any storage development or operation.

The leakage of gas from a gas storage site is driven by the buoyancy of the lighter gas compared to the surrounding formation water as well as the pressure gradient between the storage formation and the fault zone [Chen et al., 2013]. During a gas storage operation, the storage pressure fluctuates several bars, depending on the current operational mode and storage setup, e.g. up to ±35 bars for a hydrogen storage site designed for weekly withdrawal periods [Pfeiffer et al., 2017] and ±41.5 bars for a compressed air energy storage used in a daily storage scheme [Wang and Bauer, 2017]. Studies on gas leakage during natural gas storage show that frequent pressure fluctuations in the storage formation can affect leakage rates through fault zones intersecting the gas storage site [Chen et al., 2013]. In addition to the changes in formation pressure due to the storage operation, also the properties of the fault system and its internal structure affect leakage of fluids. However, such fault zone properties are often unknown and are subject to uncertainties [Faulkner et al., 2003, Fisher and Knipe, 2001, Gibson, 1998]. The effect of existing fault systems on the operation at a potential storage site, i.e. occurring leakage rates and resulting reduction in formation pressure, must be investigated prior to any deployment. This study is aimed at investigating leakage characteristics during a storage operation at a potential gas storage site in the NGB for different fault zone parametrisations. For this, first a geological model of a potential gas storage site in the NGB, which includes six individual faults, was constructed. A hypothetical methane storage operation is designed and the storage operation is simulated using a 3D reservoir model to obtain realistic storage pressures. Subsequently, a sensitivity analysis aimed at determining leakage rates for different fault zone parametrisations is carried out on a 2D slice of the model area.

5.2 Geological storage model

A potential gas storage site must satisfy the following criteria: a sufficiently high reservoir volume to store the desired amount of gas, a high intrinsic permeability to provide the required flow rates and a satisfactory containment of the stored gas [Bennion et al., 2000, Matos et al., 2019]. In the NGB the Quickborn-Volpriehausen, the Rhaetian and the Dogger sandstones are potential storage formations, as they typically provide sufficiently high permeabilities and occur in combination with potential cap rocks [Hese, 2012]. Due to salt tectonics within the NGB, all sedimentary depositions were affected by changes in regional stresses [Baldschuhn et al., 2001, Hese, 2012]. This resulted in formation of potentially suitable geological traps as well as major fault systems [Baldschuhn et al., 2001, Lehné and Sirocko, 2005]. These major fault systems typically strike N-S to NNE-SSW (Fig. 5.1a). Local faults striking in different directions often accompany the major fault systems on the top and sides of salt structures [Baldschuhn et al., 2001, Reinhold et al., 2008]. The combination

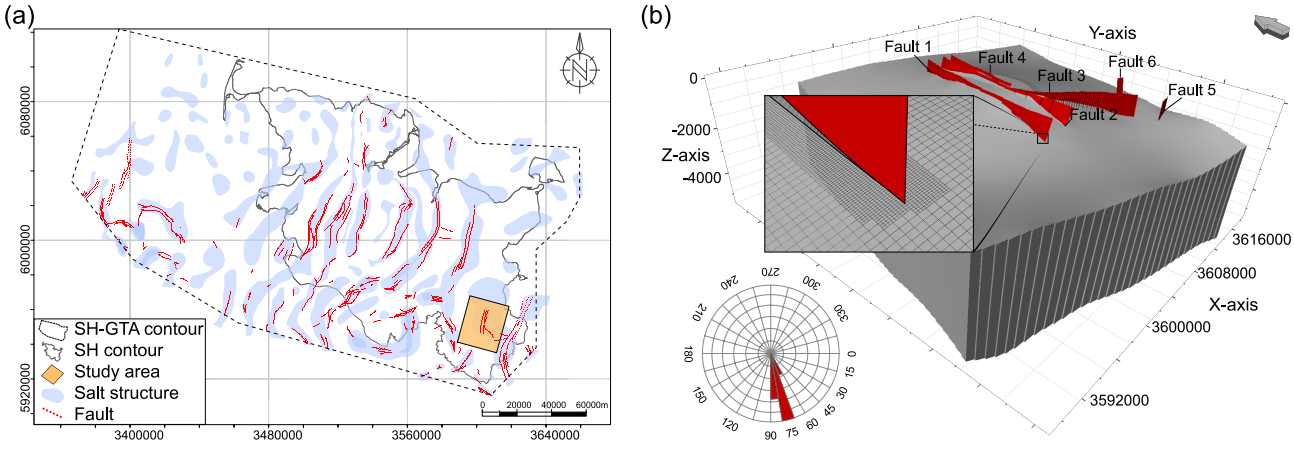

Figure 5.1: a) Salt structures, associated faults and the study area within the NGB in Schleswig-Holstein. The dashed outline is the area of Geotectonic Atlas of Northwestern Germany and the German North Sea within SH (after [Baldschuhn et al., 2001, Hese, 2012]); b) 3D geological structure model created for the study with six fault systems (average dip angle 61° to 82°).

of the number of fault systems and the different strike directions results in a complex sedimentary architecture in the NGB. Structural model used for the investigation of gas leakage from a storage site must represent this complexity and should therefore include all existing structures. In this study, a structural model of a potential storage structure was previously investigated for CO_2 [Hese, 2012] and later for hydrogen storage [Pfeiffer et al., 2017] and is created and used for the scenario simulations. At the storage site, an anticline trap was formed by halokinesis, with normal and reverse faults intersecting with the structure and providing potential leakage pathways for fluid migration (Fig. 5.1b). In the previous study by Pfeiffer et al. [2017], the faults at the study site are assumed to be sealing and boundary conditions were chosen accordingly for the flow simulation model. Of the three potential storage formations in the NGB, only the Quickborn-Volpriehausen and the Rhaetian sandstones exist at the storage site. While the Quickborn-Volpriehausen sandstones are at depths of 1860 m, the Rhaetian sandstones are located at a more suitable, shallower depth of around 400 m. In total, 14 deep (Permian till Paleogene) and 9 shallow (Miocene till Pleistocene) base horizons were used to create the 3D geological model, which has a spatial extend 23.5 km by 27.7 km by 6 km. The modelling was done using the Petrel E&P platform [Schlumberger Ltd., 2018], based on horizon and fault data provided and calibrated based on six well drilling data and seven seismic profiles by Hese [2012]. For each fault system, the geometrical fault-fault and fault-horizon interrelationships are considered. The fault systems are featured in a discrete corner point grid, which enables the representation of the fault zone complexity and allows local grid refinements, according to the requirements of the study (Fig. 5.1b). The structural analysis of fault systems at the study site shows a dip-slip movement tendency. The average dip angle of Faults 1, 3 and 4 is 70°. Fault 2 has a lower average dip angle of 61°, while Faults 5 and 6 show a higher average dip angle of 82°. The primary strike direction is NE-SW, similar to the major salt structures in the NGB

[Reinhold et al., 2008]. The fault systems crosscut the Triassic storage formations and reach up to the Oligocene horizon [Baldschuhn et al., 2001]. The average fault throw is 30 m with a total displacement of 35 m. However, locally the fault throw can reach 200 m and total displacement can be up to 240 m, which can serve as a rough probability indicator for faults acting as a possible leakage pathway [Knipe et al., 1997, Manzocchi et al., 1999, Shipton and Cowie, 2001].

During the formation of such faults, the grains of the host rock are crushed and re-arranged along the deformation band, resulting in the formation of breccias, catalaclasites, ultracataclasites and veins [Aydin, 1978, Caine et al., 1996]. The adjacent rock matrix to each side of the deformation band is typically densely fractured [Caine et al., 1996, Fossen et al., 2007]. The petrophysical properties of these two zones differ significantly, which is commonly represented by distinguishing between a fault core and a damage zone [Aydin, 1978, Caine et al., 1996, Faulkner et al., 2003]. Understanding the fluid flow processes occurring in a fault zone requires the investigation of the main characteristics of the system, i.e. the fault core, the damage zones and the adjacent host rock. The properties of these units affecting fluid flow are hydraulic permeability and capillary entry pressure as well as spatial extent [Knipe et al., 1997].

Due to the aforementioned processes, the fault core typically acts as a barrier towards fluid flow, i.e. the permeability is lower than that of the undisturbed host rock [Aydin, 1978, Caine et al., 1996, Gibson, 1998]. The petrophysical properties within a fault zone formed through a deformation band mechanism are controlled by the host rock properties and permeability reductions of approximately 4 to 6 orders of magnitude compared to the original host rock can be observed [Faulkner et al., 2003, Gibson, 1998, Knipe et al., 1997]. Studies show that the fault core permeability is within the range from 10^{-2} mD to 10^{-6} mD for siliciclastic rocks similar to those found in the NGB [Caine et al., 1996, Faulkner et al., 2003, Flodin et al., 2005, Gibson, 1998, Shipton and Cowie, 2001]. The damage zones are the area or volume of host rock affected by the fault genesis to both sides of the fault core [Aydin, 1978, Caine et al., 1996, Faulkner et al., 2003]. Contrary to the fault core, damage zones typically have hydraulic conductivities that are higher than the respective host rock due to high density of fractures, faults and cleavage [Caine et al., 1996]. For siliciclastic rocks, damage zone permeabilities typically range from 10 mD to 10^{-2} mD [Gibson, 1998, Rinaldi et al., 2014a, Torabi et al., 2013]. Capillary processes can be significant due to the reservoir rock being juxtaposed across the fault zone against the upper formations. Capillary entry pressure is one of the important parameters controlling the fluid flow in such conditions, with values given in literature typically ranging from 4 bars to 100 bars [Flodin et al., 2005, Gibson, 1998, Knipe et al., 1997, Torabi et al., 2013]. Experimental and literature studies have

shown that damage zones can reach up to 100 m on both sides from fault centre, whereas fault cores have significantly smaller thicknesses of less than 0.5 m [Faulkner et al., 2003, Knipe et al., 1997, Shipton and Cowie, 2001].

5.3 Gas storage simulation

The pressure fluctuations induced by a storage operation depend on the thickness and extent of the storage formation, the petrophysical properties of the storage formation as well as the injection/withdrawal history and the underlying storage scenario, which dictates the boundary conditions for the storage operation. For this study, a storage scenario is constructed, based on the assumption periods with no power generation from renewable sources for one week. In 2016 the average weekly electricity demand of the state of Schleswig-Holstein was about 1.04 million GJ [MELUR, 2018]. Taking this as a reference and assuming the efficiency of re-electrification of methane to be 60% [Schiebahn et al., 2015], a storage site must provide 48.4 million sm^3 (at surface conditions) of synthetic natural gas during the period of 7 days to cover the complete storage demand of such scenario.

The storage operation consists of an initial filling of the storage with gas, a cycling storage operation and a subsequent shut-in period. The initial gas injection lasts for 1460 days, during which 263 million sm^3 of gas are injected. The cyclic operation consists of six storage cycles, with the withdrawal rate in each cycle being set to 1.4 million sm^3/d per well. Each withdrawal period is followed by refilling of the storage formation with gas at a rate of 350000 sm^3/d per well for 30 days. Subsequent to the cyclic operation, a shut-in period of 222 days is simulated, resembling a temporary abandonment of the operation.

The storage operation is simulated using five vertical wells located near the top of the anticline at the depths of 429 m, 458 m, 484 m, 514 m and 554 m (Fig. 5.2). The corresponding initial well pressures are 43.0 bars, 46.0 bars, 48.6 bars, 51.6 bars and 55.4 bars. The gradient of the minimum horizontal stress of the suprasalinar sediments in the NGB is estimated to be around 0.15 bar/m [Röckel and Lempp, 2003]. Assuming this to be the fracture pressure gradient and thus the maximum allowable pressure increase, the upper bottom hole pressure values in wells 1 to 5 are calculated as 64.3 bars, 68.7 bars, 72.6 bars, 77.1 bars and 83.1 bars, respectively. The lower pressure limit of the wells during withdrawal were set to an arbitrary 30 bars. Geomechanical processes such as fault reactivation are not explicitly considered in this study. However, with the defined BHP limits geomechanical reactions due to the storage operation are assumed unlikely. To minimise the computational load,

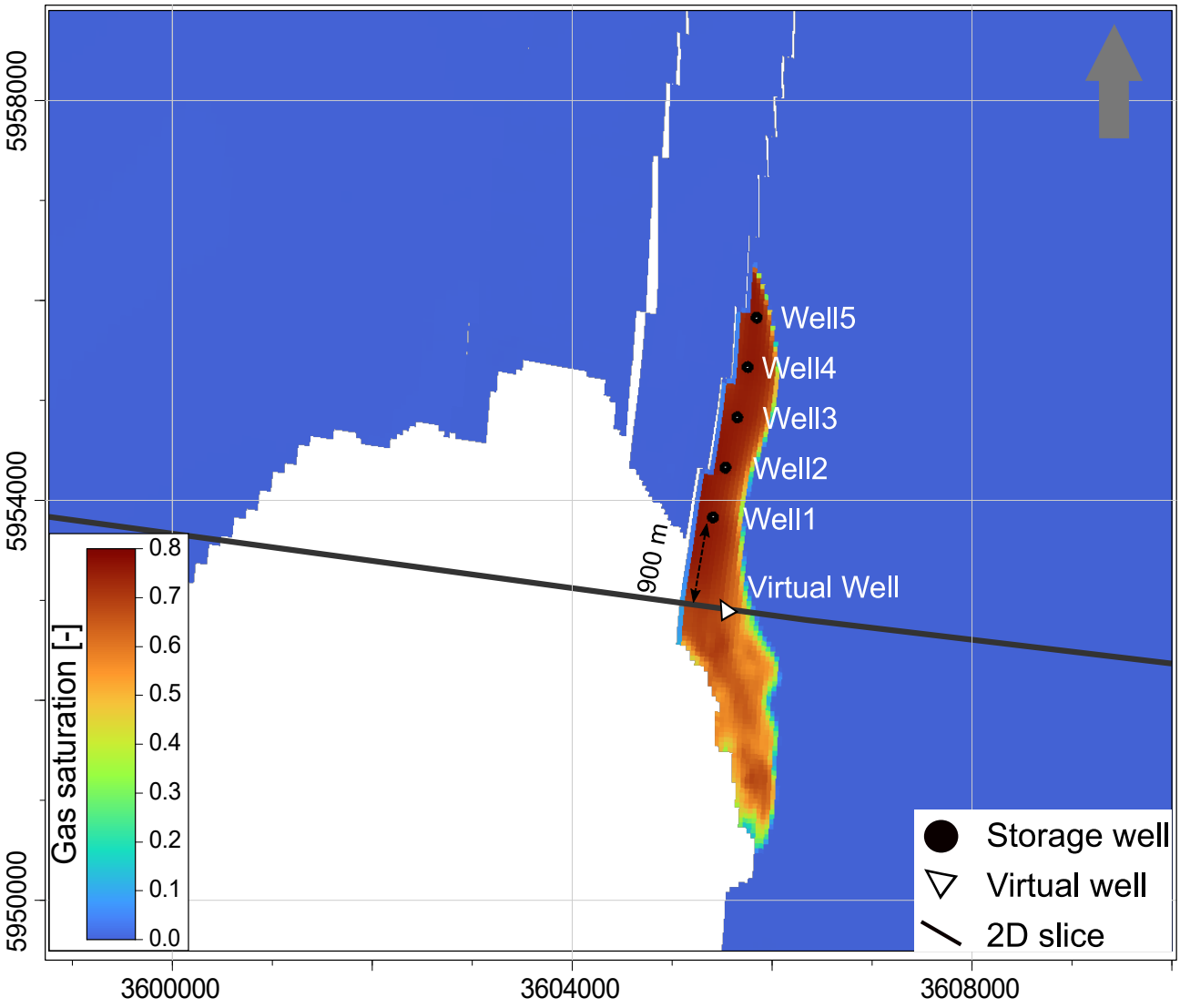

Figure 5.2: Gas phase distribution in the 3D model after the storage initialisation. Five vertical storage wells located near the top of the anticline, 900 m from well 1 is the "virtual" well for pressure controlling in 2D study.

the Rhaetian storage formation and the cap rocks are included in this simulation, with the spatial discretisation 50 m by 50 m in lateral directions. At the storage site, the mudstones of the Lias and the Lower Cretaceous form the cap rocks above the storage formation. However, the Lias is eroded towards the fault axis, so that only the Lower Cretaceous forms a complete seal over the storage formation. The model is discretised in vertical direction by dividing the individual units, i.e. the cap rocks and the storage formation, into a constant number of layers. The resulting vertical discretisation of the grid varies therefore with the local thickness of the individual unit. The storage formation is divided into five layers, with the resulting vertical discretisation ranging from 0.01 m to 26 m. The Lias and the Lower Cretaceous cap rocks are discretised using twenty layers, with resulting vertical discretisation ranging from 0.001 m to 13 m and 1 m to 5 m, respectively. No flow is allowed across the model boundaries, providing a conservative estimation of the pressure changes

Table 5.1: *Model parameters used for 3D gas storage simulation.*

Parameters	Storage formation	Cap rock	Fault core	Damage zone
Permeability, k [mD]	500	10^{-4}	10^{-2}	10^{-2}
Porosity, ϕ [-]	0.30	0.15	0.15	0.15
Residual water saturation, $S_{w,r}$ [-]	0.20	0.60	0.40	0.40
Capillary entry pressure, p_c [bar]	0.20	60	4	4

occurring during the storage operation, as overpressures cannot dissipate. All petrophysical properties are assumed as homogeneous and isotropic within the individual geological units (Table 5.2). The Brooks and Corey formulation [Brooks and Corey, 1964] is used to calculate phase permeabilities and capillary pressure, based on phase saturations. The ECLIPSE E100 black-oil simulator is used [Schlumberger Ltd., 2017], assuming immiscible two-phase flow of water and gas. It was successfully tested in a benchmark paper by Class et al. [2009] for a comparable setting and represents therefore a valid choice as modelling tool. During initial storage filling, the injected gas accumulates at the top of the anticline (Fig. 5.2). The initial filling of the storage is accompanied with a significant pressure increase, so that the BHP in well 1 reaches the upper limit after 300 days, resulting in an automatic reduction of applied injection rates and ultimately in the well being shut after 1410 days (Fig. 5.3). For the deeper wells 2, 3, 4 and 5 the upper limit is not exceeded during the initial filling, with well pressures peaking at 65.9 bars, 67.0 bars, 67.6 bars and 68.3 bars, respectively. The target withdrawal rates of 1.4 million sm^3/d are sustained for all wells in all storage cycles, so that 49 million sm^3 of gas is produced from the storage formation in each cycle. During the first storage cycle the well pressures decrease to 38.5 bars, 37.1 bars, 34.2 bars, 33.3 bars and 34.1 bars in wells 1 to 5, respectively. In the subsequent refilling period, the target injection rates are achieved in wells 2 to 5, while the upper BHP limit is reached in well 1. Thus, less gas can be injected than planned, with the total injected gas volume being 50.9 million sm^3. Regardless, the target withdrawal rates are achieved in every storage cycle, so that the storage site can cover 100% of the storage demand, as defined in this study. The storage pressure follows the trend of well pressure with the magnitude of the pressure change during different storage phases being considerably dampened (Fig. 5.3). After the initial filling, the storage pressure 900 m south of the storage wells, which is the position of the 2D slice used for the leakage scenario simulations, is around 62 bars. During the storage operation, pressure fluctuates between about 60 bars and 55 bars. Thus, the observed pressure changes during the storage operation is 7 bars at the position of the 2D model. In the shut-in period of the storage operation after 1683 days, the storage pressure rebounds

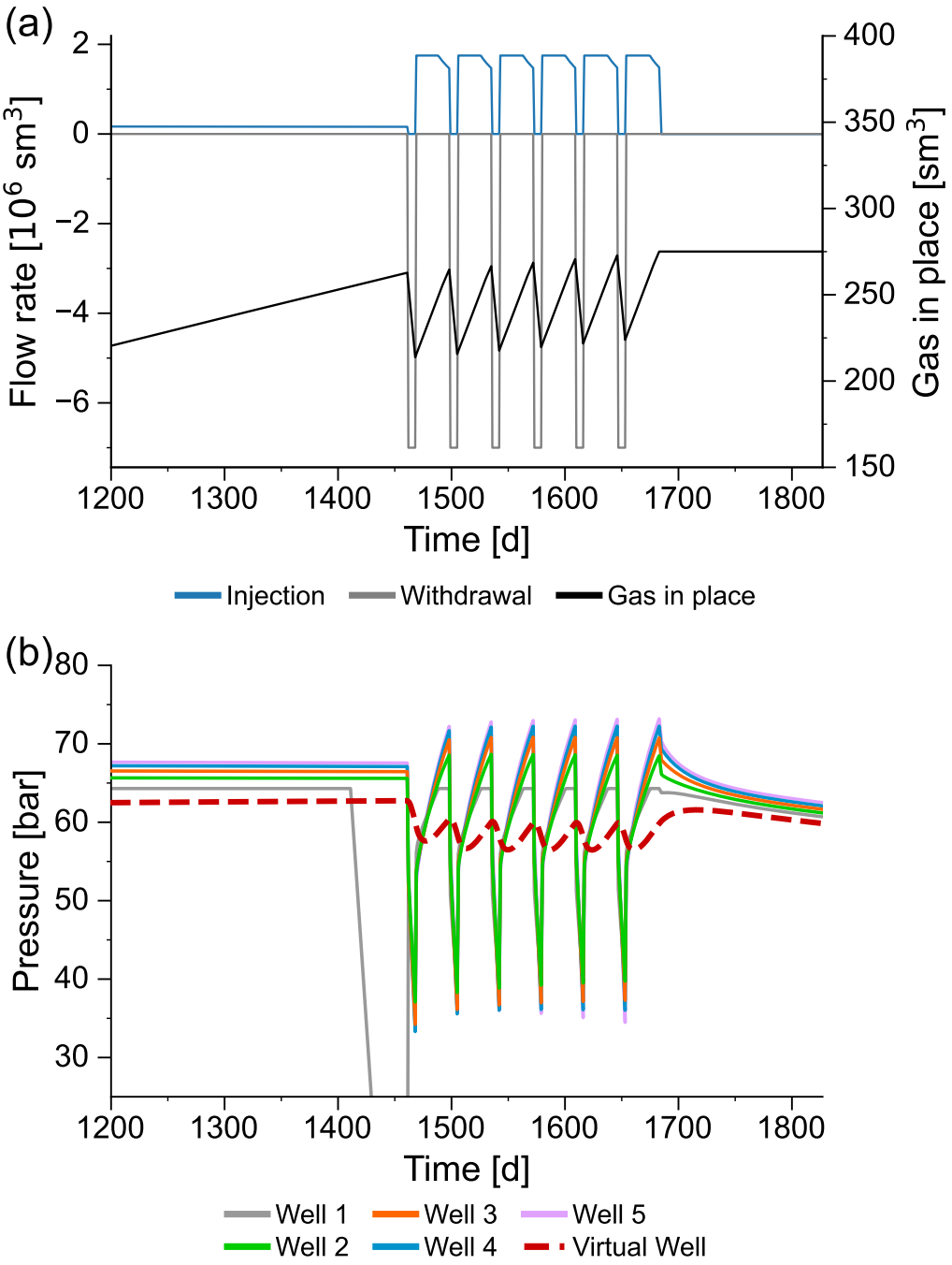

Figure 5.3: (a)The total flow rate during injection and withdrawal phases and corresponding gas in place level; (b) Bottom hole pressure for five vertical wells during the storage cyclic operation starting at day 1461 and the following shut-in period of 222 days; the dashed red line depicts the pressure change at the position of the 2D-slice used for the leakage scenario simulations.

to 62.0 bars and then slowly declines to around 59.9 bars at the end of simulation at the day 1827.

5.4 Gas leakage simulations

For the leakage simulations, only a 2D slice extracted from the full 3D model is used (Fig. 5.2), with the initial and boundary conditions being set based on the simulation results of the full 3D model of the storage operation. The 2D slice is oriented W-E, intersecting with the gas storage at about 900 m south of the storage well 1. The slice position was selected to represent realistic storage pressures, a high local gas volume, as well as a good approximation of the fault-storage interface (Fig. 5.2). At the given slice position, the pressure in the storage formation fluctuates during the cyclic storage operation by 7 bars, as can be seen from the 3D simulation (Fig. 5.3). For a realistic representation of storage pressure, an additional well is placed 350 m east from the fault zone in the 2D model that does not exist in the 3D model. The operation of this "virtual" well is the pressure control, i.e. the temporal evolution of storage pressure in the 3D model is represented by cycling the pressure at the virtual well between the minimum pressure of 55 bars and the maximum pressure of 62 bars observed in the 3D model (Fig. 5.3). The petrophysical properties of the fault damage zone are directly assigned to the grid elements. Using local grid refinement, the first 50 m from the fault zone and the storage formation were refined to grid blocks of 50 m by 1 m in lateral direction. The fault core properties are assigned using transmissibility multipliers at the connecting grid blocks [Manzocchi et al., 1999]. For the leakage scenario simulations, only the cyclic storage phase and the subsequent shut-in period are considered. Thus, the initial formation pressure is assumed to be 62.7 bars (compare Fig. 5.3).

Three different scenario parametrisations are tested in this study (Table 5.2). In the scenario I only the permeability of the damage zone is changed, while in the scenario II the capillary entry pressures are being varied. In the scenario III, both the damage zone permeability and the capillary entry pressure are varied simultaneously based on the Leverett J-function scaling [Leverett, 1941]. For this, 0.01 mD and 4 bars are set as the respective reference permeability and capillary entry pressure. Thus, increasing damage zone permeabilities are accompanied by decreasing capillary entry pressures in the simulation runs of the scenario III.

5.5 Simulation results and discussion

The leakage simulations start with a withdrawal cycle, during which the pressure in the storage formation decreases to values close to 55 bars and the fault zone pressures being 55.0 bars, 55.0 bars, 54.9 bars and 54.8 bars for simulation runs #1 to #4 (Fig. 5.4a). Even

though the pressure differential between the storage formation and the fault zone is small, the gas leaks into the fault zone and rises upwards (Fig. 5.5). The peak gas leakage rates are 325 sm^3/d and 2308 sm^3/d in simulation runs #3 and #4, while runs #1 and #2 show leakage rates below 25 sm^3/d. During the subsequent injection period from day 1468 to day 1498, the pressure in the storage formation rapidly increases, with the fault zone pressure following behind (Fig. 5.4a). Correspondingly, gas leakage occurs with peak rates being 5 sm^3/d, 24 sm^3/d, 325 sm^3/d and 2308 sm^3/d during the first injection for the simulation runs #1 to #4 of the scenario I (Fig. 5.6a). However, the rates quickly decline within the first hours of injection for the simulation case, assuming a damage zone permeability of 10 mD (run #4) with the average leakage rate being 2020 sm^3/d. Contrary to that, the peak and average leakage rates are relatively constant in the remaining simulation runs. During the following withdrawal of gas, the pressure in the storage formation is again dropping to around 55 bars, which greatly reduces the gas leakage for the higher permeability simulation runs (#3, #4) and stops it for in the lower permeability runs (#1, #2) altogether (Fig. 5.4a). The characteristics of the gas leakage rates are similar in the subsequent storage cycles, however, the differences between the peak and average leakage rates during injection increase slightly. In the dormant phase of the storage operation after 222 days of operation, gas leakage rates gradually decrease to around 2 sm^3/d, 35 sm^3/d, 348 sm^3/d and 866 sm^3/d for damage zone permeabilities of 0.01 mD, 0.1 mD, 1 mD and 10 mD, respectively. This happens while the pressure differential between the storage formation and the fault zone remains relatively constant (Fig. 5.4a). For the different capillary entry pressure cases at a constant fault zone permeability of 0.01 mD (scenario II), the gas leakage rate never exceeds 15 sm^3/d during injection (Fig. 5.6b). For the simulation cases with higher capillary entry pressures, i.e. 6 bars, 8 bars and 10 bars, the differential between the gas phase pressure in the storage and the fluid pressure in fault system is not sufficient to result in significant leakage. For the simulation case with the lower capillary entry pressure (run #8), the highest leakage rates of the scenario II are observed. However, the low damage zone permeability retards the advance of the gas phase sufficiently to minimise gas leakage. The low pressure differential between the storage formation and the fault zone inhibits any leakage during the first withdrawal period in simulation runs #1, #5 to #8. The pressure in the fault

Table 5.2: *Model parameters used for leakage scenario simulations.*

Run #	1, 2, 3, 4	5, 6, 7, 1, 8	1, 9, 10, 11
	Scenario I	Scenario II	Scenario III
Damage zone permeability [mD]	0.01, 0.1, 1, 10	0.01	0.01, 0.1, 1, 10
Capillary entry pressure [bar]	4	10, 8, 6, 4, 0.4	4, 1.26, 0.4, 0.13

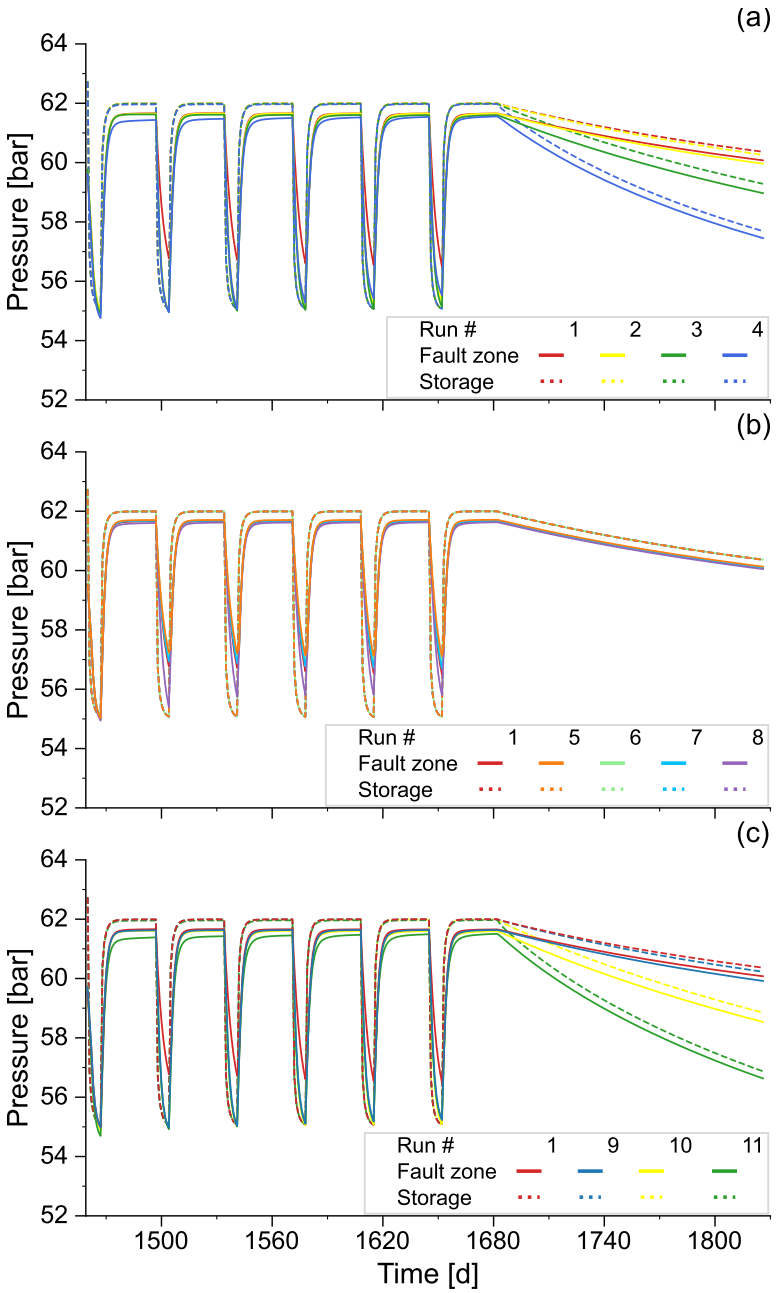

Figure 5.4: Pressure fluctuation during cycling operation in 2D model, solid lines represent pressure in the fault zones: (a) scenario I - for the damage zone permeability cases; (b) scenario II - for capillary entry pressure cases; (c) scenario III - for normalised capillary entry pressure cases.

zone is not lower than the storage formation pressure in the following withdrawal cycles, so that no gas leakage occurs (Fig. 5.4b). In the shut-in period of the storage operation, the gas leakage rates are constant, never exceeding 3.5 sm^3/d.

The overall characteristics of the gas leakage in the scenario III, i.e. when capillary entry pressure is scaled according to the permeability of the damage zone (runs #9 to #11), are similar to the results of the scenario I (Fig. 5.4a, c). However, the gas leakage rates are generally higher than in the scenario I, with peak leakage rates being 30 sm^3/d, 473 sm^3/d

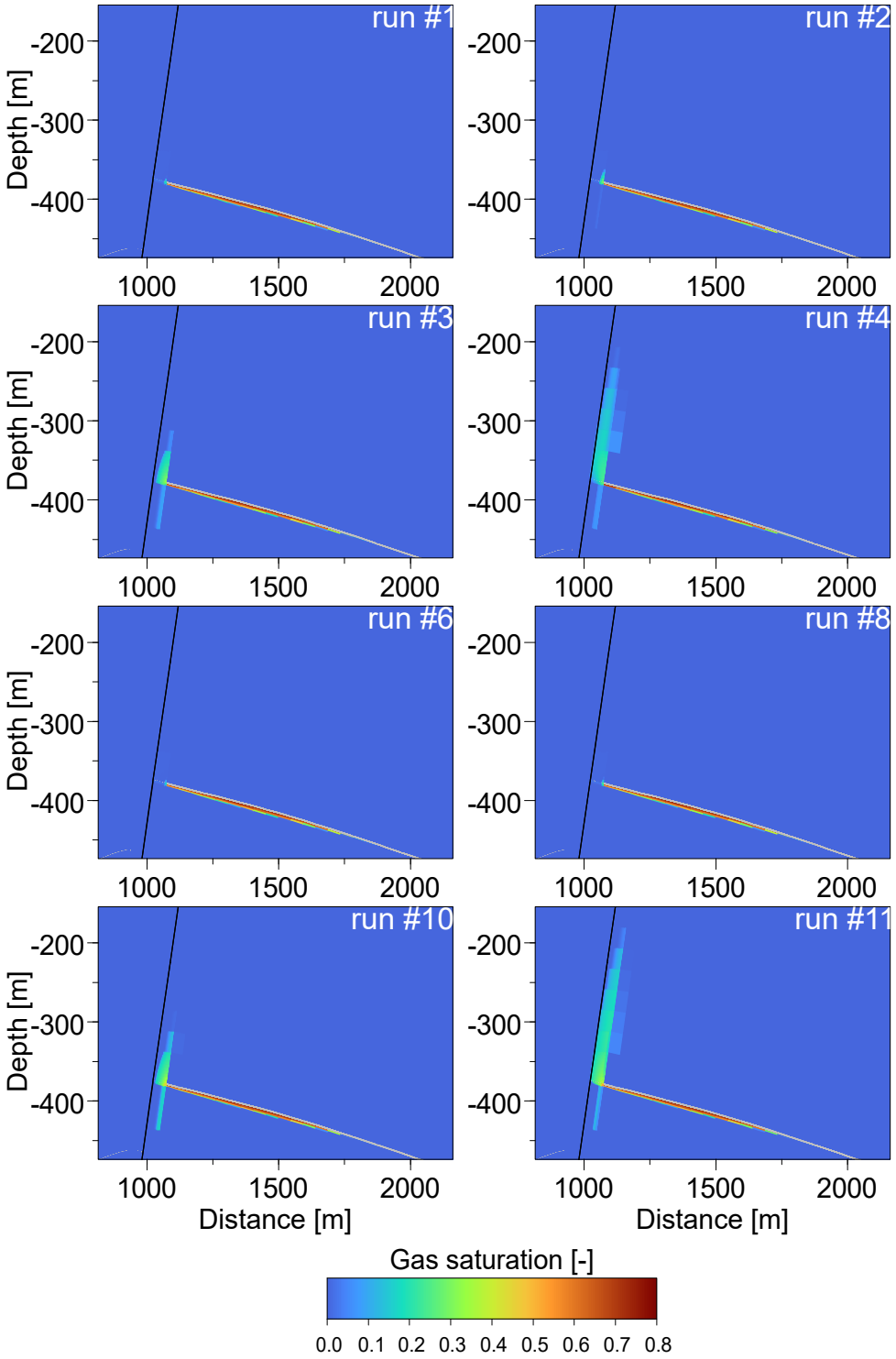

Figure 5.5: Gas phase saturation in the fault zone at day 1827, scaled-up by 3 units in z axis. The black tilted line represents the faults core. The gas flows from the storage formation to the damage zone and is directed upwards within the damage zone for runs #1-#4, #6, #8, #10 and #11.

and 3240 sm^3/d, in simulation runs #9, #10 and #11, respectively (Fig. 5.6c). For the simulation runs with higher fault zone permeabilities, a decrease in the leakage rates is observed, so that in simulation run #11 (10 mD, 0.13 bar) the average gas leakage rate is 2770 sm^3/d. For the low permeability case, the peak and average leakage rates only show a small

decrease over the injection periods. In the shut-in phase of the storage operation, leakage rates gradually decrease to around 47 sm^3/d, 497 sm^3/d and 1143 sm^3/d, for damage zone permeabilities of 0.1 mD, 1 mD and 10 mD, in combination with scaled entry pressures of 1.26 bar, 0.4 bar and 0.13 bar, correspondingly.

For all tested scenarios, an increase in the peak gas leakage rate is observed with the number of storage cycles (Fig. 5.6). This can be explained by changes in the phase mobility over time. After the first couple of storage cycles, gas intrudes into the fault zone (Fig. 5.5),

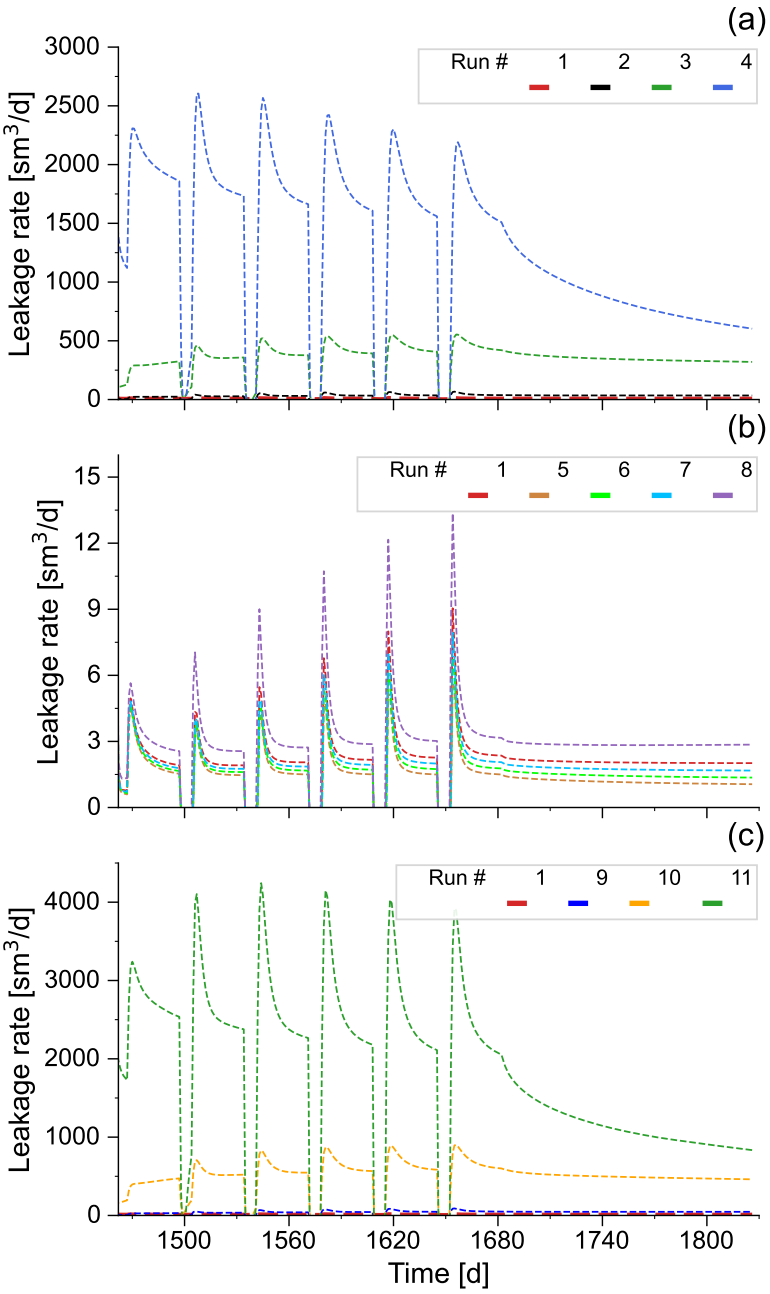

Figure 5.6: Gas leakage rates during six injection periods for: (a) scenario I – damage zone permeability cases; (b) scenario II – capillary entry pressure cases; (c) scenario III – normalised capillary entry pressure cases.

resulting in a reduced water saturation. Correspondingly, the relative permeability of gas in the affected area increases, while the relative permeability of water decreases. This increased gas mobility results in a further advance of the gas intrusion as the buoyancy of the gas drives it upwards. During the withdrawal cycles with no or only very little gas entering the fault zone, so this can result in decreasing gas saturations and thus a reduced mobility. After all storage cycles are completed, i.e. in the dormant phase of the storage, leakage rates decrease for all scenarios asymptotically, as the overpressures in the storage formation are redistributed and local pressure gradients decrease.

Comparing the average leakage rates during the injection phases of the storage operation shows a strong dependence of the observed leakage rates on the damage zone permeability and the capillary pressure (Fig. 5.7). Unsurprisingly, leakage rates decrease with increasing capillary entry pressure and decreasing damage zone permeability. Considerable gas leakage occurs when the damage zone permeability is greater than 1 mD. The capillary entry pressure acts as the main sealing mechanism with no significant gas leakage in any of the tested cases (Fig. 5.7b). However, the capillary entry pressure strongly depends on geometry of the pores within the rock formation, as does the permeability. Considering this, by scaling the capillary entry pressure according to the damage zone permeability shows a significant increase in the gas leakage rates for higher permeabilities and thus lower capillary entry pressures (Fig. 5.7c). Based on the leakage rate observed in the 2D model, the total

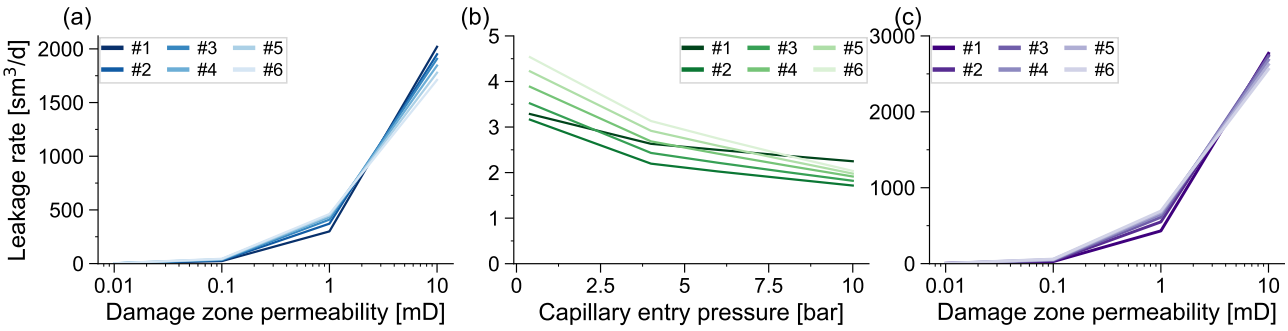

Figure 5.7: Comparison of the influence of fault zone parameters on the average leakage rate during six injection periods; Parameters: (a) damage zone permeability; (b) capillary entry pressure; (c) scaled capillary pressure and damage zone permeability.

leakage rate and the leakage volume can be calculated by considering the exposure of the gas-filled part of the storage formation to the fault zone. For the given site, the total exposure length is about 3900 m (Fig. 5.3). Thus, the total leakage rate is in the range from 1.3×10^2 sm^3/d to 2.2×10^5 sm^3/d during the injection periods of the storage operation and 0.2×10^2 sm^3/d to 1.5×10^5 sm^3/d during withdrawal. During a complete storage cycle the total gas leakage volume is in the range from 4.3×10^3 sm^3 to 7.5×10^6 sm^3, corresponding to 0.002% to 2.8% of the total GIP.

5.6 Conclusion to this chapter

In this study, the leakage of gas along a fault system during a subsurface gas storage operation at an existing geological structure was investigated and the dependence of the gas leakage rates on the fault damage zone permeability and capillary entry pressure was analysed. A 3D structural-geological model of the hypothetical storage site was constructed and used to simulate a storage operation to obtain realistic boundary conditions for the sensitivity analysis. The storage operation was designed to provide enough electricity for one week to offset a complete lack of renewable power generation in the state of Schleswig-Holstein, home to around 2.8 Million people. With the baseline characterisation, the gas storage can deliver 100% of the target power demand over a period of 7 days using five vertical wells. At the storage-fault interface this storage operation results in pressure changes between injection and withdrawal of around 7 bars. The leakage scenario simulations show that the fault zone intersecting the storage formation can act as either a conduit or a barrier for fluid flow, depending on petrophysical parameters, the fluid flow properties and the current storage operation. During gas injection the storage pressure increases, thus the peak leakage rates are observed during these phases with values as high as 3000 sm^3/d for damage zone permeabilities of 10 mD and capillary entry pressures of 0.13 bar. For lower damage zone permeabilities and higher capillary entry pressures, the gas leakage during injection is greatly reduced. However, the reduced or even reversed pressure differential between the storage formation and the fault zone during withdrawal periods can stop the leakage of gas altogether regardless of the parametrisation of the fault zone. Thus, for storage demand cases with long injection and short withdrawal periods gas leakage might be more prominent than in cases with equal length withdrawal and injection periods. The simulations show that the total leakage volume within one cycle is less than 1.0% of the GIP in the storage formation in most cases. For a highly permeable damage zones, the simulated leakage volume can reach up to 2.8% of the total GIP.

The presented study considers isotropic and homogeneous petrophysical properties in each individual (geological) unit. In reality, however, all formations and fault zones show spatial heterogeneity in their petrophysical parameters. A heterogeneous permeability distribution in the storage formation could result in a local increase or decrease of the formation pressure, compared to the homogenous case [Pfeiffer et al., 2017]. As shown in this and the previous studies such pressure changes affect the leakage rates occurring in the fault zone. Furthermore, heterogeneity in the fault zone can cause an appearance of impermeable lenses [Fredman et al., 2007, Torabi et al., 2013], resulting in a decrease in gas leakage rate and thus total leakage volume. It can also be expected that heterogeneity in the fault zone can prevent significant flow upwards within the damage zone, while the increase in pore

pressure and the resulting reduction in effective normal stress on the fault core can lead to its reactivation, potentially increasing the fault core permeability [Rinaldi et al., 2014b]. To consider these processes in fully coupled hydro-mechanical process simulations a detailed analysis and characterisation of the (site-specific) mechanical properties of a fault zone is required.

6 Summary and Concluding remarks

As renewable energy sources become a larger part of the energy mix, balancing the supply and demand of energy systems becomes more challenging on a daily and seasonal basis. The implementation of energy storage technologies is a key strategy for addressing the challenge of balancing energy systems with high shares of renewables. This study focuses on porous media subsurface storage options and investigates decisive aspects of hydrogen, synthetic methane and compressed air energy storage. The major findings and conclusions of this thesis are summarised as follows:

- The study identified potential storage sites within three main porous formations present and between about 400 m and 4000 m depth in various geological trap types focusing mainly on one of the parts of the North German Basin. The subsurface potential for individual sites may reach TWh scale capacity. The estimated subsurface potential for hydrogen, synthetic methane and compressed air energy storage is large enough to cover national-scale storage demand. The assessment approach is versatile and allows for a quantification of stored energy and exergy for individual sites, formations or specific depth ranges. Due to the large capacity identified, the uncertainty in achievable storage rates can be compensated by selection criterion. Only the most suitable sites through the detailed reservoir characterisation will allow to unit uncertainty.

- The determination of stored exergy at individual sites enables a systematic and consistent comparison of the retrievable energy using hydrogen, methane or CAES. Hydrogen and methane storage types exhibit higher stored exergy compared to CAES. This approach is the first of its kind to provide a consistent assessment and comparison of potential porous media storage sites for these three storage types. The assessment of exergetic efficiency reveals that anticipated mechanical exergy losses are significant for CAES but negligible for hydrogen or methane storage, primarily due to the higher proportion of chemical exergy. Therefore, prioritising sites with the highest achievable flow rates is crucial for CAES applications and the determination of the number and locations of storage sites depends on energy system planning strategies and the level of decarbonisation in the energy system.

- This work, based on site-specific scenario simulations that show PM-CAES systems have a power capacity of 115 MW and can store 12-50 GWh of energy, enabling continuous operation for up to two weeks. This significant capacity makes it a viable option for grid-scale power storage. The storage design is robust against variations

in future energy system scenarios and different power plant configurations, exhibiting efficiencies ranging from 0.54 to 0.67 and energy densities spanning 0.12 to 0.28 kWh/kg of stored air. The developed integrated assessment framework in this study enables the planning and optimisation of PM-CAES facilities at any potential storage sites worldwide, for large-scale storage applications in 100% renewable energy systems. The intricate nature of PM-CAES necessitates power plants designed to account for both energy system characteristics and geological storage settings within diverse energy market scenarios.

- Scenario simulations demonstrate the feasibility of PM-CAES with adiabatic plant topologies featuring two/three-stage compression and expansion sections in energy systems with significant shares of renewables. However, these systems exhibit relatively low energy densities of 0.14 kWh/kg and 0.12 kWh/kg, along with power mismatch during continuous power discharging. The high rate and large-scale heat storage required for adiabatic concept is still an unresolved technical issue. However, it is worth following this path, as adiabatic plants do not require additional heat source, thus, resulting in low CO_2 emissions.

- The developed coupled simulator, employing a semi-analytical solution, enables the assessment of the feasibility of PM-CAES under future energy system market conditions. The coupled simulator provides a consistent approximation, accurately predicting storage pressure, rates and capacity up to 98% compared to the full-scale geostorage model. Through two scenario studies, it is demonstrated that the designed PM-CAES plant achieves continuous energy discharge ranging from 3 GWh to 6.7 GWh, operating at a power rate of 50 MW and showcasing a storage efficiency of 0.53. The development method takes into account technological and geological constraints, facilitating a physically realistic modelling of processes within the storage reservoir. Therefore, this approach facilitates the optimisation of power plant configurations and storage operations for wide range of realistically fluctuating future energy system load profiles.

- The utilisation of the new coupled power plant - geostorage model, which incorporates a simplified reservoir model and semi-analytical solutions for the boreholes, significantly reduces computational time by approximately 20 times compared to numerical solutions. This approach enables the assessment of geological storage in detailed energy systems with hourly resolution within a few hours. It is important to note that the conceptual model relies on a simplified cylindrical representation where the volume of the gas phase in the storage formation remains constant, while the mass flow rates

are supported by varying storage pressure and, consequently, varying stored gas density. Future research should prioritise the optimisation of computational performance in the power plant simulator and the coupled interface code, as well as the integration of geostorage into national-scale energy system modelling frameworks.

- The investigation of gas leakage during subsurface storage operations along a fault zone reveals that the total leakage volume within one cycle is typically less than 1.0% of the GIP in the storage formation, with a potential maximum of 2.8% for highly permeable damage zones. Sensitivity analyses demonstrate the dependency of the leakage rate on the permeability of the fault damage zone and the capillary entry pressure. The methodology employed in this study involved the construction of a 3D geological model of the existing storage structure, which was utilised to simulate a methane storage operation and obtain realistic boundary conditions for sensitivity analysis. The results from the leakage scenario simulations indicate that the fault zone intersecting the storage formation can function as either a conduit or a barrier for fluid flow, depending on the petrophysical parameters of the fault zone, the fluid flow properties and the different storage operation phases. A better characterisation of flow rates along a fault could be achieved by an improved estimation of these hydraulic properties through geomechanical simulation.

- The sensitivity analysis reveals that a reduced or even reversed pressure differential between the storage formation and the fault zone during withdrawal periods has the potential to reduce or even temporarily stop the leakage, regardless of the parametrisation of the fault zone. While the study considered isotropic and homogeneous petrophysical properties in each individual geological unit, it is important to note that formations and fault zones exhibit spatial heterogeneity in their petrophysical parameters in reality. Accounting for spatial heterogeneity can significantly impact formation pressure and fault zone permeability. The presence of heterogeneity in the fault zone can result in impermeable lenses, which decrease the rate of gas leakage and prevent significant upward flow within the damage zone. However, it can also increase the permeability of the fault core, potentially leading to its reactivation, necessitating a detailed mechanical analysis of the fault zone. The findings regarding the quantification of induced hydraulic impacts have implications for the development of improved risk assessment and management strategies for subsurface storage operations, ensuring the implementation of safe and sustainable energy storage solutions.

The findings of this research support the development of innovative geological storage options for renewable energy systems, thereby supporting the transition to a sustainable fu-

ture. The practical solutions presented in this thesis offer insights for designing and operating storage facilities in porous media, enhancing understanding of the physical processes involved and the necessary technical flexibility. The developed workflows for modelling storage processes enable efficient assessments of the role of storage in renewable energy grids. The knowledge gained from this research holds both academic and practical significance, providing insights for policymakers and industry professionals, aiding in informed decision-making and driving advancements in geological storage technologies for a reliable and sustainable energy future.

References

F. Adamek, T. Aundrup, W. Glaunsinger, M. Kleimaier, H. Landinger, M. Leuthold, B. Lunz, A. Moser, C. Pape, and H. Pluntke. *Energiespeicher für die Energiewende: Speicherungsbedarf und Auswirkungen auf das Übertragungsnetz für Szenarien bis 2050*. 2012.

T. Ahmed. *Reservoir engineering handbook*. Gulf Professional Publishing, Houston, 5 edition, 2018. ISBN 9780128136492. doi: 10.1016/C2016-0-04718-6.

T. Ajayi, J. S. Gomes, and A. Bera. A review of CO_2 storage in geological formations emphasizing modeling, monitoring and capacity estimation approaches. *Petroleum Science*, 16 (5):1–36, 2019. doi: 10.1007/s12182-019-0340-8.

R. Al-Hussainy, H. Ramey, and P. Crawford. The Flow of Real Gases Through Porous Media. *Journal of Petroleum Technology*, 18(05):624–636, 1966. doi: 10.2118/1243-a-pa.

E. A. Al-Khdheeawi, S. Vialle, A. Barifcani, M. Sarmadivaleh, and S. Iglauer. Impact of reservoir wettability and heterogeneity on CO_2-plume migration and trapping capacity. *International Journal of Greenhouse Gas Control*, pages 142–158, 2017. doi: 10.1016/j.ijggc.2017.01.012.

J. Arfai, F. Jahne, R. Lutz, D. Franke, C. Gaedicke, and J. Kley. Late palaeozoic to Early Cenozoic geological evolution of the northwestern German North Sea (Entenschnabel): New results and insights. *Geologie en Mijnbouw/Netherlands Journal of Geosciences*, 93(4): 147–174, 2014. doi: 10.1017/njg.2014.22.

A. Aydin. Small faults formed as deformation bands in sandstone. *Pure and Applied Geophysics*, 116(4-5), 1978. doi: 10.1007/BF00876546.

S. Bachu. Review of CO_2 storage efficiency in deep saline aquifers. *International Journal of Greenhouse Gas Control*, 40:188–202, 2015. doi: 10.1016/j.ijggc.2015.01.007.

S. Bachu, D. Bonijoly, J. Bradshaw, R. Burruss, S. Holloway, N. P. Christensen, and O. M. Mathiassen. CO_2 storage capacity estimation: Methodology and gaps. *International Journal of Greenhouse Gas Control*, 1(4):430–443, 2007. doi: 10.1016/S1750-5836(07)00086-2.

R. Baldschuhn, F. Binot, S. Fleig, and F. Kockel. *Geotektonischer Atlas von Nordwest-Deutschland und dem-deutschen Nordsee-Sektor*. Schweizerbart'sche Verlagsbuchhandlung, Stuttgart, 2001.

S. Bartel and G. Janssen. Underground spatial planning - Perspectives and current research in Germany. *Tunnelling and Underground Space Technology*, 55:112–117, 2016. doi: 10.1016/j.tust.2015.11.023.

A. Bary, F. Crotogino, B. Prevedel, H. Berger, K. Brown, J. Frantz, W. Sawyer, M. Henzell, K. Mohmeyer, and N. Ren. Storing natural gas underground. *Oilfield Review*, 14(2):2–17, 2002.

S. Bauer, H. Class, M. Ebert, V. Feeser, H. Götze, A. Holzheid, O. Kolditz, S. Rosenbaum, W. Rabbel, D. Schäfer, and A. Dahmke. Modeling, parameterization and evaluation of monitoring methods for CO_2 storage in deep saline formations: the CO_2-MoPa project. *Environmental Earth Sciences*, 67(2):351–367, sep 2012. doi: 10.1007/s12665-012-1707-y.

S. Bauer, C. Beyer, F. Dethlefsen, P. Dietrich, R. Duttmann, M. Ebert, V. Feeser, U. Görke, R. Köber, O. Kolditz, W. Rabbel, T. Schanz, D. Schäfer, H. Würdemann, and A. Dahmke. Impacts of the use of the geological subsurface for energy storage: An investigation concept. *Environmental Earth Sciences*, 70(8):3935–3943, 2013. doi: 10.1007/s12665-013-2883-0.

S. Bauer, A. Dahmke, and O. Kolditz. Subsurface energy storage: geological storage of renewable energy—capacities, induced effects and implications. *Environmental Earth Sciences*, 76(20), oct 2017. doi: 10.1007/s12665-017-7007-9.

I. H. Bell, J. Wronski, S. Quoilin, and V. Lemort. Pure and pseudo-pure fluid thermophysical property evaluation and the open-source thermophysical property library coolprop. *Industrial and Engineering Chemistry Research*, 53(6):2498–2508, 2014. doi: 10.1021/ie4033999.

K. Benisch and S. Bauer. Short- and long-term regional pressure build-up during CO_2 injection and its applicability for site monitoring. *International Journal of Greenhouse Gas Control*, 19:220–233, nov 2013. doi: 10.1016/j.ijggc.2013.09.002.

D. B. Bennion, F. B. Thomas, T. Ma, and D. Imer. Detailed protocol for the screening and selection of gas storage reservoirs. In *SPE Proceedings - Gas Technology Symposium*, page 12, 2000. doi: 10.2118/59738-ms.

J. T. Birkholzer, C. M. Oldenburg, and Q. Zhou. CO_2 migration and pressure evolution in deep saline aquifers. *International Journal of Greenhouse Gas Control*, 40:203–220, 2015. doi: 10.1016/j.ijggc.2015.03.022.

H. Blanco and A. Faaij. A review at the role of storage in energy systems with a focus on Power to Gas and long-term storage. *Renewable and Sustainable Energy Reviews*, 81:1049–1086, 2018.

M. Bloemendal, M. Jaxa-Rozen, and T. Olsthoorn. Methods for planning of ATES systems. *Applied Energy*, 216:534–557, 2018. doi: 10.1016/j.apenergy.2018.02.068.

BMWi. Sixth "Energy Transition" Monitoring Report "The Energy of the Future". Technical report, Federal Ministry for Economic Affairs and Energy, Berlin, 2018.

H. Boigk. *Erdöl und Erdölgas in der Bundesrepublik Deutschland: Erdölprovinzen, Felder, Förderung, Vorräte, Lagerstättentechnik*. Enke, Stuttgart, 1981. ISBN 3432912714.

J. Bradshaw and T. Dance. Mapping geological storage prospectivity of CO_2 for the world's sedimentary basins and regional source to sink matching. pages 583–591. Elsevier, 2005. doi: 10.1016/B978-008044704-9/50059-8.

R. Brooks and A. Corey. Hydraulic properties of porous media. *Hydrology Papers, Colorado State University*, 3(March), 1964.

M. Budt, D. Wolf, R. Span, and J. Yan. A review on compressed air energy storage: Basic principles, past milestones and recent developments. *Applied Energy*, 170:250–268, 2016. doi: 10.1016/j.apenergy.2016.02.108.

H. V. Bui, R. A. Herzog, D. M. Jacewicz, G. R. Lange, E. R. Scarpace, and H. H. Thomas. Compressed-air energy storage: Pittsfield aquifer field test. Technical report, 1990.

D. G. Caglayan, N. Weber, H. U. Heinrichs, J. Linßen, M. Robinius, P. A. Kukla, and D. Stolten. Technical potential of salt caverns for hydrogen storage in Europe. *International Journal of Hydrogen Energy*, 45(11):6793–6805, 2020. doi: 10.1016/j.ijhydene.2019.12.161.

J. S. Caine, J. P. Evans, and C. B. Forster. Fault zone architecture and permeability structure. *Geology*, 24(11), 1996. doi: 10.1130/0091-7613(1996)024⟨1025:FZAAPS⟩2.3.CO;2.

J. F. Carneiro, C. R. Matos, and S. van Gessel. Opportunities for large-scale energy storage in geological formations in mainland Portugal. *Renewable and Sustainable Energy Reviews*, 99:201–211, 2019. doi: 10.1016/j.rser.2018.09.036.

F. Cebulla, J. Haas, J. Eichman, W. Nowak, and P. Mancarella. How much electrical energy storage do we need? A synthesis for the US, Europe, and Germany. *Journal of Cleaner Production*, 181:449–459, 2018. doi: 10.1016/j.jclepro.2018.01.144.

M. Chen, T. A. Buscheck, J. L. Wagoner, Y. Sun, J. A. White, L. Chiaramonte, and R. D. Aines. Analysis of fault leakage from Leroy underground natural gas storage facility, Wyoming, USA. *Hydrogeology Journal*, 21(7), 2013. doi: 10.1007/s10040-013-1020-1.

M. Child, C. Kemfert, D. Bogdanov, and C. Breyer. Flexible electricity generation, grid exchange and storage for the transition to a 100% renewable energy system in Europe. *Renewable Energy*, 139:80–101, 2019. doi: 10.1016/j.renene.2019.02.077.

L. Clarke, Y.-M. Wei, A. de la Vega Navarro, A. Garg, A. N. Hahmann, S. Khennas, I. M. L. Azevedo, A. Löschel, A. K. Singh, and L. Steg. Energy Systems. In *Climate Change 2022: Mitigation of Climate Change. Working Group III Contribution to the IPCC Sixth Assessment Report*. Cambridge University Press, 2022.

H. Class, A. Ebigbo, R. Helmig, H. K. Dahle, J. M. Nordbotten, M. A. Celia, P. Audigane, M. Darcis, J. Ennis-King, Y. Fan, et al. A benchmark study on problems related to co 2 storage in geologic formations: summary and discussion of the results. *Computational Geosciences*, 13:409–434, 2009. doi: 10.1007/s10596-009-9146-x.

F. Crotogino, S. Donadei, U. Bünger, and H. Landinger. Large-Scale Hydrogen Underground Storage for Securing Future Energy Supplies. In *18th World Hydrogen Energy Conference 2010 - WHEC 2010 Parallel Sessions Book 4: Storage Systems / Policy Perspectives, Initiatives and Co-operations*, volume 78, pages 37–45, 2010. doi: 10.1109/INTMAG.2015.7157557.

P. Denholm and M. Hand. Grid flexibility and storage required to achieve very high penetration of variable renewable electricity. *Energy Policy*, 39(3):1817–1830, 2011.

P. Denholm, E. Ela, B. Kirby, and M. Milligan. Role of energy storage with renewable electricity generation. Technical report, 2010.

F. Dethlefsen, M. Ebert, and A. Dahmke. A geological database for parameterization in numerical modeling of subsurface storage in northern Germany. *Environmental Earth Sciences*, 71(5):2227–2244, 2014. doi: 10.1007/s12665-013-2627-1.

S. Donadei and G. S. Schneider. Compressed Air Energy Storage in Underground Formations. In *Storing Energy: With Special Reference to Renewable Energy Sources*, pages 113–133. 2016. doi: 10.1016/B978-0-12-803440-8.00006-3.

H. Doornenbal and A. Stevenson. *Petroleum geological atlas of the Southern Permian Basin area*. European Association of Geoscientists Engineers, Houten, Netherlands, 2010. ISBN 9073781612. doi: 10.3997/2214-4609.20145798.

L. J. Durlofsky. Upscaling and gridding of fine scale geological models for flow simulation. In *8th International Forum on Reservoir Simulation*, Stresa, Italy, 2005.

D. J. Evans and J. M. West. An appraisal of underground gas storage technologies and incidents, for the development of risk assessment methodology. Technical report, Britisch Geological Survey, Nottingham, 2008.

D. R. Faulkner, A. C. Lewis, and E. H. Rutter. On the internal structure and mechanics of large strike-slip fault zones: Field observations of the Carboneras fault in southeastern Spain. *Tectonophysics*, 367(3-4), 2003. doi: 10.1016/S0040-1951(03)00134-3.

F. Feldmann, B. Hagemann, L. Ganzer, and M. Panfilov. Numerical simulation of hydrodynamic and gas mixing processes in underground hydrogen storages. *Environmental Earth Sciences*, 75:1–15, 2016.

Q. J. Fisher and R. J. Knipe. The permeability of faults within siliciclastic petroleum reservoirs of the North Sea and Norwegian Continental Shelf. *Marine and Petroleum Geology*, 18(10):1063–1081, dec 2001. doi: 10.1016/S0264-8172(01)00042-3.

P. Fleuchaus, B. Godschalk, I. Stober, and P. Blum. Worldwide application of aquifer thermal energy storage – A review. *Renewable and Sustainable Energy Reviews*, 94:861–876, 2018. doi: 10.1016/j.rser.2018.06.057.

E. Flodin, M. Gerdes, A. Aydin, and W. D. Wiggins. Petrophysical properties and sealing capacity of fault rock, Aztec Sandstone, Nevada. *AAPG Memoir*, 85:197–217, 2005.

S. Folga, E. Portante, S. Shamsuddin, A. Tompkins, L. Talaber, M. McLamore, J. Kavicky, G. Conzelmann, and T. Levin. US natural gas storage risk-based ranking methodology and results. Technical report, 2016.

H. Fossen, R. A. Schultz, Z. K. Shipton, and K. Mair. Deformation bands in sandstone: A review. *Journal of the Geological Society*, 164(4), 2007. doi: 10.1144/0016-76492006-036.

N. Fredman, J. Tveranger, S. Semshaug, A. Braathen, and E. Sverdrup. Sensitivity of fluid flow to fault core architecture and petrophysical properties of fault rocks in siliciclastic reservoirs: a synthetic fault model study. *Petroleum Geoscience*, 13(4):305–320, nov 2007. doi: 10.1144/1354-079306-721.

P. Gabrielli, A. Poluzzi, G. J. Kramer, C. Spiers, M. Mazzotti, and M. Gazzani. Seasonal energy storage for zero-emissions multi-energy systems via underground hydrogen storage. *Renewable and Sustainable Energy Reviews*, 121:109629, 2020. doi: 10.1016/j.rser.2019.109629.

F. Gasanzade, W. T. Pfeiffer, F. Witte, I. Tuschy, and S. Bauer. Subsurface renewable energy storage capacity for hydrogen, methane and compressed air – A performance assessment study from the North German Basin. *Renewable and Sustainable Energy Reviews*, 149:111422, oct 2021. doi: 10.1016/J.RSER.2021.111422.

F. Gasanzade, F. Witte, I. Tuschy, and S. Bauer. Integration of geological compressed air energy storage into future energy supply systems dominated by renewable power sources. *Energy Conversion and Management*, 277:116643, 2023. doi: 10.1016/j.enconman.2022.116643.

M. C. Geluk. *Stratigraphy and tectonics of Permo-Triassic basins in the Netherlands and surrounding areas*. PhD thesis, University of Utrecht,, 2005.

N. Gerhardt, F. Sandau, A. Scholz, H. Hahn, P. Schumacher, C. Sager, F. Bergk, C. Kämper, W. Knörr, and J. Kräck. Interaktion EE-Strom, Wärme und Verkehr. Technical report, Fraunhofer IWES, Kassel, 2015.

J. P. Gerling. Unterirdische Speicherpotenziale (Gas, H_2, Druckluft). In *Forum Netzintegration/DUH Speicher-Fachgespräch*, Berlin, 2010.

R. G. Gibson. Physical character and fluid-flow properties of sandstone-derived fault zones. *Geological Society Special Publication*, 127, 1998. doi: 10.1144/GSL.SP.1998.127.01.07.

I. Glendenning. Compressed air storage. *Physics in Technology*, 12(3):103–110, 1981. doi: 10.1088/0305-4624/12/3/i05.

J. Gluyas and C. A. Cade. Prediction of porosity in compacted sands. *AAPG Memoir*, (69): 19–27, 1997. doi: 10.1306/m69613c2.

G. Goffey, M. Attree, P. Curtis, F. Goodfellow, J. Lynch, D. MacKertich, T. Orife, and W. Tyrrell. New exploration discoveries in a mature basin: Offshore Denmark. *Petroleum Geology Conference Proceedings*, 8(1):287–306, 2018. doi: 10.1144/PGC8.1.

C. Guo, L. Pan, K. Zhang, C. M. Oldenburg, C. Li, and Y. Li. Comparison of compressed air energy storage process in aquifers and caverns based on the Huntorf CAES plant. *Applied Energy*, 181:342–356, 2016. doi: 10.1016/j.apenergy.2016.08.105.

L. Gurobi Optimization. Gurobi Optimizer Reference Manual, 2021, 2021.

R. Hable, H. Kaufhold, T. Liebsch-Dörschner, and C. Thomsen. Endbericht Speicher Kataster Deutschland für die Bundesländer Hamburg und Schleswig-Holstein. Technical report, Landesamt für Landwirtschaft, Umwelt und ländliche Räume des Landes Schleswig-Holstein, Flintbek, 2011.

N. Hartmann. Rolle und Bedeutung der Stromspeicher bei hohen Anteilen erneuerbarer Energien in Deutschland: Speichersimulation und Betriebsoptimierung. 2013.

N. Hartmann, O. Vöhringer, C. Kruck, and L. Eltrop. Simulation and analysis of different adiabatic compressed air energy storage plant configurations. *Applied Energy*, 93:541–548, 2012. doi: 10.1016/j.apenergy.2011.12.007.

N. Hassannayebi, S. Azizmohammadi, M. De Lucia, and H. Ott. Underground hydrogen storage: application of geochemical modelling in a case study in the Molasse Basin, Upper Austria. *Environmental Earth Sciences*, 78(5):177, 2019. doi: 10.1007/s12665-019-8184-5.

W. He, X. Luo, D. J. Evans, J. Busby, S. Garvey, D. Parkes, and J. Wang. Exergy storage of compressed air in cavern and cavern volume estimation of the large-scale compressed air

energy storage system. *Applied Energy*, 208:745–757, 2017. doi: 10.1016/j.apenergy.2017.09.074.

W. He, M. Dooner, M. King, D. Li, S. Guo, and J. Wang. Techno-economic analysis of bulk-scale compressed air energy storage in power system decarbonisation. *Applied Energy*, 282:116097, 2021. doi: 10.1016/j.apenergy.2020.116097.

F. Hese. *3D Modellierungen und Visualisierung von Untergrundstrukturen für die Nutzung des unterirdischen Raumes in Schleswig-Holstein*. PhD thesis, Christian-Albrechts Universität Kiel, 2012.

F. Hese, A. Schaller, and K. Lademann. Verbundvorhaben "StörTief" Die Rolle von tiefreichenden Störungszonen bei der geothermischen Energienutzung Teilprojekt (AP 1.2) Erarbeitung eines geothermischen 3D-Strukturmodells für den Glückstadtgraben in Schleswig-Holstein. Technical report, Landesamt für Landwirtschaft, Umwelt und ländliche Räume des Landes Schleswig-Holstein, Flintbek, 2017.

S. Hilpert, C. Kaldemeyer, U. Krien, S. Günther, C. Wingenbach, and G. Plessmann. The Open Energy Modelling Framework (oemof)-A new approach to facilitate open science in energy system modelling. *Energy strategy reviews*, 22:16–25, 2018. doi: 10.1016/j.esr.2018.07.001.

S. Hilpert, M. Söthe, and C. Wingenbach. ANGUSII Scenarios: Pathways to 100% Renewable German Energy System. mar 2020. doi: 10.5281/ZENODO.3714708.

S. Holloway, J. P. Heederik, L. G. H. van der Meer, I. Czernichowski-Lauriol, R. Harrison, E. Lindeberg, I. R. Summerfield, C. Rochelle, T. Schwarzkopf, and O. Kaarstad. The underground disposal of carbon dioxide. Final report JOULE II project no. CT92-0031. Technical report, British Geological Survey, Nottingham, 1996.

K. Holst, G. Huff, R. H. Schulte, and N. Critelli. Lessons from Iowa: development of a 270 megawatt compressed air energy storage project in midwest Independent System Operator: a study for the DOE Energy Storage Systems Program. Technical report, 2012.

J. D. Hunt, E. Byers, Y. Wada, S. Parkinson, D. E. H. J. Gernaat, S. Langan, D. P. van Vuuren, and K. Riahi. Global resource potential of seasonal pumped hydropower storage for energy and water storage. *Nature communications*, 11(1):947, 2020.

IEA. Net Zero by 2050: A Roadmap for the Global Energy Sector. Technical report, International Energy Agency, Paris, 2021.

S.-i. Inage. Prospects for Large-Scale Energy Storage in Decarbonised Power Grids. Technical Report 4, OECD/IEA, International Energy Agency (IEA), Paris, 2009.

IPCC. Mitigation of climate change. Technical report, (Cambridge Univ. Press, 2007, 2014.

F. Jähne-Klingberg, M. Wolf, S. Steuer, F. Bense, D. Kaufmann, and A. Weitkamp. Speicherpotenziale im zentralen deutschen Nordsee-Sektor. Technical report, Bundesanstalt für Geowissenschaften und Rohstoffe, Hannover, 2014.

R. Juanes, C. W. MacMinn, and M. L. Szulczewski. The Footprint of the CO_2 Plume during Carbon Dioxide Storage in Saline Aquifers: Storage Efficiency for Capillary Trapping at the Basin Scale. *Transport in Porous Media*, 82(1):19–30, 2010. doi: 10.1007/s11242-009-9420-3.

J. Juez-Larré, S. Van Gessel, R. Dalman, G. Remmelts, and R. Groenenberg. Assessment of underground energy storage potential to support the energy transition in the Netherlands. *First Break*, 37(7):57–66, 2019.

A. Kabuth, A. Dahmke, C. Beyer, L. Bilke, F. Dethlefsen, P. Dietrich, R. Duttmann, M. Ebert, V. Feeser, U. J. Görke, R. Köber, W. Rabbel, T. Schanz, D. Schäfer, H. Würdemann, and S. Bauer. Energy storage in the geological subsurface: dimensioning, risk analysis and spatial planning: the ANGUS+ project. *Environmental Earth Sciences*, 76(1):23, jan 2017. doi: 10.1007/s12665-016-6319-5.

D. L. Katz, D. Cornell, R. Kobayashi, F. H. Poettmann, J. A. Vary, J. R. Ellenbass, and C. F. Weinaug. *Handbook of Natural Gas Engineering*. New York, 1959.

H. Kaufhold, R. Hable, T. Liebsch-Dörschner, C. Thomsen, and R. Taugs. Verbreitung und Eigenschaften mesozoischer Sandsteine sowie überlagernder Barrieregesteine in Schleswig-Holstein und Hamburg–Basisinformationen zur energiewirtschaftlichen Nutzung des tieferenUntergrundes. *Schriftenreihe der Deutschen Gesellschaft für Geowissenschaften*, pages 38–60, 2011. doi: 10.1127/sdgg/74/2011/38.

T. Kempka, R. Herd, E. Huenges, R. Endler, C. Jahnke, S. Janetz, E. Jolie, M. Kühn, F. Magri, P. Meinert, I. Moeck, M. Möller, G. Munoz, O. Ritter, W. Schafrik, C. Schmidt-Hattenberger, E. Tillner, H.-J. Voigt, and G. Zimmermann. Joint Research Project Brine: Carbon Dioxide Storage in Eastern Brandenburg: Implications for Synergetic Geothermal Heat Recovery and Conceptualization of an Early Warning System Against Freshwater Salinization. 2015. doi: 10.1007/978-3-319-13930-2_9.

M. King, A. Jain, R. Bhakar, J. Mathur, and J. Wang. Overview of current compressed air energy storage projects and analysis of the potential underground storage capacity in India and the UK. *Renewable and Sustainable Energy Reviews*, 139:110705, 2021. doi: 10.1016/j.rser.2021.110705.

A. Kissinger, V. Noack, S. Knopf, D. Scheer, W. Konrad, and H. Class. Characterization of reservoir conditions for CO_2 storage using a dimensionless gravitational number applied to the North German Basin. *Sustainable Energy Technologies and Assessments*, 7:209–220, 2014. doi: 10.1016/j.seta.2014.06.003.

T. Klaus, C. Vollmer, K. Werner, H. Lehmann, and K. Müschen. Energieziel 2050 : 100% Strom aus erneuerbaren Quellen. Technical report, Umweltbundesamt, Dessau, 2010.

R. J. Knipe, Q. J. Fisher, G. Jones, M. R. Clennell, A. B. Farmer, A. Harrison, B. Kidd, E. Mcallister, J. R. Porter, and E. A. White. Fault seal analysis: successful methodologies, application and future directions. *Norwegian Petroleum Society Special Publications*, 7(C):15–38, jan 1997. doi: 10.1016/S0928-8937(97)80004-5.

S. Knopf and F. May. Comparing Methods for the Estimation of CO_2 Storage Capacity in Saline Aquifers in Germany: Regional Aquifer Based vs. Structural Trap Based Assessments. volume 114, pages 4710–4721, 2017. doi: 10.1016/j.egypro.2017.03.1605.

M. Kortekaas, U. Böker, C. Van Der Kooij, and B. Jaarsma. Lower Triassic reservoir development in the northern Dutch offshore. *Geological Society Special Publication*, 469(1): 149–168, 2018. doi: 10.1144/SP469.19.

L. Kristensen, M. L. Hjuler, P. Frykman, M. Olivarius, R. Weibel, L. H. Nielsen, and A. Mathiesen. Pre-drilling assessments of average porosity and permeability in the geothermal reservoirs of the Danish area. *Geothermal Energy*, 4(1):27, 2016. doi: 10.1186/s40517-016-0048-6.

N. Krzikalla, S. Achner, and S. Brühl. *Möglichkeiten zum Ausgleich fluktuierender Einspeisungen aus Erneuerbaren Energien: Studie im Auftrag des Bundesverbandes Erneuerbare Energie*. Ponte Press, 2013. ISBN 3920328647.

R. Kushnir, A. Ullmann, and A. Dayan. Compressed air flow within aquifer reservoirs of CAES plants. *Transport in porous media*, 81:219–240, 2010.

L. Lankof and R. Tarkowski. Assessment of the potential for underground hydrogen storage in bedded salt formation. *International Journal of Hydrogen Energy*, 45(38):19479–19492, 2020. doi: 10.1016/j.ijhydene.2020.05.024.

LBEG. Erdöl und Erdgas in der Bundesrepublik Deutschland. Technical report, Landesamt für Bergbau, Energie und Geologie, Hannover, 2018.

LBEG. Erdöl und Erdgas in der Bundesrepublik Deutschland. Technical report, Landesamt für Bergbau, Energie und Geologie, Hannover, 2021.

R. Lehné and F. Sirocko. Quantification of recent movement potentials in Schleswig-Holstein (Germany) by GIS-based calculation of correlation coefficients. *International Journal of Earth Sciences*, 94(5-6), 2005. doi: 10.1007/s00531-005-0043-9.

M. Leverett. Capillary behavior in porous solids. *Transactions of the AIME*, 142(01):152–169, 1941.

A. I. Levorsen. *Geology of Petroleum*. WH Freeman Company, San Francisco, 1956.

J. Lewandowska-Śmierzchalska, R. Tarkowski, and B. Uliasz-Misiak. Screening and ranking framework for underground hydrogen storage site selection in Poland. *International Journal of Hydrogen Energy*, 43(9):4401–4414, 2018.

D. Li, C. Beyer, and S. Bauer. A unified phase equilibrium model for hydrogen solubility and solution density. *International Journal of Hydrogen Energy*, 43(1), 2018. doi: 10.1016/j.ijhydene.2017.07.228.

M. Z. Lukawski, B. J. Anderson, C. Augustine, L. E. Capuano, K. F. Beckers, B. Livesay, and J. W. Tester. Cost analysis of oil, gas, and geothermal well drilling. *Journal of Petroleum Science and Engineering*, 2014. doi: 10.1016/j.petrol.2014.03.012.

H. Lund and G. Salgi. The role of compressed air energy storage (CAES) in future sustainable energy systems. *Energy conversion and management*, 50(5):1172–1179, 2009.

B. Lunz, P. Stöcker, S. Eckstein, A. Nebel, S. Samadi, B. Erlach, M. Fischedick, P. Elsner, and D. U. Sauer. Scenario-based comparative assessment of potential future electricity systems–A new methodological approach using Germany in 2050 as an example. *Applied energy*, 171:555–580, 2016.

X. Luo, J. Wang, M. Dooner, and J. Clarke. Overview of current development in electrical energy storage technologies and the application potential in power system operation. *Applied Energy*, 137:511–536, 2015. doi: 10.1016/j.apenergy.2014.09.081.

J. Ma, Q. Li, M. Kühn, and N. Nakaten. Power-to-gas based subsurface energy storage: A review. *Renewable and Sustainable Energy Reviews*, 97:478–496, 2018. doi: 10.1016/j.rser.2018.08.056.

T. Manzocchi, J. J. Walsh, P. Nell, and G. Yielding. Fault transmissibility multipliers for flow simulation models. *Petroleum Geoscience*, 5(1), 1999. doi: 10.1144/petgeo.5.1.53.

A. Mathiesen, L. Kristensen, T. Bidstrup, and L. H. Nielsen. Evaluation of the possible geothermal Gassum reservoir in the area around Rødding 1 well. Technical report, Kopenhagen., 2011.

C. R. Matos, J. F. Carneiro, and P. P. Silva. Overview of Large-Scale Underground Energy Storage Technologies for Integration of Renewable Energies and Criteria for Reservoir Identification. *Journal of Energy Storage*, 21, 2019. doi: 10.1016/j.est.2018.11.023.

MELUR. Erneuerbare Energien in Zahlen für Schleswig-Holstein. Versorgungsbeitrag in den Jahren 2006–2016, Ministerium für Energiewende, Landwirtschaft, Umwelt und ländliche Räume Schleswig-Holstein (MELUR). Technical report, Kiel, 2018.

A. B. Mitiku and S. Bauer. Optimal use of a dome-shaped anticline structure for CO_2 storage: A case study in the North German sedimentary basin. *Environmental Earth Sciences*, 70 (8):3661–3673, 2013. doi: 10.1007/s12665-013-2580-z.

K. Mongird, V. V. Viswanathan, P. J. Balducci, M. J. E. Alam, V. Fotedar, V. S. Koritarov, and B. Hadjerioua. Energy storage technology and cost characterization report. Technical report, 2019.

J. Mouli-Castillo, M. Wilkinson, D. Mignard, C. McDermott, R. S. Haszeldine, and Z. K. Shipton. Inter-seasonal compressed-air energy storage using saline aquifers. *Nature Energy*, 4(2):131–139, 2019. doi: 10.1038/s41560-018-0311-0.

M. Muskat. *The flow of homogeneous fluids through porous media*. J. W. Edwards, Publisher, Inc. Ann Arbor, 1946.

C. M. Oldenburg and L. Pan. Porous Media Compressed-Air Energy Storage (PM-CAES): Theory and Simulation of the Coupled Wellbore-Reservoir System. *Transport in Porous Media*, 97(2):201–221, 2013. doi: 10.1007/s11242-012-0118-6.

C. M. Oldenburg, A. J. A. Unger, R. P. Hepple, and P. D. Jordan. On leakage and seepage from geological carbon sequestration sites. Technical report, 2002.

M. Olivarius, R. Weibel, M. L. Hjuler, L. Kristensen, A. Mathiesen, L. H. Nielsen, and C. Kjøller. Diagenetic effects on porosity-permeability relationships in red beds of the Lower Triassic Bunter Sandstone Formation in the North German Basin. *Sedimentary Geology*, 321:139–153, 2015. doi: 10.1016/j.sedgeo.2015.03.003.

J. F. Osterle. The thermodynamics of compressed air exergy storage. *Journal of Energy Resources Technology, Transactions of the ASME*, 113(1):7–11, 1991. doi: 10.1115/1.2905781.

A. Palzer and H.-M. Henning. A comprehensive model for the German electricity and heat sector in a future energy system with a dominant contribution from renewable energy technologies–Part II: Results. *Renewable and Sustainable Energy Reviews*, 30:1019–1034, 2014.

J. Papay. ATermelestechnologiai Parameterek Valtozasa a Gazlelepk Muvelese Soran. *OGIL MUSZ, Tud, Kuzl., Budapest*, pages 267–273, 1968.

C. Pape, N. Gerhardt, P. Härtel, A. Scholz, R. Schwinn, T. Drees, A. Maaz, J. Sprey, C. Breuer, and A. Moser. Roadmap Speicher-Speicherbedarf für Erneuerbare Energien-Speicheralternativen-Speicheranreiz-Überwindung Rechtlicher Hemmnisse. Technical report, Fraunhofer IWES, Würzburg, 2014.

D. Parkes, D. J. Evans, P. Williamson, and J. D. O. Williams. Estimating available salt volume for potential CAES development: A case study using the Northwich Halite of the Cheshire Basin. *Journal of Energy Storage*, 18:50–61, 2018. doi: 10.1016/j.est.2018.04.019.

W. T. Pfeiffer and S. Bauer. Subsurface porous media hydrogen storage–scenario development and simulation. *Energy Procedia*, 76:565–572, 2015.

W. T. Pfeiffer and S. Bauer. Comparing simulations of hydrogen storage in a sandstone formation using heterogeneous and homogenous flow property models. *Petroleum Geoscience*, 25(3):325–336, 2019.

W. T. Pfeiffer, C. Beyer, and S. Bauer. Hydrogen storage in a heterogeneous sandstone formation: Dimensioning and induced hydraulic effects. *Petroleum Geoscience*, 23(3):315–326, aug 2017. doi: 10.1144/petgeo2016-050.

W. T. Pfeiffer, F. Witte, I. Tuschy, and S. Bauer. Coupled power plant and geostorage simulations of porous media compressed air energy storage (PM-CAES). *Energy Conversion and Management*, 249:114849, dec 2021. doi: 10.1016/J.ENCONMAN.2021.114849.

K. Reinhold, P. Krull, F. Kockel, and J. Rätz. *Salzstrukturen Norddeutschlands: Geologische Karte, 1: 500 000*. Herausgeber, Bundesanstalt für Geowissenschaften und Rohstoffe, 2008.

K. Reinhold, C. Müller, and C. Riesenberg. Informationssystem Speichergesteine für den Standort Deutschland-Synthese. Technical report, Berlin, Hannover, 2011.

N. E. Research and IEA. Nordic energy technology perspectives 2016. cities, flexibility and pathways to carbon-neutrality. Technical report, Oslo, Paris, 2016.

A. P. Rinaldi, P. Jeanne, J. Rutqvist, F. Cappa, and Y. Guglielmi. Effects of fault-zone architecture on earthquake magnitude and gas leakage related to CO_2 injection in a multilayered sedimentary system. *Greenhouse Gases: Science and Technology*, 4(1), 2014a. doi: 10.1002/ghg.1403.

A. P. Rinaldi, J. Rutqvist, and F. Cappa. Geomechanical effects on CO_2 leakage through fault zones during large-scale underground injection. *International Journal of Greenhouse Gas Control*, 20, 2014b. doi: 10.1016/j.ijggc.2013.11.001.

P. S. Ringrose and T. A. Meckel. Maturing global co_2 storage resources on offshore continental margins to achieve 2ds emissions reductions. *Scientific Reports*, 9(1):1–10, 2019. doi: 10.1038/s41598-019-54363-z.

T. Röckel and C. Lempp. Der spannungszustand im Norddeutschen Becken. *Erdoel Erdgas Kohle*, 119(2):73–80, 2003. ISSN 01793187.

A. Sainz-Garcia, E. Abarca, V. Rubi, and F. Grandia. Assessment of feasible strategies for seasonal underground hydrogen storage in a saline aquifer. *International Journal of Hydrogen Energy*, 42(26):16657–16666, 2017. doi: 10.1016/j.ijhydene.2017.05.076.

K. Schaber, F. Steinke, and T. Hamacher. Managing temporary oversupply from renewables efficiently: Electricity storage versus energy sector coupling in germany. In *International energy workshop, Paris*, 2013.

F. Schäfer, L. Walter, H. Class, and C. Müller. Regionale Druckentwicklung bei der Injektion von CO_2 in salinare Aquifere. *BGR Abschlussbericht*, 2010.

S. Schiebahn, T. Grube, M. Robinius, V. Tietze, B. Kumar, and D. Stolten. Power to gas: Technological overview, systems analysis and economic assessment for a case study in Germany. *International Journal of Hydrogen Energy*, 40(12), 2015. doi: 10.1016/j.ijhydene.2015.01.123.

W.-P. Schill. Residual load, renewable surplus generation and storage requirements in Germany. *Energy Policy*, 73:65–79, 2014.

Schlumberger Ltd. Eclipse Reservoir Simulation Software v2017.2, Technical Description Manual. Technical report, Houston, United States, 2017.

Schlumberger Ltd. Petrel EP Software platform v2018.1, 2018.

Z. K. Shipton and P. A. Cowie. Damage zone and slip-surface evolution over μm to km scales in high-porosity Navajo sandstone, Utah. *Journal of Structural Geology*, 23(12):1825–1844, dec 2001. doi: 10.1016/S0191-8141(01)00035-9.

S. G. Soldatkin. Complex of researches for creation of hydrodynamic model of operation Kaluga UGS. *Georesursy*, 36(4), 2010.

A. A. Solomon, D. M. Kammen, and D. Callaway. The role of large-scale energy storage design and dispatch in the power grid: a study of very high grid penetration of variable renewable resources. *Applied Energy*, 134:75–89, 2014.

D. Sopher, C. Juhlin, T. Levendal, M. Erlström, K. Nilsson, and J. P. Da Silva Soares. Evaluation of the subsurface compressed air energy storage (CAES) potential on Gotland, Sweden. *Environmental Earth Sciences*, 78(6):17, 2019. doi: 10.1007/s12665-019-8196-1.

B. Sørensen. Energy and Resources: A plan is outlined according to which solar and wind energy would supply Denmark's needs by the year 2050. *Science*, 189(4199):255–260, 1975.

SRU. *Wege zur 100% erneuerbaren Stromversorgung: Sondergutachten*. Erich Schmidt, 2011. ISBN 3503136061.

M. Sterner and I. Stadler. *Energiespeicher - Bedarf, Technologien, Integration*. Springer Vieweg, Berlin, Heidelberg, 2014. ISBN 978-3-642-37379-4. doi: 10.1007/978-3-642-37380-0.

S. Succar and R. H. Williams. Compressed air energy storage: theory, resources, and applications for wind power. Technical report, Princeton University, Princeton, 2008.

J. Szargut. Chemical exergies of the elements. *Applied Energy*, 32(4):269–286, 1989. doi: 10.1016/0306-2619(89)90016-0.

R. Tarkowski. Perspectives of using the geological subsurface for hydrogen storage in Poland. *International Journal of Hydrogen Energy*, 42(1):347–355, 2017.

R. Tarkowski, B. Uliasz-Misiak, and P. Tarkowski. Storage of hydrogen, natural gas, and carbon dioxide–Geological and legal conditions. *International Journal of Hydrogen Energy*, 46(38):20010–20022, 2021. doi: 10.1016/j.ijhydene.2021.03.131.

C. Thomsen. Porositäts – Tiefen Beziehung für Reservoir sandsteine. Technical report, Landesamt für Landwirtschaft, Umwelt und ländliche Räume des Landes Schleswig-Holstein, Flintbek, 2013.

TNO and EBN. Ondergrondse opslag in Nederland-Technische verkenning. Technical report, TNO-Report: 2018 R11372, Utrecht, 2018.

A. Torabi, H. Fossen, and A. Braathen. Insight into petrophysical properties of deformed sandstone reservoirs. *AAPG Bulletin*, 97(4):619–637, apr 2013. doi: 10.1306/10031212040.

I. Tuschy. Compressed air energy storage power plants as an option for the grid integration of renewable energy sources. A comparison of the concepts; Druckluftspeicherkraftwerke als Option zur Netzintegration erneuerbarer Energiequellen. Ein Vergleich der Konzepte. page 12, Germany, 2008. Fachhochschule Flensburg (Germany). Inst. fuer Energiesystemtechnik.

I. Tuschy, R. Althaus, R. Gerdes, and P. Keller-Sornig. Compressed air energy storage with high efficiency and power output. *VDI-Verlag*, 1734(In Energiespeicher):57–66, 2002.

UBA. Erneuerbare Energien in Deutschland 2019. Daten zur Entwicklung im Jahr 2019. Technical report, Geschäftsstelle der Arbeitsgruppe Erneuerbare Energien-Statistik (AGEE-Stat) am Umweltbundesamt, Dessau, 2020.

T. Vangkilde-Pedersen, K. Kirk, N. Smith, N. Maurand, A. Wojcicki, F. Neele, C. Hendriks, Y. Le Nindre, and K. Lyng Anthonsen. Assessing European Capacity for Geological Storage of Carbon Dioxide – the EU GeoCapacity project no. SES6-518318. Technical report, Copenhagen, 2009.

B. Wang and S. Bauer. Compressed air energy storage in porous formations: A feasibility and deliverability study. *Petroleum Geoscience*, 23(3):306–314, 2017. doi: 10.1144/petgeo2016-049.

B. Wang and S. Bauer. Induced geochemical reactions by compressed air energy storage in a porous formation in the North German Basin. *Applied Geochemistry*, 102:171–185, mar 2019. doi: 10.1016/j.apgeochem.2019.02.003.

F. E. Watson, S. A. Mathias, S. E. Daniels, R. R. Jones, R. J. Davies, B. J. Hedley, and J. van Hunen. Dynamic modelling of a UK North Sea saline formation for CO_2 sequestration. *Petroleum Geoscience*, 20(2):169–185, 2014. doi: 10.1144/petgeo2012-072.

S. Weitemeyer, D. Kleinhans, T. Vogt, and C. Agert. Integration of Renewable Energy Sources in future power systems: The role of storage. *Renewable Energy*, 75:14–20, 2015. doi: 10.1016/j.renene.2014.09.028.

F. Witte and I. Tuschy. TESPy: Thermal Engineering Systems in Python. *Journal of Open Source Software*, 5(49):2178, 2020. doi: 10.21105/joss.02178.

M. Wolf, S. Steuer, F. Jähne, D. Kaufmann, and A. Weitkamp. 3D-Lithofaziesmodell des Buntsandstein in der zentralen deutschen Nordsee. Technical report, Bundesanstalt für Geowissenschaften und Rohstoffe, Hannover, 2014.

B. Zakeri and S. Syri. Electrical energy storage systems: A comparative life cycle cost analysis. *Renewable and sustainable energy reviews*, 42:569–596, 2015.

Publications associated with this research

Chapter 2

Firdovsi Gasanzade, Wolf Tilmann Pfeiffer, Francesco Witte, Ilja Tuschy and Sebastian Bauer (2021) Subsurface renewable energy storage capacity for hydrogen, methane and compressed air–A performance assessment study from the North German Basin. Renewable and Sustainable Energy Reviews 149. doi:10.1016/j.rser.2021.111422

Abstract

The transition to renewable energy sources to mitigate climate change will require large-scale energy storage to dampen the fluctuating availability of renewable sources and to ensure a stable energy supply. Energy storage in the geological subsurface can provide capacity and support the cycle times required. This study investigates hydrogen storage, methane storage and compressed air energy storage in subsurface porous formations and quantifies potential storage capacities as well as storage rates on a site-specific basis. For part of the North German Basin, used as the study area, potential storage sites are identified, employing a newly developed structural geological model. Energy storage capacities estimated from a volume-based approach are 6510 TWh and 24544 TWh for hydrogen and methane, respectively. For a consistent comparison of storage capacities including compressed air energy storage, the stored exergy is calculated as 6735 TWh, 25795 TWh and 358 TWh for hydrogen, methane and compressed air energy storage, respectively. Evaluation of storage deliverability indicates that high deliverability rates are found mainly in two of the three storage formations considered. Even accounting for the uncertainty in geological parameters, the storage potential for the three considered storage technologies is significantly larger than the predicted demand, and suitable storage rates are achievable in all storage formations.

Chapter 3

Firdovsi Gasanzade, Francesco Witte, Ilja Tuschy and Sebastian Bauer (2023) Integration of geological compressed air energy storage into future energy supply systems dominated by renewable power sources. Energy Conversion and Management 277. doi:10.1016/j.enconman.2022.116643

Abstract Compressed air energy storage in geological porous formations, also known as porous medium compressed air energy storage (PM-CAES), presents one option for balanc-

ing the fluctuations in energy supply systems dominated by renewable energy sources. The strong coupling between the subsurface storage facility and the surface power plant via the pressure of the compressed air, which directly determines the amount of energy stored and the power rates achievable, requires the consideration of the fluctuating supply and demand of electric power, the specific technical design of the compressed air energy storage plant and the subsurface storage processes to determine achievable power rates, storage capacities and overall performance. In this paper, we present subsurface storage designs using a set of future energy system scenarios with different fractions of renewable energy supply and technical options for the power plant. Our findings indicate that the PM-CAES systems can supply 115 MW of electric power and between 12.1 GWh and 49.9 GWh of electric energy for up to 429 h, thus offering grid-scale power storage capacity. The storage design is robust against variations in future energy system scenarios and different power plant configurations, with efficiencies between 0.54 and 0.67 and energy densities between 0.12 and 0.28 kWh per kilogram of stored air. The storage design can be improved further by using horizontal instead of vertical wells, which also reduces induced pressure increases in the storage formation. This study for the first time provides a complete framework for assessing achievable storage rates and capacities for PM-CAES based on detailed forecasts of future energy systems, the geological and geotechnical setting as well as engineering aspects of the compressed air energy power plant.

Chapter 4

Firdovsi Gasanzade, Wolf Tilmann Pfeiffer and Sebastian Bauer (2022) Proxy Model Development and Application for Coupled Power Plant and Geostorage Simulations of Compressed Air Energy Storage. Energy Proceedings 22. doi:10.46855/energy-proceedings-10154

Abstract

Porous media compressed air energy storage (PM-CAES) is a viable option to compensate expected fluctuations in energy supply in future energy systems with a 100% share of renewables. However, the design and evaluation of operational conditions for a PM-CAES require an efficient coupled power plant – geostorage model. In this study, therefore, a proxy model for the geostorage is developed and evaluated with respect to two scenarios representing realistic energy system load profiles. Results show, that the proxy model represents a consistent approximation, yielding storage pressure, rates and capacity within 98% of the full-scale reservoir model, while reducing runtimes to about 6%.

Chapter 5

Firdovsi Gasanzade, Sebastian Bauer and Wolf Tilmann Pfeiffer (2019) Sensitivity analysis of gas leakage through a fault zone during subsurface gas storage in porous formations. Advances in Geosciences 49. doi:10.5194/adgeo- 49-155-2019

Abstract

Subsurface gas storage in porous media is a viable option to mitigate shortages in energy supply in systems largely based on renewable sources. Fault systems adjacent to or intersecting with gas storage could potentially result in a leakage of stored gas. Variations in formation pressure during a storage operation can affect the gas leakage rates, requiring a site and scenario specific assessment. In this study, a geological model of an existing structure in the North German Basin (NGB) is developed, parameterised and a methane gas storage operation is simulated. Based on the observed storage pressure, a sensitivity study aimed at determining gas leakage rates for different parametrisations of the fault damage zone is performed using a simplified 2D model. The leakage scenario simulations show a strong parameter dependence with the fault acting as either a barrier or a conduit for gas flow. Furthermore, the storage operation greatly affects the gas leakage rates for a given parametrisation with significant leakage only during the injection periods and thus during increased overpressures in the storage formation. During injection, the peak leakage rates can be as high as 2308 sm^3/d for damage zone permeabilities of 10 mD and a capillary entry pressure of 4 bars. Increasing capillary entry pressure results in a sealing effect. If the capillary entry pressure is scaled according to the damage zone permeability, peak leakage rates can be higher, i.e. 3240 sm^3d for 10 mD and 0.13 bar. During withdrawal periods, the pressure gradient between a storage formation and a fault zone is reduced or even reversed, resulting in greatly reduced leakage rates or even a temporary stop of the leakage. Total leakage volume from storage formation was assessed based on the 2D study by considering the exposure of the gas-filled part of the storage formation to the fault zone and subsequently compared with gas in place volume.

Nomenclature

Symbols

A	area of storage closure, m^2
B_g	gas formation volume factor, rm^3/sm^3
D	well diameter, m
ex_{ph}	physical exergy, kJ
H	specific enthalpy, kJ/kg
h	net formation thickness, m
k_s	pipe roughness, m
k	formation permeability, m^2 ($1.013 \cdot 10^{15}$ mD)
L	vertical well length, m
L_c	total completion length, m
L_h	horizontal section length, m
m	mass of gas in place, kg
M_{gas}	mass of gas within the storage formation, kg
p	formation pressure, Pa
p_0	ambient pressure, Pa
$p_{bhp,w}$	well bottom hole pressure, Pa
p_c	capillary entry pressure, bar
p_{crit}	critical pressure, Pa
p_{res}	reservoir pressure at the outer boundary, Pa (10^{-5} bar)
p_s	standard pressure, Pa
Q	flow rate, m^3/s
r_e	drainage radius, m
r_{res}	reservoir radius of the outer gas phase, m
r_w	wellbore radius, m
S	specific entropy, kJ/(kg · K)
s	mechanical skin factor, dimensionless
S_g	maximum gas saturation, dimensionless
$S_{w,r}$	residual water saturation, dimensionless
T	formation temperature, K
T_0	ambient temperature, K
T_{crit}	critical temperature, K
T_s	standard temperature, K

V_{gas}	initial gas in place volume, m^3
Z_f	gas compressibility Z-factor, dimensionless
$\eta_{I(s,cmp)}$	compressor isentropic efficiency, dimensionless
$\eta_{I(s,exp)}$	turbine isentropic efficiency, dimensionless
μ_{res}	dynamic viscosity, $Pa \cdot s$
ρ_{res}	gas density at reservoir conditions, kg/m^3
ρ_{surf}	gas density at surface conditions, kg/m^3
ϕ	formation porosity, dimensionless
$\psi(p)$	real gas pseudo-pressure function, $Pa^2/(Pa \cdot s)$

Acronyms

BHP	Bottom Hole Pressure
CAES	Compressed Air Energy Storage
CCGT	Combined Cycle Power Plant
CCS	Carbon Capture and Sequestration
GIP	Gas in Place Volume
GIS	Geographic Information System
GTA	Geotectonic Atlas of Northwest Germany and the German North Sea Sector
NGB	North German Basin
SH	Schleswig-Holstein
TESPy	Thermal Engineering Systems in Python
OCGT	Open Cycle Gas Turbine
ZNS	Central North Sea Sector
2-AA-CAES	Adiabatic plant with two-stage compression and expansion stages
3-AA-CAES	Adiabatic plant with three-stage compression and expansion stages
D-CAES	Diabatic plant with three-stage compression and two-stage expansion stages